

Numerical modeling of igniting non-premixed
combustion systems
using FGM

Aromal Vasavan

Numerical modeling of igniting non-premixed combustion systems using
FGM
by Aromal Vasavan.
Technische Universiteit Eindhoven, 2021

A catalogue record is available from the Eindhoven University of Technology
Library
ISBN: 978-90-386-5392-1
Printed by Gildeprint
Cover design by Aromal Vasavan

Copyright © 2021 by Aromal Vasavan. All Rights Reserved.
No part of this material may be reproduced, distributed, or transmitted in any
form or by any means, without the prior written permission of the author.

This research is funded by the Dutch Research Council (NWO), Domain Ap-
plied and Engineering Sciences (TTW) (under project number 10766: Clean
Combustion of Future Fuels).

Numerical modeling of igniting non-premixed combustion systems using FGM

PROEFSCHRIFT

ter verkrijging van de graad van doctor aan de Technische
Universiteit Eindhoven, op gezag van de rector magnificus prof.dr.ir.
F.P.T. Baaijens, voor een commissie aangewezen door het College
voor Promoties, in het openbaar te verdedigen op
dinsdag 30 november 2021 om 11:00 uur

door

Aromal Vasavan

geboren te Thamarakkulam, India

Dit proefschrift is goedgekeurd door de promotoren en de samenstelling van de promotiecommissie is als volgt:

voorzitter: prof.dr.ir. D.M.J. Smeulders
1e promotor: prof.dr.ir. J.A. van Oijen
2e promotor: prof.dr. L.P.H. de Goey
Leden: prof.dr. D.J.E.M. Roekaerts (Technische Universiteit Delft)
prof.dr.ir. B. Merci (Universiteit Gent)
prof.dr. A. Parente (Université Libre de Bruxelles)
prof.dr.ir. N.G. Deen

Het onderzoek of ontwerp dat in dit proefschrift wordt beschreven is uitgevoerd in overeenstemming met de TU/e Gedragscode Wetenschapsbeoefening.

Numerical modeling of igniting non-premixed combustion systems using FGM

This thesis presents an extensive numerical modeling study on igniting non-premixed systems of combustion, with emphasis on biogas combustion. The scope of the research covers three main steps, starting with 1D modeling studies of igniting non-premixed flames using detailed chemistry (GRI), a generic method to formulate a reaction progress variable for the application in FGM, and finally LES modeling of turbulent Jet in Hot Coflow (JHC) systems using FGM.

In the first step the ignition delay of biogas in mixing layers is investigated using a 1D combustion model, with its application in Moderate or Intense Low oxygen Dilution (MILD) combustion being the focus. The study reveals the key aspects of the ignition of biogas in a nonpremixed, igniting mixing layer with a hot oxidizer of low oxygen content. Biogas is considered here as a mixture of CH₄ with variable amounts CO₂. The ignition delay predictions from one-dimensional mixing layers show no significant influence of CO₂ levels in biogas. The study also reveals the role of oxidizer composition and temperature on the ignition characteristics of a MILD biogas flame.

In order to extend the study to igniting turbulent flames that covers the MILD regime, LES with FGM serves an effective tool, given that there exists a reaction progress variable that can reproduce the ignition behavior of the fuels accurately. Therefore, a new method to formulate reaction progress variables for the application of FGM in combustion systems was developed. The method involves a multiobjective optimisation to find a reaction progress variable that accurately reproduces complex reactive phenomenon of interest. Through its application in a number of igniting counterflow flames, the effectiveness of the current method is verified.

Further, an Igniting Mixing Layer (IML) based FGM approach is implemented in LES modeling of JHC flames. The modeling criteria required for accurate representation of various flame characteristics are evaluated. Flames in two well-known JHC experimental burners are simulated, namely, the Cabra vitiated coflow burner using methane, and the Delft Jet in Hot Coflow burner using Dutch Natural Gas and

biogas like mixtures. With a refined set of modeling criteria, the variation in flame lift off height with respect to jet Reynolds number is investigated for DJHC flames. Finally, the impact of CO₂ levels on biogas flame behavior is analyzed using LES simulations of DJHC burner. This part of the study concludes that IML based FGM together with well-chosen submodels for sub-grid scale variance of mixture fraction is able to predict auto-igniting flames in a broad range of conditions.

The thesis thus draws out a computational methodology for modelling the ignition behavior of biogas and other methane based fuels in nonpremixed systems, to be extended to avenues such as recirculation to aid in the development of MILD burners for biogas-like fuels of future.

Contents

Abstract	v
1 Introduction	1
1.1 Energy and combustion	1
1.2 Biogas	3
1.3 Flameless or MILD combustion	3
1.4 Numerical studies on JHC flames	7
2 Auto Ignition of Biogas in MILD Non-premixed Combustion Systems	11
2.1 Introduction	11
2.2 Computational method	13
2.3 Results and discussion	16
2.3.1 Structure of IML and comparison with ICF	16
2.4 Conclusion	31
2.A Appendix	34
3 FGM modeling of autoigniting non-premixed systems	37
3.1 Introduction	37
3.2 Method	39
3.2.1 New optimization approach	42
3.3 Results and Discussion	46
3.3.1 Application in Cabra vitiated coflow flame	46
3.3.2 Application of IML based FGM in ICF	53
3.3.3 Application in DJHC flame	53
3.3.4 ECN Spray-A using n-dodecane.	55
3.4 Conclusion	57
3.A Appendix	59
4 Modeling Jet in Hot Coflow Flames	61
4.1 Introduction	61
4.2 Model description	63
4.2.1 FGM model	65
4.2.2 Computational set-up	68
4.3 Results and Discussion	71

4.3.1	Jet in a uniform hot coflow (Cabra)	71
4.3.2	Jet in non-uniform coflow (DJHC-I)	78
4.3.3	Biogas JHC simulations (DJHC-X)	84
4.3.4	Comparison to measurements	90
4.3.5	Influence of Reynolds number in DJHC-I	91
4.4	Conclusion	94
4.A	Appendix	98
4.A.1	Inlet turbulence generation	98
4.A.2	Simplification of coflow boundary	99
4.A.3	Conservative scalar transport	99
5	Conclusions & Outlook	101
	Acknowledgement	115
	Curriculum Vitae	115
	List of Publications	117

1.1 Energy and combustion

Energy is a basic input for many economic production and consumption activities, and the consumption of energy is strongly dependent on the economic growth of a nation [1]. The shift from an economy that relied on land resources to one based on the combustion of fossil fuels marked the onset of industrial revolution in the British economy [2–4] and in the rest of the world. The role of combustion technology in human life has been highlighted to this day, as a means of transforming primary energy into heating, propulsion, mechanical and electrical power. Further, the global energy consumption is projected to rise together with economic growth and it is also known that the rate of consumption flattens as the nations achieve higher Gross National Product (GNP). Most of the increase in energy consumption is predicted to come from non-OECD countries where a strong economic growth, increased access to the energy market and a rising population are expected. Energy consumption in non-OECD countries is expected to grow by 70% between 2018 and 2050 in contrast to 15% growth in OECD countries as shown in Fig. 1.1 [5]. In a time where the countermeasures against climate change are receiving more and more support, it has to be kept in mind that these expectations may turn out differently.

Figure 1.2 shows the foreseen trend till 2050 in energy consumption by source [6]. It is predicted that renewable energy will be the leading source of primary energy consumption by 2050, and in the absence of new measures to limit their consumption, fossil fuels will continue to be consumed over this period. Among fossil fuels, the consumption of natural gas is the world's fastest growing one. The renewable energy consumption is set to increase by 3% per year between 2018 and 2050, which is driven mainly by electricity demand growth, economic and political drivers.

However, the predicted expansion in energy consumption also adds a tremendous burden on the environment via carbon dioxide emissions [7], which worsens global warming and associated climate phenomena. According to the Intergovernmental Panel on Climate Change (IPCC) special report titled “Global Warming of 1.5°C” [8], the adverse consequences of global warming on ecosystems and communities can only be avoided if the world limits the global temperature rise to 1.5 °C. To accomplish this goal, the global anthropogenic CO₂ emissions is required to be reduced by about 45% by 2030 from the emission levels in 2010, to net zero CO₂ emission in 2050. To this end, long-term international climate action [8] is warranted. The “European Green Deal” [9], announced by the European Commission Vice-President, Frans Timmermans in 2019, aims for a greenhouse gas emissions

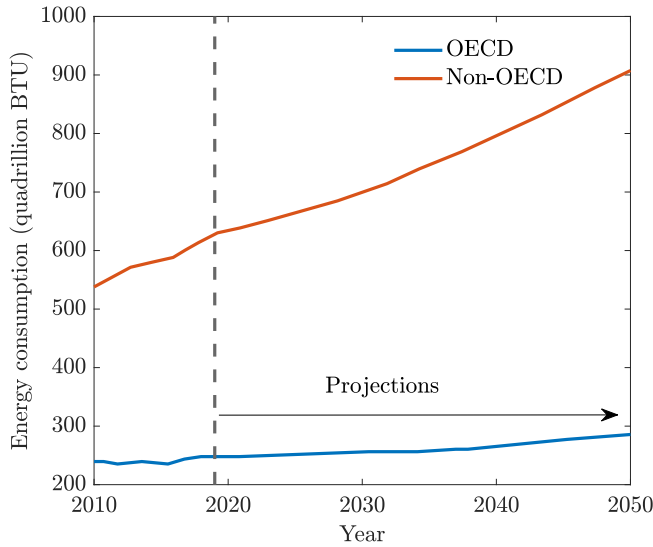


Figure 1.1: World energy consumption. The values from 2019 onward is based on projections in EIA(2020) [5].

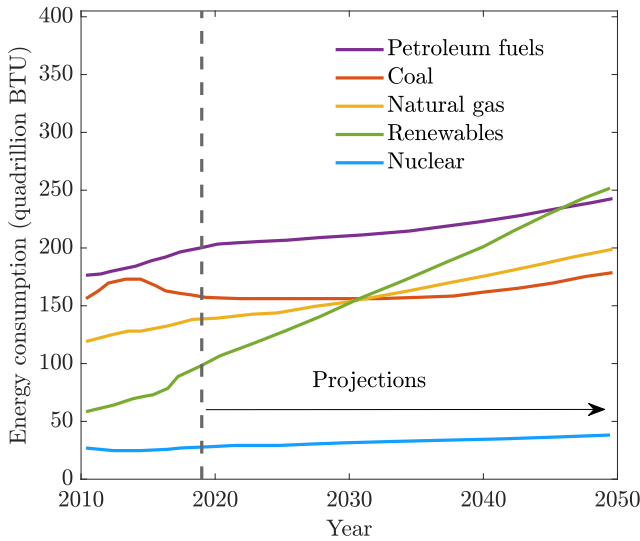


Figure 1.2: Primary global energy consumption by energy source. The values from 2019 onward are based on projections. The graph is based on the international energy outlook by EIA(2020) [5].

reduction of at least 50% by 2030 in comparison to 1990. In order to work towards this aim, it will be essential to ensure the decarbonization of the energy system. The

European Union's (EU) Renewable Energy Directive 2018/2001/EU (RED) aims at the production and promotion of renewable energy sources in EU. It requires the EU to meet at least 32% of its total energy needs with renewable energy by 2030 [10].

Apart from the threat of global warming, the prevalent combustion methods often release into the atmosphere numerous other emissions such as carbon monoxide, nitric oxides, and soot. These emissions can jeopardize the environment and public health when the rate of their production keeps increasing with rapid industrialization.

1.2 Biogas

Carbon neutral fuels are a promising option that leads to net zero carbon addition to the atmosphere. Biogas is a promising carbon neutral fuel which can be used for domestic and industrial applications. Biogas is a combustible gas which is produced by anaerobic digestion of organic material, and is composed mainly of methane and carbon dioxide. The combustion of biogas to generate electricity and heat can contribute towards the EU's 32% goal for 2030. In the Netherlands, there is an ongoing debate around the viability of energy from biomass. On one hand it is extremely important to mitigate the climate change and to meet the renewable energy goals [11]. On the other hand, bioenergy is seen as the least valuable utilization of biomass [12]. Alternative thermal conversion processes can lead to more valuable product stream (syngas, bio-oil, chemicals). Biogas production is a good option for utilizing waste streams from sources which are agricultural, municipal, food waste, manure and sewage [13]. A major drawback of biogas as fuel for combustion is its low calorific value for use in conventional burners. In conventional modes of combustion, biogas gives weak unstable flames [14]. The process of CO₂ removal from biogas to improve its calorific value remains too expensive to be practically viable [15].

This thesis aims at investigating the non-premixed combustion of methane based fuels such as biogas, using numerical modeling approaches, that can aid in the development of highly efficient and low emission burners.

1.3 Flameless or MILD combustion

In order to meet the energy demand for economic growth and at the same time reduce negative ecological effects, new energy conversion technologies are emerging, aiding the transition from fossil fuels to future sustainable fuels such as biogas. Flameless combustion, which is considered a clean and efficient combustion technology of the 21st century, can be effective in utilizing low calorific value fuels such as biogas with low emissions and high thermal efficiency [16].

Since the 1970s, most of the investigations on combustion were aimed at improving performance by reducing energy waste. With the conventional industrial combustion technology, a considerable amount of the heat input is lost through flue-gases at high enthalpy. The use of heat recovery was found to be effective in increasing energy efficiency and thereby obtaining excellent combustion perfor-

mance. Extensive research was conducted on so-called excess enthalpy combustion, leading to the development of recuperative and regenerative burners, among which regenerative systems offered a significantly higher preheating levels, of up to 1200°C and a higher thermal efficiency [17, 18].

In 1989, an experimental burner that used natural gas as fuel and preheated air at 650°C as oxidizer showed complete fuel consumption without a visible flame, with approximately zero NO_x emissions at a furnace temperature of 1000°C. The technique used in this burner was called Flameless Oxidation (FLOX) [17]. This development was followed by combustion technologies that employ preheated and diluted air such as, Highly Preheated Air Combustion (HPCA) [19], High Temperature Air Combustion (HiTAC) [18], and Colorless Distributed Combustion (CDC) [20]. These technologies have many features in common and are generally called 'flameless combustion'. Two fundamental conditions to achieve the flameless regime were found to be, 1) the temperature inside the combustion chamber should be above the auto-ignition temperature of the fuel-oxidizer mixture, and 2) the ratio of fuel and oxidizer to exhaust gas or, the recirculation ratio should be higher than 3 and smaller than 10, where the recirculation ratio K_v is defined as;

$$K_v = M_e / (M_f + M_a) \quad (1.1)$$

where M_e is the recirculated mass flow rate, M_f the fuel mass flow rate, and M_a is the mass flow rate of air. Figure 1.3(a) shows the various combustion regimes as a function of the recirculation ratio and the furnace temperature [17]. The regime for stable combustion indicates that stable conventional flames are achieved up to 30% recirculation, above which the flames start to be unstable and are prone to blow out. The latter regime is marked as unstable flame in the diagram. When the furnace temperature is higher than the autoignition temperature of the fuel-oxidizer mixture, and at high degrees of recirculation with $K_v \geq 3$, the flame starts to stabilize again in the regime that is highlighted in green, which corresponds to the flameless mode. An example for a burner design that employs exhaust gas recirculation is shown in Fig. 1.3(b), in which the fuel and oxidizer streams are entering the furnace which is at a high temperature due to recirculation of exhaust gases. For a practical furnace to operate in this manner, first it has to be heated with a conventional flame and then a transition has to occur with recirculation of the exhaust gas to achieve the flameless mode. The conditions put forth by Cavaliere and de Joannon [21] for achieving what they define to be 'Moderate/Intense Low oxygen Dilution' (MILD) combustion in the context of a Perfectly Stirred Reactor (PSR) are, 1) inlet temperature of the reactants are above the autoignition temperature for a given reactant mixture, 2) the temperature rise is smaller than the auto ignition temperature. These conditions lead to a homogenization of reactants and products and leads to a reduction in the final combustion temperature, followed by a reduction of thermal NO_x. In more recent studies, the definition of MILD or Flameless state of combustion has been subjected to further scrutiny. The definition for PSR based MILD combustion by Cavaliere and de Joannon includes flames featuring instabilities due to local autoignition and extinction. Oberlack et al. [22] proposed the definition of MILD combustion in the context of premixed flames to be the regime where sharp autoigniting and extinguishing points are absent, in-

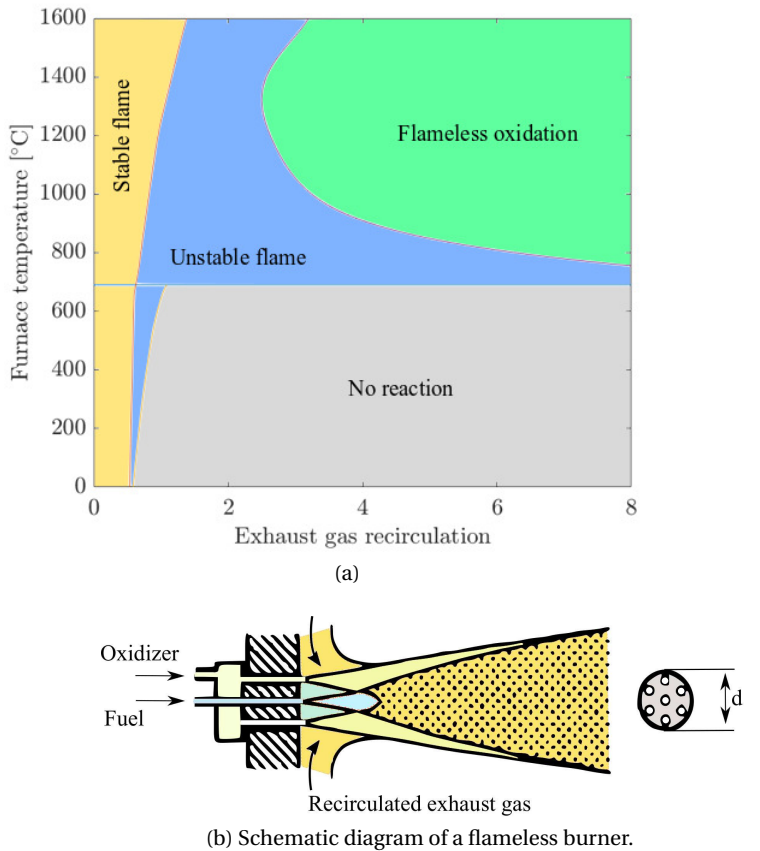


Figure 1.3: a) Regimes of combustion and b) a schematic diagram of a flameless burner; from Wünniger & Wünniger [17]

stead a gradual combustion of reactants takes place. Evans et al. [23] extended this definition to the non-premixed regime, and made a distinction between autoigniting flames and MILD flames, in such a way that MILD flames do not exhibit clear autoignition or extinction in the flame structures of non-premixed systems but display a gradual combustion. For the same fuel-oxidizer composition all three definitions fundamentally depend on the initial temperature and the temperature rise. Again, the original definition by Cavaliere and de Joannon [21] characterizes the MILD combustion regime with a low temperature rise between initial and final state of reactants, and the initial temperature of the reactants surpassing the activation energy barrier. The definitions by Oberlack et al. and Evans et al. describe the MILD regime in terms of gradual heat release from the reactants without abrupt local ignition or extinction events.

A prominent variable for characterizing the flame regimes is the Damköhler number Da , which is defined as the ratio of flow time to reaction time. Cavaliere and de Joannon [21] assume $Da \ll 1$ implying slow reactions relative to the flow

time, which simplifies the study by neglecting the effects of turbulence-chemistry interaction. Another study by Khalil and Gupta [20] addressed combustion in a swirl burner that achieved $Da \ll 1$ through the internal recirculation of product gases. In this case the recirculation reduces the oxygen concentration and thereby slows down the reaction chemistry relative to the flow time determined based on the integral length scale. An experimental and modeling study by Li et al. [24] showed that the MILD regime falls approximately within the range of $Da = 0.01$ to $Da = 5$, indicating that MILD flames fall in the regime where both flow and reaction time scales play a role. For non-premixed burners, the turbulence-chemistry interaction is of low importance away from the burner exit. However, the creation of diluted mixture of fuel, oxidizer and products close to the burner exit must be described by taking turbulence-chemistry interaction in to account. DNS studies on MILD combustion [25–27] have shown the presence of strong thin quasi-1D flame surfaces also known as flamelets, distributed throughout the computational domain showing that in fact locally $Da > 1$. The use of a 1D flamelet representation of complex 3D flames reduces computational cost significantly. However the question remains in which situations a MILD flame can be characterized with the flamelet representation. There is no conclusive method to link burner design to flame regime in different experimental set-ups, which makes the convergence to a single and clear definition of MILD combustion a difficult and open problem.

Experimental studies

MILD combustion has been subjected to experimental studies using flow reactor type burners [28–30] for characterizing the chemical kinetic features and the fluid mechanics. With practical applications in mind, several burner configurations with internal recirculation have been studied for gaseous and liquid fuels [31–35]. A widely used experimental setup for studying MILD combustion in turbulent jet flames is the Jet in Hot Coflow (JHC) configuration. The JHC flame configuration consists of a central fuel jet within a coflow of oxidizer that is preheated and diluted with combustion products. It presents an opportunity to study MILD and/or autoigniting flame behavior by lowering the oxygen concentration in the coflow, without having the recirculation of combustion products. The open and axisymmetric configuration of JHC simplifies the measurements with greater access for diagnostics. A review paper by Perpignan et al. [36] summarizes the various studies on JHC flames that uses gaseous fuels. Dally et al. [37] performed the first set of experiments on a JHC burner, also known as the Adelaide JHC burner, to investigate MILD combustion. A mixture of methane and hydrogen was used as the fuel in this JHC under constant coflow temperatures and fuel jet Reynolds number Re . Three levels of oxygen concentration (3%, 6% and 9%) were applied in the coflow stream of this burner. The reduction in oxygen concentration to 3% showed a significant change in the flame behavior from that with 9% in terms of lowering OH and NO formation. According to a later theoretical analysis by Evans et al. [38], this study captured the transition from autoigniting at 9% to MILD regime at 3% O_2 in the coflow. Medwell et al. [39] further extended this study by simultaneously measuring OH and CH_2O concentrations and temperature, at two coflow O_2 levels and 3 different jet Re numbers. This study showed that at 3% O_2 in the coflow,

a suppression of OH levels takes place along with an increase in CH_2O . Cabra et al. [40] previously developed a JHC arrangement with considerably large O_2 concentration in the coflow known as the Cabra vitiated coflow burner, on which they performed a study of lifted turbulent jet flames using H_2 and CH_4 /air mixture as the fuel. Gordon et al. [41] measured OH and CH_2O on the Cabra burner, and showed that the autoignition structures corresponded with an igniting laminar 1D flame. The Cabra flame however, did not really belong in the MILD regime because of the too high oxygen content in the coflow. Oldenhof et al. [42–45] conducted an extensive series of experiments on the Delft-Jet-in-Hot-Coflow (DJHC) burner discovering the formation of autoignition kernels, the role of entrainment in flame stabilization. The transient response of the burner during starting was also studied. Figure 1.4 shows a schematic diagram of the DJHC experimental set-up.

JHC experiments have subjected a number of gaseous fuels to investigation in the context of MILD combustion. On the Adelaide JHC burner $\text{CH}_4 - \text{H}_2$ mixture was studied first [37, 39], followed by $\text{C}_2\text{H}_4 - \text{H}_2$, $\text{C}_2\text{H}_4/\text{N}_2$, and $\text{C}_2\text{H}_4/\text{Air}$ [46]. The main difference between CH_4 and C_2H_4 is their reactivity due to the C_2 bond in ethylene, which also shows a high sooting tendency in conventional flames. Under MILD conditions, the flame stabilization mechanism was shown to be fundamentally different from conventional combustion, along with soot suppression for C_2H_4 . Further, Evans et al. [38] studied fuel blends of $\text{CH}_4 - \text{C}_2\text{H}_4$ in the Adelaide burner which showed a higher sensitivity of lift-off height for blends with $> 50\%$ C_2H_4 to coflow temperatures than for mixtures with $> 50\%$ CH_4 . Cabra et al. [47] studied the flame behavior of a $\text{H}_2 - \text{N}_2$ mixture in the Cabra burner, and further studied the lifted flame behavior of $\text{CH}_4 - \text{H}_2 - \text{O}_2 - \text{H}_2\text{O}$ in the same burner [40], and found autoignition to be a significant factor for flame stabilization. The Delft JHC burner was used to study the MILD combustion of CH_4 by Oldenhof et al. [42]. In the DJHC experiments, Dutch natural gas (DNG) was used in place of CH_4 . Arteaga et al. studied a mixture of $\text{CH}_4 - \text{H}_2$ [48] and found that the flame lift-off reduces with the increase in the fraction of H_2 . Sarras et al. [49] investigated DNG/ $\text{CH}_4 - \text{CO}_2$ fuel mixtures that are representative of biogas. The addition of CO_2 to CH_4 resulted in a reduction in the flame length. However, the impact on the flame lift-off was negligible. The experimental research on MILD combustion is ongoing along with computational modeling studies. To develop practical burner designs and for the understanding of the MILD regime, robust combustion models are needed. Computational modeling provides insights on the flame behavior and the variables that are not measured in experiments. A major challenge in the modeling of MILD combustion is that the physics of autoignition, flame propagation, interaction of flame fronts, mixing, recirculation, and turbulent-chemistry interaction adds up to a high level of complexity. To develop a model that can capture these aspects in future, we must have a clear understanding of their interplay through continued experimental and modeling research.

1.4 Numerical studies on JHC flames

Modeling MILD flames in the JHC configuration reduces the computational complexity by avoiding recirculation. The comparison between experimental measure-

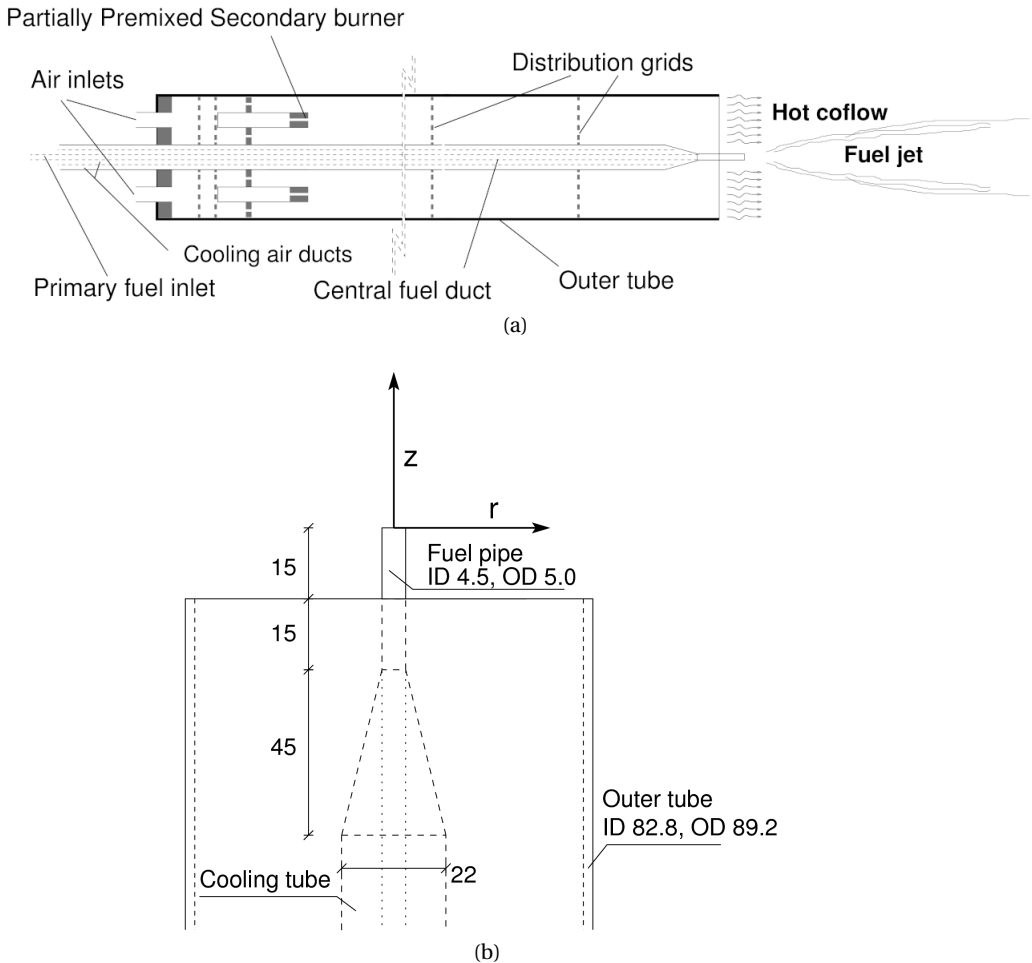


Figure 1.4: Delft Jet in Hot Coflow burner setup [42].

ments and computational data at various stages of mixing, ignition and stabilization of flames provides insights to validate the computational models. A complete description of turbulence is obtained by the Direct Numerical Simulation (DNS) approach, which also provides fully three-dimensional information on the dynamics of the flame lift-off height in case of JHC flames. A lifted hydrogen jet flame in JHC configuration was studied using DNS by Yoo et al. [50]. In their study, the fuel was a mixture of hydrogen and nitrogen, with heated air as coflow. Auto-ignition was found to be the key mechanism for flame stabilization in this case. DNS studies, however, come at a cost of high computational power requirement, due to which it has limited applicability in complex technical burner configurations. LES simulations on the other hand resolve large scale flow structures, and use closure assumptions for transported scalars and turbulence in small scales. A major challenge in modeling combustion in practical burner configurations is ac-

counting for the numerous reaction pathways and reaction rates which leads ultimately to heat release and transformation of thermo-physical properties. Detailed reaction mechanisms lead to chemical stiffness due to a large number of species and reaction time scales, and skeletal reaction mechanisms might lead to omitting significant reaction pathways in MILD combustion. LES simulations of JHC burners give physical insights into the flame, however incorporating the detailed reaction kinetics and its interaction with turbulence is highly challenging. Detailed reaction chemistry can be incorporated in LES simulations by using tabulated chemistry methods. Flamelet based models, such as the Flamelet Generated Manifold (FGM) [51] and Flamelet Progress Variable approach (FPV) [52] tabulate the thermochemical properties and reactive species from laminar diffusion flame structures underlying a turbulent flame, using controlling variables such as mixture fraction Z to indicate the degree of mixing between fuel and oxidizer, and reaction progress variable \mathcal{V} . Along with flamelet based models, statistical models for turbulence chemistry interaction such as transported PDF approach [53], Conditional Moment Closure (CMC) [54] and Conditional Source Estimation (CSE) [55] have been successfully employed in LES of JHC flames. Abtahizadeh et al. [56] applied an Igniting Mixing Layer (IML) based FGM to simulate the DJHC flame with methane-hydrogen mixture as fuel. The turbulence-chemistry interaction was modeled in this case using a presumed beta pdf assumption. This approach will serve as the baseline for LES studies presented in this thesis. The FGM approach has been widely used in computational studies of JHC flames due to the low computational cost relative to the accuracy of simulations. An important challenge in the application of this approach is determining a progress variable (\mathcal{V}) that can effectively represent the underlying detailed flamelet chemistry. \mathcal{V} is defined as a combination of mass fractions of chosen chemical species in the detailed reaction chemistry [52, 56, 57]. In case of MILD combustion the choice of a progress variable gets trickier as the product species, usually considered for formulating the progress variable, are already present in the oxidizer stream and therefore a significant change in the progress variable may not occur during ignition. Medwell et al. [46] observed a preignition stage in the lifted region in a JHC flame, where the short-lived precursors to ignition form with no significant change in reactant or product concentrations. The inclusion of the precursor species can lead to loss of accuracy in the oxidation stage, where they are consumed away. Thus, lifted igniting flames in JHC is not easy to predict accurately using manually chosen definition of \mathcal{V} . As an opposed to manually chosen \mathcal{V} , developing an approach for automating the formulation of \mathcal{V} is in scope of this thesis.

The overarching goal of this thesis is to investigate MILD combustion of methane based fuels such as biogas in non-premixed systems through numerical studies. These numerical studies are designed to identify the role of various physical parameters as well as the effectiveness of various numerical modeling strategies in representing the physics of MILD combustion.

Overview of research objectives

In this thesis the following questions on the physics and the numerical modeling of MILD combustion are addressed:

Ignition in MILD combustion

- What: Autoignition is one of the core features of flame stabilization in MILD flames. What is the relationship of ignition delay of biogas (mixture of CH_4 and CO_2) to the temperature and oxygen concentration of the oxidizer in a MILD environment? How is ignition delay affected by the concentration of CO_2 in biogas?

How: In Chapter 2, the ignition behavior of biogas is studied in transient reaction-diffusion structures using mixtures of CH_4 and CO_2 , with varying proportions of CO_2 as fuel and oxidizer at varying concentration of O_2 for a range of temperatures.

Flamelet Generated Manifold Manifold Approach

- What: The reaction chemistry in turbulent jet-in-hot-coflow simulations will be modeled using the FGM approach. In FGM the reaction progress variable must ideally have a one-to-one mapping with the evolution of various chemical species, and must reproduce the ignition delay as predicted from one dimensional simulations with detailed chemistry. It is not guaranteed that a conventional definition of the reaction progress variable can accurately reproduce the predictions of detailed chemistry simulations. Therefore, finding a reaction progress variable is not always trivial. How to determine a progress variable formulation that is applicable for a non-premixed system which reproduces the ignition delay predictions from detailed chemistry simulations?

How: In Chapter 3, a novel methodology for computing an automated progress variable combination is discussed. It uses a multi-objective optimization method to obtain a progress variable formulation for a given set of igniting flamelets. It includes an accurate description of chemical the pre-ignition phase. Predicted ignition delays and species mass fractions with detailed chemistry and FGM are compared and analyzed to assess the accuracy of automated progress variable definition in each case.

Application of FGM to wide range of JHC Experiments

- What: Numerical simulation of combustion in JHC burners; What is the influence of (i) preheating and dilution of the oxidizer, (ii) fuel composition/dilution, and (iii) fuel jet Reynolds number on the flame stabilization in JHC burners? Which FGM based modeling strategy is desirable in case of different JHC burners?

How: In Chapter 4, the Cabra vitiated coflow burner and DJHC burner are investigated using LES, with FGM to model the reaction chemistry and a presumed PDF approach to model turbulence-chemistry interaction. The flame stabilization behavior is investigated with different modeling options and fuels. The results are analyzed and compared with the experimental measurements for validation of the chosen modeling methods.

Chapter 2

Auto Ignition of Biogas in MILD Non-premixed Combustion Systems

Abstract

The ignition delay of biogas in mixing layers is investigated using a one dimensional combustion model, with its application to Moderate or Intense Low oxygen Dilution (MILD) combustion being the focus. The current study reveals the key aspects of the ignition of biogas in a non-premixed, igniting mixing layer with a hot oxidizer of low oxygen content. The observed characteristics are contrasted against the existing studies on ignition in homogeneous mixtures under similar conditions. Biogas is considered here as a mixture of CH_4 with variable amounts CO_2 . The influence of reactive, thermal and transport properties of CO_2 on the ignition is evaluated using artificial species to mimic the respective characteristic of CO_2 . While the ignition delay in homogeneous mixtures shows a strong dependence on CO_2 content in the fuel, the ignition delay predictions from one-dimensional mixing layers show no significant influence of CO_2 levels in biogas. In addition, the influence of oxidizer composition and temperature on the ignition delay is determined for CO_2 levels ranging from zero to 90%. A sensitivity analysis of chemical reactions on the ignition delay shows a negligible effect of CO_2 concentration in biogas. The current study emphasizes the role of oxidizer composition and temperature on the ignition characteristics of a MILD biogas flame.

This chapter closely follows the paper “Numerical Study on the Autoignition of Biogas in Moderate or Intense Low Oxygen Dilution Non-premixed Combustion Systems” by Vasavan et al. [58].

2.1 Introduction

Biogas can be considered as a carbon neutral fuel when it has its origins in the anaerobic digestion of organic matter by living organisms. The major components that make up biogas are methane and CO_2 . Due to the presence of a considerable amount of CO_2 the biogas has a low calorific value. In spite of this, biogas is a promising candidate to meet the energy targets set by the European Union due to its flexibility as an energy source and its wide range of applications including heating and electricity production [59]. It is widely accepted to be a sustainable fuel for household as well as industrial applications despite challenges with production and implementation [60]. Still, at present its industrial applications are limited due to low heating value and variable composition of biogas often containing corrosive components such as H_2S [61]. It is not an easy task to ensure the production of biogas with a fixed composition by virtue of its biological origin. The variation in the

composition of biogas coupled with its low heat release rate could reduce the thermal efficiency of engines [62]. The application of biogas in engines was reviewed in [63]. For engine relevant conditions, the ignition delay trend with respect to CO_2 level has been predicted from the studies on ignition of homogeneous mixtures of biogas with air [64], given that in engine applications biogas is premixed with air. However, for the ignition of biogas in non-premixed systems where the fuel and oxidizer are initially separated, only limited literature is available in authors' knowledge. It is therefore important to extend our knowledge on the influence of biogas composition changes in non-premixed systems.

For applications such as fueling industrial furnaces, the environmental impact of exhaust gases is a major concern provided that there is a considerable amount of NO_x released from conventional burners and so is the carbon footprint left by the fuel consumption [65]. Moderate or intense low oxygen dilution (MILD) combustion has been a subject in a number of studies for its potential to deliver high thermal efficiency with lower pollutant emissions [21, 37, 42]. For achieving MILD combustion, the gas flow has to be kept above the autoignition temperature of the fuel. The fuel is burned under strong mixing in a hot, low oxygen environment. The heat release rate of combustion can be lower than conventional feed-back stabilized combustion, provided a hot-diluted environment is maintained. Hence furnaces operating in the MILD mode can run on fuels such as biogas with a low heat content. The peak temperatures attained are lower than conventional burners, which yields a substantial reduction in the thermally generated NO_x [66]. MILD combustion is materialized in practical burners of various configurations [67–70] that differ in flame structures and stabilization mechanism. MILD combustion of biogas has been studied using the Delft Jet-in-Hot-Coflow (DJHC) burner, which is a laboratory scale burner that mimics MILD combustion conditions where the fuel jet is issued into a hot coflow of lean combustion products [42]. Oldenhof et al. [43–45] performed experiments on the DJHC burner with natural gas as the fuel and Sarras et al. [49] studied the influence of mixing CO_2 with natural gas. The combination of CO_2 and natural gas mimics biogas, except for the presence of trace amounts of ethane and higher alkanes in natural gas. From these studies the stabilization of JHC flames is found to be dependent on the formation and propagation of autoignition kernels. The ignition delay for methane diluted with CO_2 was experimentally measured for homogeneous mixtures with air by Zeng et al. [64]. Their study focused on the ignition of mixtures with equivalence ratio 0.5, 1 and 2, for a temperature range of 1300 – 2100 K and pressure range of 0.1 – 1 MPa. It was shown that an increase in dilution by CO_2 or N_2 has an inhibitory effect on ignition delays at every equivalence ratio. This effect is stronger for dilution with CO_2 than N_2 . Their numerical investigation showed that the ignition of methane/air mixtures is sensitive to reactions involving H, O and OH radicals. With increase in CO_2 or N_2 in the mixture, reactions promoting the ignition were found to be inhibited. Fischer and Jiang [71] performed a computational study on the ignition of homogeneous $\text{CH}_4\text{-CO}_2\text{-O}_2$ mixtures and compared the ignition delays predicted by five different reaction mechanisms against the results from shock tube experiments. Their study showed that among the five, GRI Mech 3.0 [72] delivered the best predictions for the ignition delays of $\text{CH}_4\text{-CO}_2$ mixtures.

It has to be realized that in a JHC burner the reactants are not premixed. A

DNS study on the fine structure of turbulent MILD combustion of methane by Doan et al. [26] has shown that the non-premixed combustion mode is relevant even if the initial mixture is partially premixed. Hence, studies on MILD flames under non-premixed conditions become necessary to understand their ignition and combustion behavior[73]. Sidey and Mastorakos [74] studied the effect of adding CO₂ with methane in steady diffusion flames under MILD conditions. The effect of strain rate on the flame structure and maximum temperature was studied along with the extinction behavior. Wang et al. [75] investigated the chemical and physical aspects of adding CO₂ to CH₄ in steady counterflow diffusion flames. The CO₂ presence was found to reduce the flame temperatures and increase the CO production by reducing its rate of oxidation into CO₂. These studies on steady diffusion flames provide insights regarding the flame structures, flame quenching and pollutant formation, and help in understanding the interplay of chemistry in MILD non-premixed flames. However, the ignition in non-premixed systems was not clearly addressed which is a key aspect in the flame stabilization in MILD burners.

A one dimensional Igniting Mixing Layer (IML) [56, 76, 77] serves as the simplest physical representation of a non-premixed system. The present study aims at investigating the ignition of methane and biogas under MILD conditions through IML simulations. The range of boundary conditions applied in the current study is based on the Delft JHC studies with Dutch Natural Gas (DNG) [42] and biogas-like fuels [49]. It was found in [49] that addition of CO₂ did not result in a considerable change of the lift-off height of a natural gas flame, which seems to contradict the findings from studies on homogeneous mixtures where CO₂ affects the ignition delays substantially. It was further suggested that the addition of CO₂ to natural gas in a JHC may result in a counteracting mechanism of slower ignition chemistry against the increased turbulent entrainment of hot oxidizer, that maintains the lift-off heights at the same level. The influence of CO₂ on ignition is also addressed in the current study. The main objectives of this study are summarized as,

- To study the ignition and flame development in an IML, and to identify the most sensitive reactions that influence the ignition delay.
- To investigate the effects of CO₂ content in the fuel on ignition delay of methane/natural gas and to assess the influence of thermo chemical properties of CO₂ on biogas ignition.
- To examine the dependence of ignition delay on the oxidizer temperature and oxygen level for CH₄ and CH₄ – CO₂ mixtures.

In the following section the computational methodology is presented, the results of IML simulations are discussed next, along with the inferences from sensitivity analysis, followed by the conclusions from the study.

2.2 Computational method

The physical and chemical processes in a MILD flame (e.g. Jet-in-hot-co flow) are very similar to those in an Igniting Mixing Layer (IML). An IML is a time dependent reaction-diffusion layer [56, 77, 78], where the diffusive transport and reactive

processes occur simultaneously from an initial unmixed state, which represents a pocket of fuel issuing from the jet and mixing with the hot oxidizer, leading to its ignition. As shown in Figure 2.1, at time $t = 0$ for $x < 0$ the local thermo-chemical properties describe the fuel flow and for $x > 0$ they correspond to the oxidizer conditions. Due to the steep initial gradients in concentration of fuel and oxidizer, in the absence of an applied strain, the mixing is governed entirely by diffusive fluxes. The scalar gradients dissipate with time and the reactive-diffusive processes asymptotically approach a state of chemical equilibrium at $t \rightarrow \infty$. In

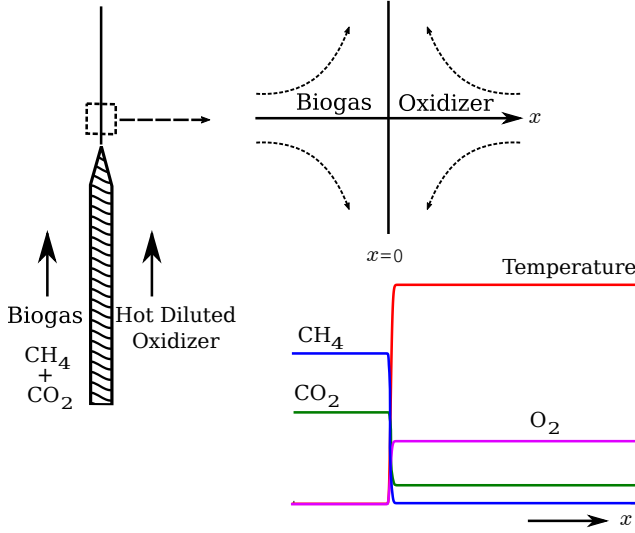


Figure 2.1: Schematic diagram of the case set up for IML, representing the initial profiles of the major species and temperature.

the present study, IML is modeled as a time dependent 1D counterflow flame with a low strain rate ($a = 10 \text{ s}^{-1}$). That is, from an initially unmixed state, the mixing layer approaches a steady state counterflow flame with $a = 10 \text{ s}^{-1}$. The application of strain rate makes it possible to keep the flame within a physical domain of finite size and to achieve a steady state condition in approximately 1 s. This approach is different from an Igniting Counterflow Flame (ICF) [79] where the reactive process starts from a steady non-reacting counterflow solution with an applied strain rate, where the time dependent changes in scalar dissipation rate is not considered. An IML is expected to mimic a MILD flame than ICF for this reason. The transport equations that describe a one-dimensional unsteady counterflow are given by [80]

$$\frac{\partial \rho}{\partial t} + \frac{\partial \rho u}{\partial x} = -\rho G, \quad (2.1)$$

$$\rho \frac{\partial Y_i}{\partial t} + \rho u \frac{\partial Y_i}{\partial x} - \frac{\partial}{\partial x} \left(\rho U_i \frac{\partial Y_i}{\partial x} \right) - \dot{w}_i = 0, \quad (2.2)$$

$$\rho \frac{\partial h}{\partial t} + \rho u \frac{\partial h}{\partial x} - \frac{\partial}{\partial x} \left(\frac{\lambda}{c_p} \frac{\partial h}{\partial x} \right) = \frac{\partial}{\partial x} \left(\sum_{i=1}^{N_{\text{sp}}} h_i \left(\rho Y_i U_i - \frac{\lambda}{c_p} \frac{\partial Y_i}{\partial x} \right) \right), \quad (2.3)$$

Table 2.1: Summary of computational set up

Parameter	Values
x range	[-1 : 2.5] cm
Time step	Variable time stepping [10^{-8} : 10^{-4}]s
Number of grid points	500 (with adaptive grid refinement)
Fuel composition (moles)	$(1 - X_{\text{CO}_2}) \text{CH}_4 + X_{\text{CO}_2} \text{CO}_2$
Fuel temperature	450 K
Oxidizer composition	Vitiated air with $Y_{\text{O}_2, \text{ox}} = 0.04$ & 0.06 (details are available in table 2.3)
Oxidizer temperature	1200 - 1600 K
Reaction mechanism	GRI-Mech 3.0
Transport model	Mixture averaged

where ρ , c_p , λ and μ stand for mass density, specific heat at constant pressure, thermal conductivity and viscosity, respectively. U_i represents the diffusion velocity and u the velocity in x direction. Y_i and \dot{w}_i are the mass fraction and chemical production rate ($\text{kg}/\text{m}^3\text{s}$) of the i^{th} species where i ranges from 1 to N_{sp} , the total number of species. The momentum balance in counterflow configuration is modeled after Dixon-Lewis [80] through solving a transport equation for G (Eq.(2.4)), the tangential velocity gradient or strain rate:

$$\rho \frac{\partial G}{\partial t} + \rho u \frac{\partial G}{\partial x} - \frac{\partial}{\partial x} \left(\mu \frac{\partial G}{\partial x} \right) = J - \rho G^2. \quad (2.4)$$

Here $J = \rho_{\text{ox}} a^2$, with a being the applied strain rate and ρ_{ox} the density at the oxidizer side. The computational time is set to 1 s within which the flame attains a near steady state. It is assumed that the hot diluted oxidizer is at chemical equilibrium. The oxidizer composition is computed as a constrained chemical equilibrium solution for a given temperature and oxygen level.

In theory, the initial condition for IML can be modeled as a Heaviside function. However, the numerical scheme for resolving diffusive fluxes uses a finite spatial and temporal spacing. Therefore the Heaviside solution is replaced with a smooth initial condition obtained from a steady counterflow solution with a high applied strain which approximates a Heaviside function. In the current case the initial condition is computed as a steady counterflow solution with $a = 10^4 \text{ s}^{-1}$. This applied strain rate is sufficiently high, so that the flame is quenched and initial the mixing layer thickness is of the order of $100 \mu\text{m}$. Subsequently, the strain rate $G(x)$ is rescaled based on $a = 10 \text{ s}^{-1}$ and the corresponding mass flux ρu is updated for every grid point in the domain based on the steady state mass conservation,

$$\frac{\partial \rho u}{\partial x} = -\rho G. \quad (2.5)$$

Using the initial profile thus obtained, an unsteady simulation is performed using the one-dimensional flame code CHEM1D [81]. The code uses adaptive mesh refinement in combination with variable time stepping. The results are verified

to be independent of mesh size and time step size. For the analysis of the IML flamelets, Bilger's definition of mixture fraction Z is used, which is given as,

$$Z = \frac{0.5M_{\text{H}}^{-1}[Z_{\text{H}} - Z_{\text{H},2}] + 2M_{\text{C}}^{-1}[Z_{\text{C}} - Z_{\text{C},2}] - M_{\text{O}}^{-1}[Z_{\text{O}} - Z_{\text{O},2}]}{0.5M_{\text{H}}^{-1}[Z_{\text{H},1} - Z_{\text{H},2}] + 2M_{\text{C}}^{-1}[Z_{\text{C},1} - Z_{\text{C},2}] - M_{\text{O}}^{-1}[Z_{\text{O},1} - Z_{\text{O},2}]} \quad (2.6)$$

where Z_{H} , Z_{C} , and Z_{O} are the elemental mass fractions of hydrogen, carbon and oxygen respectively. M_{H} , M_{C} , and M_{O} are the corresponding atomic masses.

A number of cases with varying fuel and oxidizer boundary conditions is simulated. Table 3.1 gives a concise overview of the computational set up. On the oxidizer side the temperature T_{ox} is varied from 1200 – 1600 K and the oxygen level ($Y_{\text{O}_2,\text{ox}}$) is varied between 2 – 16% by mass. Table 2.3 in the Appendix shows more detailed data. The ranges of $Y_{\text{O}_2,\text{ox}}$ and T_{ox} are chosen based on the oxygen percentage and temperature in the co-flow of the DJHC experiments [42]. The Table 2.3 also gives the mass fractions of major species in the oxidizer and the stoichiometric mixture fraction Z_{st} . The fuel is chosen as methane for the reference case and, for the biogas study, the CO_2 mole fraction is increased from 0 to 90% with the rest being methane. The fuel temperature is chosen as 450 K for all simulations as observed in the DJHC burner [42]. All simulations are performed at atmospheric pressure. A mixture-averaged diffusion transport model [81] is used along with the GRI 3.0 mechanism for reaction chemistry. It was shown in multiple numerical studies that GRI 3.0 gives accurate predictions of ignition delay for biogas-like fuel combinations [64, 71].

2.3 Results and discussion

First, the characteristics of ignition in an IML are discussed and a comparison of IML is made against ICF. Further, the ignition delay trends for methane and biogas are estimated for a range of CO_2 levels. The impact of CO_2 on the ignition delay of biogas is assessed by introducing artificial species to isolate the effects of chemical, transport and thermal properties of CO_2 . The impact of oxidizer composition and temperature are estimated thereafter. The sensitivity of ignition reactions to the amount of CO_2 in biogas is analyzed under the IML configuration.

2.3.1 Structure of IML and comparison with ICF

The evolution of a mixing layer from an unmixed initial condition towards a steady diffusion flame involves a series of mutually dependent chemical and thermal events under a continuously decaying scalar dissipation in the domain. This includes the pre-ignition chemistry, ignition and heat release followed by diffusive flame spreading. In Figure 2.2(a) the time-dependent mixture fraction (Z) profiles from $t = 0$ to 0.1 s in a 1D IML are shown. The fuel considered here is methane and the oxidizer has 8% O_2 by mass, and a temperature of 1540 K. Figure 2.2(a) shows the progressive mixing of the initially unmixed fuel and oxidizer, proceeding towards a well mixed state. During the mixing process the hot oxidizer reacts with the fuel releasing heat and the corresponding temperature profiles are shown in

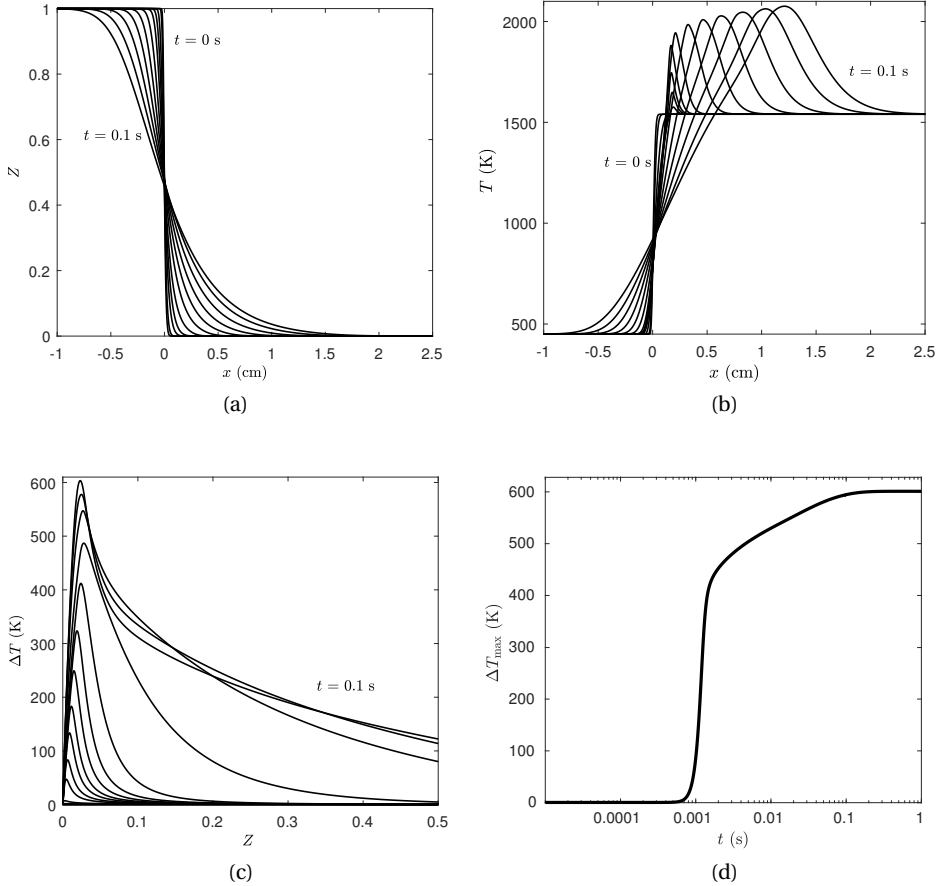


Figure 2.2: Time dependent characteristics of IML, (a) mixture fraction and (b) temperature profiles, (c) temperature rise ΔT against Z and (d) maximum temperature rise ΔT_{\max} against time t . Plots in (a), (b) and (c) are corresponding to time $t = 0$ to 0.1 s.

Figure 2.2(b). The temperature rise is defined as $\Delta T(Z, t) = T(Z, t) - T(Z, t = 0)$. In Figure 2.2(c) $\Delta T(Z, t)$ is plotted against Z , it shows the temperature rise starting from a location with Z close to 0, and growing to reach a maximum of 600 K near the stoichiometric mixture fraction, $Z_{\text{st}} = 0.02$. The time-dependent variation in the maximum temperature in the domain, ΔT_{\max} is shown in Figure 2.2(d). It shows a pre-ignition phase where the temperature rise is slow, up to $t \approx 10^{-3}$ s and thereafter ΔT_{\max} shoots to a maximum of $\Delta T_{\max} \approx 600$ K owing to a rapid heat release following ignition. Ignition delay under MILD conditions has shown good agreement with a temperature rise threshold of 10 K as it correlates well to the onset of chemiluminescence [82]. Hence in this study the ignition delay (τ_{ig}) is defined as the time for achieving $\Delta T_{\max} = 10$ K. The value of Z at which this ΔT_{\max}

is attained is denoted as the most reactive mixture fraction, Z_{mr} .

Autoignition in an IML is governed by reaction and diffusion processes. An unsteady diffusion flame with unity Lewis number is described by the unsteady flamelet equation for temperature as [83],

$$\rho \frac{\partial T}{\partial t} = \dot{\omega}_T + \frac{1}{2} \rho \chi \frac{\partial^2 T}{\partial Z^2}, \quad (2.7)$$

where $\dot{\omega}_T$ is the source term for temperature from the chemical reactions. The second term in the RHS corresponds to the diffusive transport, with χ being the scalar dissipation rate given by,

$$\chi = 2D \left(\frac{\partial Z}{\partial x} \right)^2 \quad (2.8)$$

where D is the scalar diffusivity which is equal to $\frac{\lambda}{\rho C_p}$ for unity Lewis number. A high scalar dissipation delays ignition in non-premixed systems [84]. For an IML with a Heaviside initial condition, the expression for χ is obtained as [83],

$$\chi_{\text{th}}(Z, t) = \frac{1}{2\pi t} e^{-2[\text{erfc}^{-1}(2Z)]^2}, \quad (2.9)$$

which indicates that $\chi \propto t^{-1}$. In order to understand the influence of χ on ignition, the IML under consideration is compared against an ICF with the same fuel and oxidizer boundary conditions and with a strain rate of 10 s^{-1} . In Figure 2.3(a) the values of χ at Z_{mr} and Z_{st} are plotted against time for IML and ICF. Theoretically the values of χ in an IML approach infinity at $t = 0$ as the mixing layer thickness, δ_{th} , is infinitesimally thin. In this log-log plot, χ_{th} follows a straight line with negative slope starting from a magnitude that tends to infinity at $t = 0$. In the current simulations, the mixing layer thickness δ varies from an initial value, $\delta_{Z,\text{initial}} = 0.5 \text{ mm}$ to $\delta_{Z,\text{final}} = 25 \text{ mm}$. Therefore, the initial values of χ are obtained to be finite and the final values are determined by the applied strain rate. The red and blue lines correspond to Z_{mr} and Z_{st} respectively. The IML closely follows the χ_{th} within the range of χ corresponding to $\delta_{Z,\text{initial}}$ and $\delta_{Z,\text{final}}$. The scalar dissipation trend in ICF remains at a constant value as expected. As the flame develops, at $t \approx 1 \text{ ms}$ the exothermic expansion causes a perturbation in χ for both cases and χ assumes a lower value following the thermal expansion.

Figure 2.3(b) shows the evolution of ΔT_Z , the temperature rise for a constant Z , in IML and ICF at Z_{mr} and Z_{st} . It can be seen here that the ignition is delayed in the case of IML due to the high value of χ . The delay between Z_{mr} and Z_{st} curves represents the time required for the flame spread. The close proximity of these curves for IML indicates a faster flame spread in the IML. As compared to ICF, IML has a higher χ during and post ignition aiding the flame spread through increased diffusive transport. This is further elucidated in Figure 2.4 that shows the heat release rate (HRR) contours as function of mixture fraction and time for ICF and IML. At ignition, there is a clear difference in HRR at Z_{mr} and Z_{st} in the case of ICF. This shows a highly localized raise in HRR and therefore temperature. In the case of IML, it takes longer to achieve the same level of heat release rate but the difference

in HRR between Z_{mr} and Z_{st} is smaller and the ignition is less localized in Z . The increased diffusive fluxes in the case of IML are shown to delay the ignition by more than two fold as compared with ICF. The ignition in IML combine the effects of decaying χ with ignition chemistry, therefore it mimics the situation in non-premixed MILD burners better, much different from ICF.

Effect of CO₂ on the ignition of biogas

The ignition of biogas under MILD conditions is estimated in IML simulations with varying levels of CO₂ in the fuel. Fuel compositions containing CH₄ with CO₂ levels that range from 0 to 90% are considered. The T_{ox} is set as 1500 K, with an O₂ mass fraction of 8% in the oxidizer. In Figure 2.5, two ignition time scales are plotted against X_{CO_2} for biogas-like fuel compositions. Ignition time scales represented here are the time for $\Delta T = 10$ K and 100 K. It shows that the ignition delay remains nearly constant for CO₂ levels up to 90% in the fuel. This trend is significantly different from experimentally reported ignition delays in shock tube experiments with uniform mixtures. The additional freedom of chemical species to diffuse across mixture fraction in the case of a non-premixed flame makes ignition far less sensitive to fuel composition when compared with homogeneous mixtures. The numerical studies on the ignition of biogas in homogeneous mixtures show CO₂ causing significant increase in ignition delays [64, 71]. In the mixing layer however, the influence of CO₂ is nearly absent. There is actually a small decrease in τ_{ig} at higher CO₂ levels. After ignition ($\Delta T = 10$ K), the spot of ignition develops into a flame in steady state. For $\Delta T = 100$ K, the slope increases for CO₂ levels above 70%. This can be understood from the reduction in heat release rate due to lesser reactive content in the fuel, leading to a slower flame development.

To further explain the observed behavior, the effect of chemical and thermo physical properties of CO₂ on the IML ignition delay of biogas is assessed by replacing CO₂ in the fuel with the following artificial species as in [75]:

1. CO_{2x}, which is chemically inert CO₂.
2. CO_{2xx}, which is CO_{2x} with the diffusivity of methane.
3. CO_{2xy}, which is CO_{2x} with the heat capacity of methane.

By comparing the ignition behavior of CH₄ - CO_{2x} mixtures with CH₄ - CO₂ mixtures, the influence of reactive properties of CO₂ in biogas is assessed. Similarly with CO_{2xx} and CO_{2xy}, the role of diffusivity and thermal conductivity of CO₂ in the ignition of biogas is quantified. In the following analysis and table 2.2, the synthetic species CO_{2x}, CO_{2xx} & CO_{2xy} replace CO₂ at 30% and 90% in biogas and τ_{ig} is evaluated.

In table 2.2 the first row shows the magnitude of ignition time scales for biogas and the following rows show the change in ignition delays corresponding to each CO₂ substitute in comparison with CO₂. For cases with CO_{2x} and CO_{2xx} the values for τ_{ig} differ only by $\approx 0.1\%$. For CO_{2x} the ignition delays are slightly reduced, indicating a minute inhibitory influence of the reactivity of CO₂ on ignition. These results give a clear proof that the ignition delay is hardly affected by the chemical or transport properties of CO₂. As $Z_{mr} \approx 10^{-3}$, the CO₂ content from fuel can be

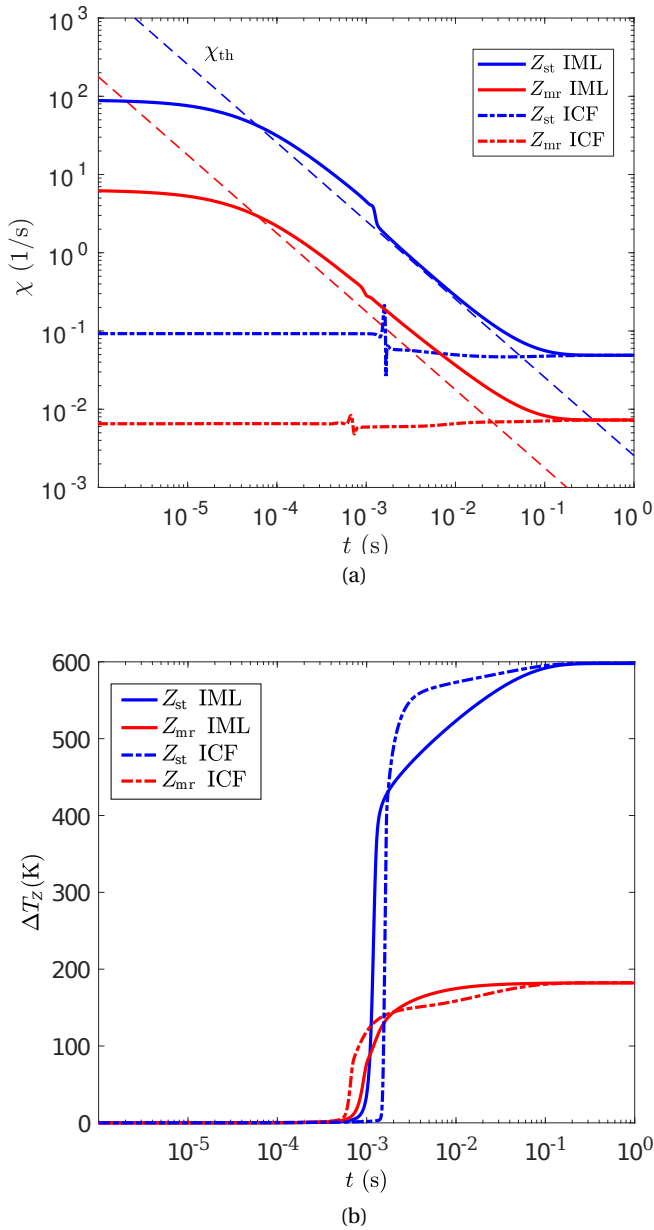


Figure 2.3: Scalar dissipation rates (a) and ΔT_Z (b) at Z_{mr} and Z_{st} against time for IML and ICF. The straight dashed lines in (a) indicates the "ideal" profile of χ_{th} against time.

expected to exert no significant influence on the ignition chemistry. It has to be noted that τ_{ig} increases slightly for 30% and 90% of CO_2/xy in the fuel. This explains

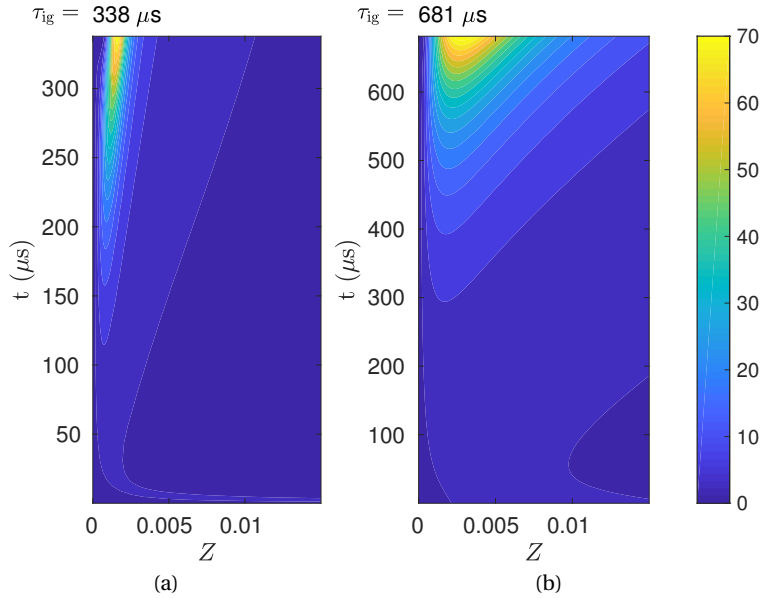


Figure 2.4: Comparison of heat release rate (W/m^3) contours as a function of mixture fraction and time (until ignition) for, a) ICF and b) IML. $Z_{st} = 0.02$

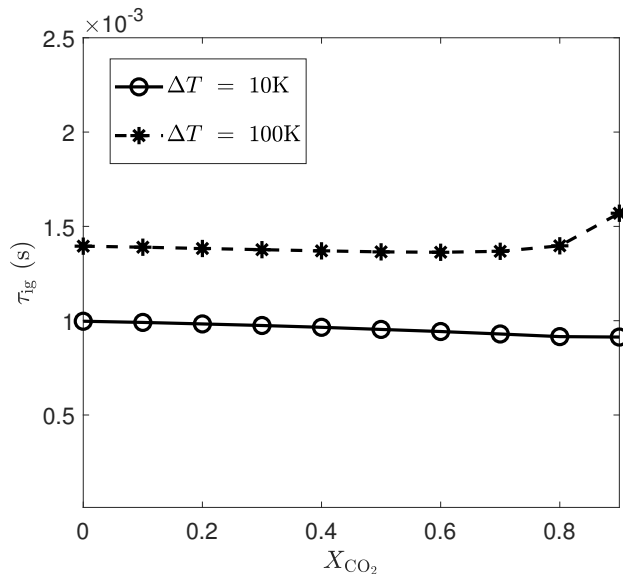


Figure 2.5: Ignition delay against mole fraction of CO_2 in fuel

that the lower τ_{ig} at high CO_2 levels are a result of the lower heat capacity of CO_2 in comparison to CH_4 . Due to the higher C_p of CO_2 , the flame development delay till $\Delta T = 100\text{K}$ is doubled at 90% CO_2 in comparison with 90% CO_2 . In the

Table 2.2: Ignition delay with CO₂ and artificial species in IML, for $T_{\text{ox}} = 1540$ K and $Y_{\text{O}_2, \text{ox}} = 0.08$

Ignition delay	$\Delta T_{\text{max}} = 10$ K		$\Delta T_{\text{max}} = 100$ K	
	30%	90%	30%	90%
$X_{\text{CO}_2, \text{Fuel}}$	30%	90%	30%	90%
CO ₂ (ms)	0.97	0.91	1.38	1.57
CO ₂ x	-0.1%	-1.2%	-0.1%	-3.7%
CO ₂ xx	+0.1%	+0.1%	+0.02%	-3.6%
CO ₂ xy	+0.5%	+11.3%	+1.2%	+39.8%

case of CO₂xx the results are much closer to CO₂x, showing hardly an impact of transport properties.

Role of oxidizer temperature

The influence of oxidizer temperature (T_{ox}) on ignition delay is assessed in a series of IMLs subsequently. For a range of T_{ox} , the oxidizer composition is computed at fixed values of $Y_{\text{O}_2, \text{ox}} = 8\%$, ensuring the same elemental composition. Figure 2.6 shows the variation of τ_{ig} within the given range of temperature. A near linear increase of $\log(\tau_{\text{ig}})$ with respect to the inverse of T_{ox} is observed. It can be noted that the slope of the curve is higher at the lowest temperatures. From shock-tube experiments of methane-oxygen mixtures in argon, an empirical correlation of ignition delay with respect to temperature is given for a range of 1200 K to 2100 K as [85],

$$\tau_1 (s) = 2.5 \times 10^{-15} e^{(26700/T)} [\text{CH}_4]^{0.32} [\text{O}_2]^{-1.02}, \quad (2.10)$$

where the concentrations of CH₄ and O₂ are given in mol/cm³. Equation (2.10) indicates a linear dependency of $\log(\tau_1)$ on T^{-1} . Furthermore, an increase in O₂ concentration shortens the ignition delay and an increase in CH₄ concentration increases the ignition delay. Hence, it can be expected that for a counterflow laminar flame with methane and hot oxidizer, the ignition will occur at a mixture fraction close to zero. A comparison of ignition delay trends (τ_{ig} against T_{ox}) can be made for the IML predictions and the empirical relations such as Eq. (2.10), based on the experimental observations for homogeneous mixtures. A representative correlation based on Eq. (2.10) is given as, $\tau_1 \propto [\text{CH}_4]^{0.32} e^{(26700/T)}$. It is assumed here that the [O₂] at Z_{mr} is constant, that is, $[\text{O}_2]_{\text{mr}} = [\text{O}_2]_{\text{ox}}$. The concentration of CH₄ is considered at the location of Z_{mr} from the unmixed initial condition. τ_1 is plotted in Fig. 2.6 adjacent to the τ_{ig} curve for IML using an appropriate scaling constant.

From the experiments conducted by Zeng et al. [64], a second empirical correlation for τ_{ig} of methane in homogeneous mixtures is given by

$$\tau_2 = 1.31 \times 10^{-3} p^{-0.68} e^{(20199/T)}, \quad (2.11)$$

Homogeneous mixtures of methane-air were considered in this study in a temperature range of 1300 K to 2100 K at a mixture equivalence ratio $\phi = 0.5$. In Eq. (2.11), p represents the pressure in MPa, which is atmospheric pressure in the current study. The slope of this line is given by, $\tau_2 \propto e^{(20199/T)}$, which is lower than that

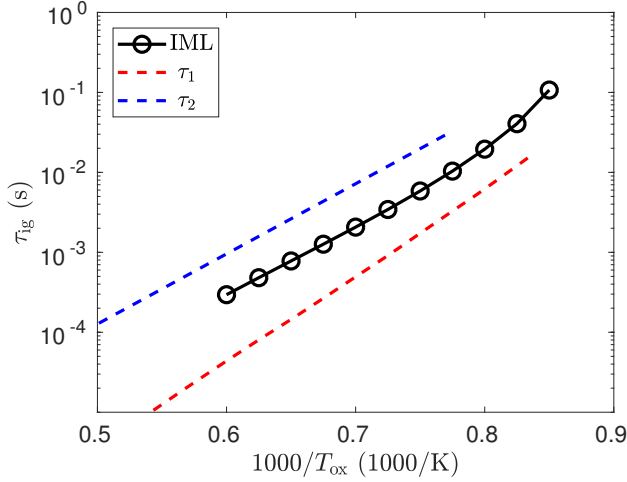


Figure 2.6: Ignition delay against the inverse of temperature, for 8% oxygen in the oxidizer by mass, the dashed curves represent trends based on empirical predictions.

of τ_1 . This trend is plotted in Figure 2.6, positioned above the ignition delay curve of IML. The IML ignition delay curve shows slope close to the experimentally observed value in Eq. (2.11) for most part of the temperature range considered (1300 K - 1650 K). Therefore the activation temperature, T_a for IML is closer that of τ_2 . For $T_{\text{ox}} < 1250$ K ($1000/T_{\text{ox}} > 0.8$) the ignition delays are clearly seen to increase in a non-linear fashion. This region is outside the range of experimental temperatures for τ_2 . Here onwards the trend gets closer to that from Eq. (2.10) till 1200 K ($1000/T = 0.83$). Apart from similarity in trends, the magnitude of ignition delays are larger in the case of IML compared to the homogeneous mixtures considered here, which is caused by diffusive transport of radical species at the onset of ignition.

Figure 2.7 shows Z_{mr} , the location of ΔT_{max} in mixture fraction space at the time of ignition, against the oxidizer temperature. It shows that Z_{mr} remains low within the order of $Z \approx 10^{-3}$ but varies across the range of T_{ox} . At a high oxidizer temperature, τ_{ig} is short and the scalar dissipation rates are large, leading to more diffusive transport, causing higher reactivity at $Z > 10^{-3}$. For example, in Fig. 2.4 it was seen in the case of ICF that the heat release and therefore the major reactions are concentrated over a narrow zone close to the oxidizer side, whereas in the IML, the reaction zone is widened as the reactive species are subjected to a high scalar dissipation rate. The radical species formed close to the high temperature zone are transported in the direction of fuel, widening the heat release zone and shifting the Z_{mr} towards Z_{st} compared with ICF. This shift in Z_{mr} , however, diminishes with lower T_{ox} . With the decrease in T_{ox} , the reaction rates slow down leading to an increase in τ_{ig} . Owing to the reduction in scalar dissipation rates with the ignition delay, the Z_{mr} settles towards a limiting value and becomes comparable to ICF.

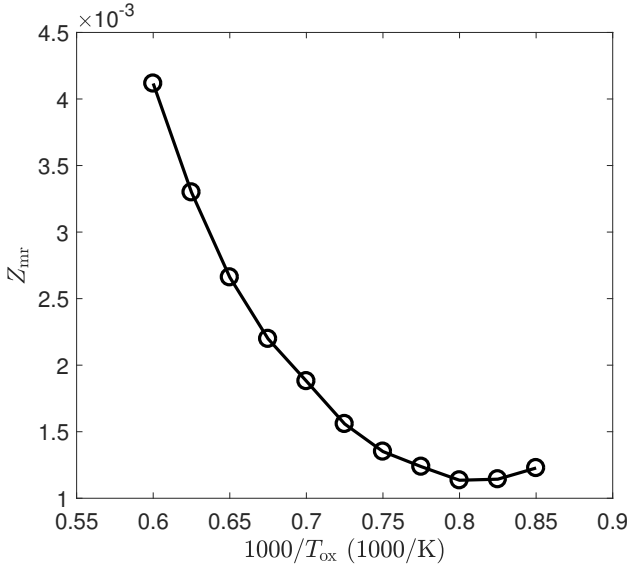


Figure 2.7: Z_{mr} with respect to T_{ox} for $Y_{O_2,ox} = 0.08$

The ignition delay prediction for biogas compositions are shown in Figure 2.8 for $Y_{O_2,ox} = 8\%$ in the range of T_{ox} 1200 - 1540 K. Evidently, for CO_2 levels from 0 till 90% the ignition delay trends nor their magnitudes are hardly affected by the presence of CO_2 . The small change in thermal properties of the fuel is reflected in the small advancement of ignition in the case of biogas with 90% CO_2 . The relative insensitivity of ignition delays to CO_2 levels as observed from Fig. 2.5 holds true for the entire range of oxidizer temperatures considered here.

Role of oxygen concentration in oxidizer

Low levels of oxygen concentration in the oxidizer is a defining characteristic of MILD combustion. Therefore, the dependence of ignition delay with respect to oxygen levels is also investigated here. Figure 2.9 shows the ignition delay trends to $Y_{O_2,ox}$ of 8% and 4%, for X_{CO_2} varying from 0 to 90% at $T_{ox} = 1540$ K. With the oxygen level reduced to half, the ignition delays are seen to be doubled. This is in agreement with the empirical relation (2.10). With respect to the CO_2 level, the reduction in $Y_{O_2,ox}$ does not change the ignition delay behavior as from previous observations. The dependence of ignition delay on $Y_{O_2,ox}$ is investigated for oxidizer temperatures of 1200 K and 1540 K and for oxygen mass fractions ranging from 2% to 16%. The results are presented in Figure 2.10. For both the oxidizer temperatures, the ignition delay curves remain parallel till the oxygen levels fall below 4%. The dashed lines in Figure 2.10 represent trends based on empirical relations. The red line is proportional to $[O_2]^{-1.02}$ (Eq. 2.10) and the magenta line is proportional to $[O_2]^{-0.8}$, which is chosen to match the trend of the curves. It can be seen that for $T_{ox} = 1540$ K, the red curve traces the ignition trend till $Y_{O_2,ox} \approx 0.04$ but shows a faster decline in τ_{ig} with increasing oxygen levels in IML. For $T_{ox} = 1200$ K, the

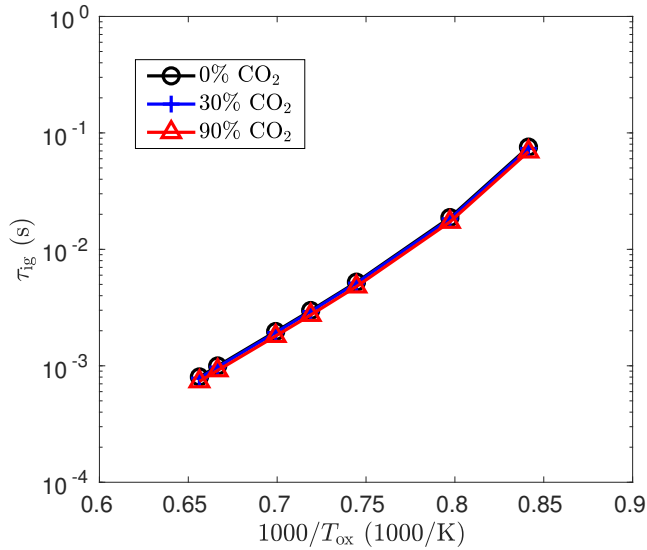


Figure 2.8: Ignition delay against T_{ox} for different levels of CO_2 in fuel (methane) for $Y_{O_2,ox} = 0.08$

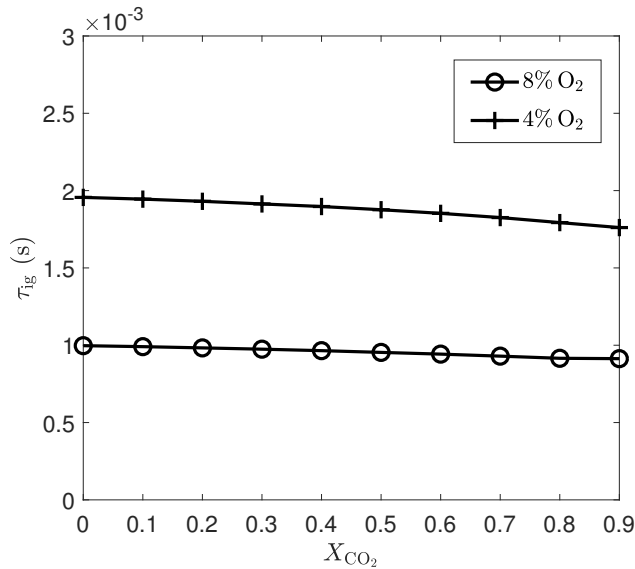


Figure 2.9: Ignition delay against percentage of CO_2 in the fuel for $Y_{O_2,ox} = 0.04$ & 0.08 with $T_{ox} = 1540$ K

ignition delay in this region increases at a higher order of $[O_2]$ than -1.02 . At both temperatures (for oxygen levels from 4% till 16%), the $[O_2]^{0.8}$ curve reproduces the trend in τ_{ig} closely. Hence it can be observed that for IML the ignition delay is less

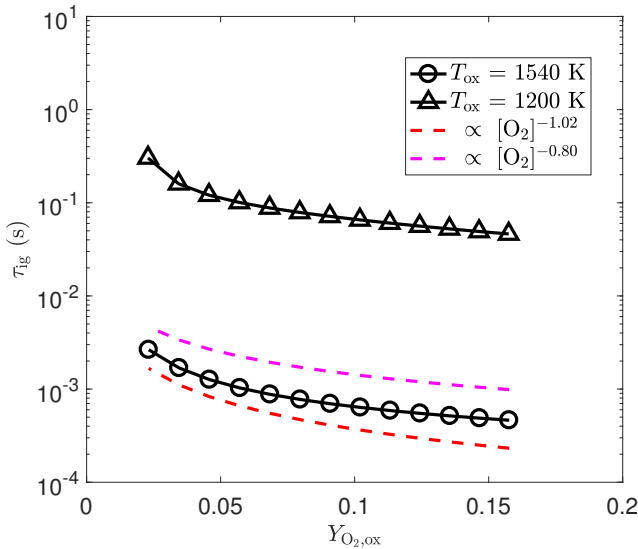


Figure 2.10: Ignition delay against oxygen mass fraction in the oxidizer

sensitive to the oxygen concentration than in homogeneous mixtures and thereby causing a reduction in the order of oxygen concentration to approximately -0.8 .

Influence of trace amounts of higher alkanes

Biogas-like composition considered in the DJHC experiments consists of natural gas (NG) and CO_2 . NG was used as an affordable alternative to methane in the biogas experiments [49]. The presence of trace amounts of higher alkanes in NG such as ethane and propane are known to reduce the ignition delay of methane, wherein a relatively weak carbon-carbon bond can be thermally split yielding loosely bound hydrogen atoms in the chain initiation step [86]. The ignition of methane-ethane blends are studied in homogeneous mixtures by C. Aul et al. [87], which indicated that addition of ethane to methane results in a large, non-linear effect on reactivity and thereby ignition delays. Following [49], the presence of higher alkanes in NG is approximated as 3.7% ethane by volume, with the rest of the composition made of 81.3% of methane, 14.4% of nitrogen and 0.6% CO_2 . Figure 2.11 shows the ignition delay comparison for methane and natural gas as the reactive component of biogas, mixed with various levels of CO_2 . The ignition delay for NG is 10% lower than CH_4 due to the presence of C_2H_6 , which accelerates the ignition. However, the addition of CO_2 does not show a different interaction with NG than with pure methane.

Figure 2.12 illustrates the ignition delays in IMLs for methane and natural gas (NG) over the temperature range 1200-1540 K for $Y_{\text{O}_2,\text{ox}}$ of 8%. With a modest amount of ethane present in the fuel mixture, the ignition is advanced slightly across the range of temperatures.

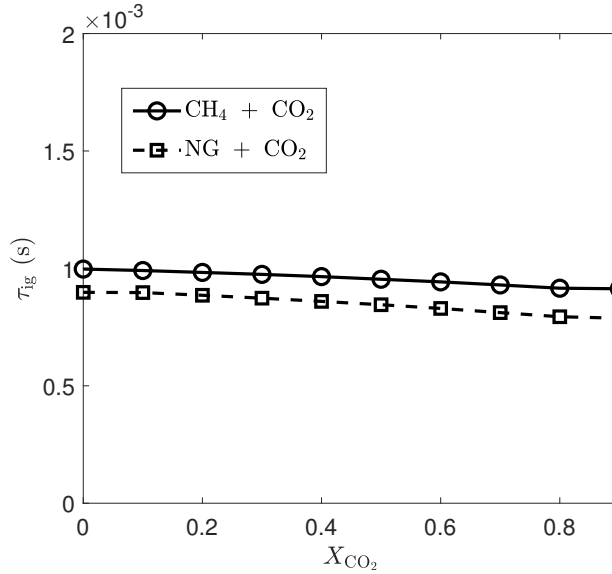


Figure 2.11: Comparison of τ_{ig} for biogas-like compositions using natural gas instead of methane with $T_{ox} = 1540$ K and $Y_{O_2,ox} = 0.08$

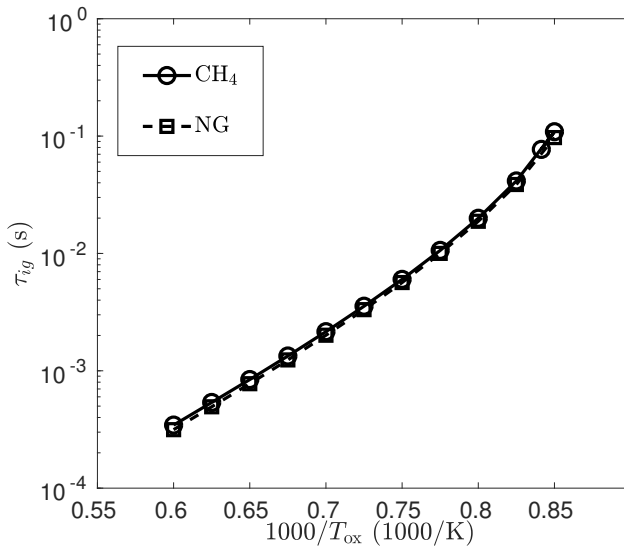


Figure 2.12: Comparison of τ_{ig} against oxidizer temperature for methane and natural gas for $Y_{O_2,ox} = 0.08$

Sensitivity analysis

In this section, the impact of fuel bound CO_2 content on ignition chemistry is examined in IML. Also the influence of oxidizer temperature on the various methane

oxidation pathways is evaluated based on reaction sensitivity analysis. The sensitivity of ignition delay to oxidation chemistry of methane and biogas has been examined in previous studies [64, 87, 88] for homogeneous mixtures at specific equivalence ratios. From these studies the influence of CO₂ on ignition kinetics is seen to act in two main ways. A first effect is related to the enhancement of the reverse rate of reaction,



consuming H radicals which have a positive impact on ignition. The reference to reaction, R99, stands for the corresponding number of the reaction in the GRI 3.0 mechanism. A second mode of influence is related to the increase in third body collision efficiencies. The influence of CO₂ on ignition was found to be the largest for a stoichiometric mixture. In the case of IML these equivalence ratios are not isolated and therefore the influences of chemistry on ignition delay needs to be more precise. Also the impact of CO₂ on ignition or the reasons for the relative absence of its influence (as seen in previous sections) are investigated. To identify the chemical reactions which are critical to the ignition of biogas in IML, a sensitivity analysis is performed. The sensitivity of ignition delay to the reaction chemistry is examined for oxidizer with 8% O₂ and at temperatures of 1200 and 1540 K.

IML ignition delays are computed with 10% increment in individual reaction coefficient for every reaction in GRI Mech 3.0. From the results, a relative sensitivity coefficient σ for each reaction in the mechanism is computed as,

$$\sigma_r = \frac{k_r}{\tau_{\text{ig}}} \frac{\Delta \tau_{\text{ig}}}{\Delta k_r} = \frac{1}{\tau_{\text{ig}}} \frac{\tau_{\text{ig}}(r_k) - \tau_{\text{ig}}}{0.1}, \quad (2.12)$$

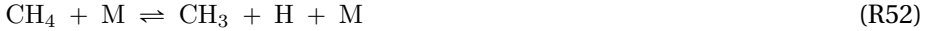
where $\tau_{\text{ig}}(r_k)$ stands for the ignition delay corresponding to a 10% increase in the reaction rate constant k for reaction r_k . A negative value of σ points to enhancement of ignition and a positive σ denotes an inhibitory effect of the reaction. Figure 2.12 shows the most sensitive reactions in IMLs plotted for fuels CH₄ and CH₄ – CO₂(90%) corresponding to (a) $T_{\text{ox}} = 1200$ K and (b) $T_{\text{ox}} = 1540$ K. It can be seen that the ignition delay becomes much more sensitive to reactions at lower temperatures. The reason for this drop in σ at high temperatures is the presence of higher amounts of H, OH and O radicals, which play the main role in chain branching reactions that enhance ignition. Therefore, a 10% change in the most important chain branching reaction in the ignition of alkanes, R38 [21],



results in less than 10% change in the ignition delay. Therefore, the role of chemistry to rise temperature by 10 K is relatively lower than in case of a low temperature mixture. Furthermore, it can be seen that for the range of temperatures considered, R99, a critical reaction that is important in homogeneous mixtures of biogas, has no notable influence on the ignition delay. This could be due to the fact that despite containing 90% CO₂ in the fuel, at Z_{mr} the CO₂ levels are not high enough to cause a reversal in reaction R99.

Considering the third body collision efficiency aspect of CO₂, Fischer and Jiang [71]

found that the thermal decomposition of methane by means of reaction,



becomes crucial for rich homogeneous mixtures in the presence of CO_2 . In the case of IMLs however, this reaction shows very low sensitivity, ($\sigma < 0.3\%$, this reaction is therefore not included in the figures comparing the sensitivity coefficients) as again Z_{mr} is situated in an ultra lean region in mixture fraction space. Hence the presence of CO_2 is seen to be irrelevant on ignition kinetics.

Further, the response of oxidation steps for methane to the oxidizer temperature is addressed. It can be seen from Figure 2.12 that the chain branching reaction R38, which plays the most important role in ignition, promotes ignition at $T_{\text{ox}} = 1540 \text{ K}$ and 1200 K . The instantaneous rates for major reactions inhibiting and promoting ignition are plotted as a function of Z in Figure 2.13 for both fuels under consideration. Although it does not provide direct information on the history of reactions, it gives insight into the reaction rates at the time of ignition indicating the fuels' stage of oxidation. It can be noted that at 1200 K the heat release is of much lower magnitude and takes place at much lower mixture fraction than for 1540 K . As previously discussed in section 3.1.2, this effect is caused by the scalar dissipation decay in IML. Also methane shows ignition closer to the oxidizer than biogas (with 10% methane). The reduced availability of methane shifts the heat release to a region away from the oxidizer.

In the C_1 branch for the oxidation of methane, two reaction paths exist for the conversion of CH_3 into CO_2 [75, 85],

- $\text{CH}_3 \rightarrow \text{CH}_3\text{O} \rightarrow \text{CH}_2\text{O} \rightarrow \text{HCO} \rightarrow \text{CO} \rightarrow \text{CO}_2$
- $\text{CH}_3 \rightarrow \text{CH}_2(\text{s}) \rightarrow \text{CH}_2 \rightarrow \text{HCO} \rightarrow \text{CO} \rightarrow \text{CO}_2$

R97 and R119, which are among the most ignition promoting reactions in Figure 2.12, mark the distinct reaction lines for CH_3 .



Figure 2.13(a-b) shows the instantaneous rates of R97 and R119 at ignition. From the plots, the reaction rate of R119 is higher than R97 at 1200 K for both fuels. The sensitivity coefficients show that ignition is highly promoted by R119 at 1200 K , in comparison to which R97 shows a lower ignition promoting effect. R119 is known to be the dominant oxidation step for methyl radical close to ignition [85, 88], producing the dominant chain branching radical OH and CH_3O , at the same time consuming HO_2 . As for homogeneous mixtures, this reaction is shown to be highly ignition promoting [88]. R119 competes with the chain termination reactions, R87 and R158,



competing for HO_2 and CH_3 respectively. The highest ignition inhibiting effect (largest positive values of σ) for R87 and R158 at 1200 K highlights the significance of reaction R119 in the case of IML as well. Furthermore, the ignition inhibiting reactions mainly show one characteristic, that is the formation of HO_2 , feeding reaction R87 at 1200 K.

The ignition promoting reactions with highest σ indicate dominance of the second reaction line in the C1 branch. At $T_{\text{ox}} = 1540$ K, R97 has a higher reaction rate than R119 and has a higher ignition promoting effect in comparison. Here the inhibitory effect of chemistry on ignition becomes much smaller in general and the inhibitory influence of HO_2 forming reactions are seen to be diminished. Further down the pathway, the reaction R290



shows maximum sensitivity. Furthermore, Figure 2.13(a-b) shows that the peaks of R97 and R290 are aligned at both temperatures to the HRR peak, whereas the peak of R119 is offset to the richer side at high temperature. At high temperatures, shorter τ_{ig} cause ignition to occur under high χ (Figure 2.7), which favors diffusion to the richer side, hence shifting the peaks of reactive species. Here R97 shows lesser influence of χ as compared to R119. This suggests that R97 is a more significant route of oxidation for methyl radical at high temperature and scalar dissipation rate.

The subsequent oxidation of $\text{CH}_2(\text{S})$ results in the formation of formyl radical and its conversion to CO could take place following the reaction pathways R167 and R168 [89],



Figure 2.12(b) shows that R167 promotes ignition whereas R168 has a high inhibitory effect on ignition as it produces the chain terminating radical HO_2 . Figure 2.13(c-d) shows that R168 has a high reaction rate than R158 and R87 which are the most ignition inhibiting reactions at 1200 K. The relative increase in the influence of HCO oxidation at 1540 K suggests that the ignition is more sensitive to the terminal steps of methyl oxidation at high temperatures.

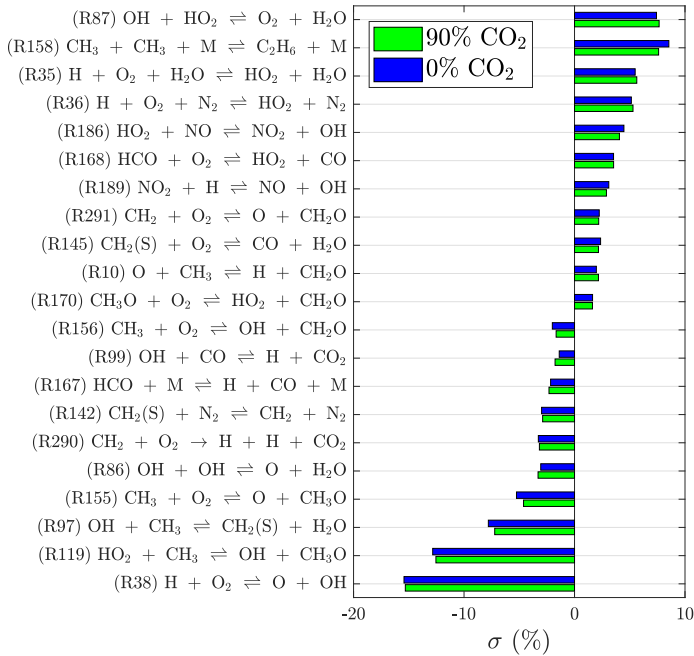
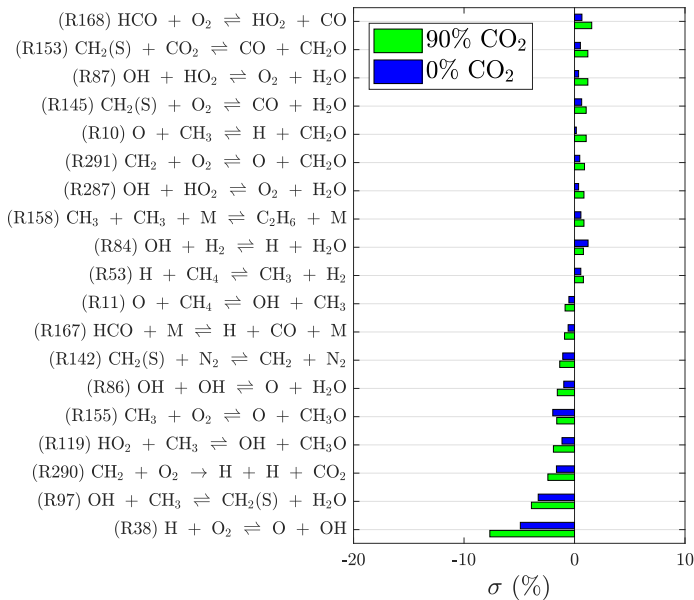
From the observations comparing ignition chemistry at 1200 K and 1540 K in Figure 2.13, it can be suggested that following the main chain branching reaction R38, at 1200 K the ignition is promoted by the methyl oxidation route R119 and inhibited by R87 and R158. R97 promotes ignition better at 1540 K and the inhibitory effect of HO_2 producing reactions on ignition are at bare minimum here. The shift in the most sensitive reaction pathways across temperatures indicate the stage of flame development at which ignition is attained. In the case of IML, for both oxidizer temperatures considered, the influence of CO_2 on ignition sensitivity can be attributed to the heat capacity of CO_2 rather than its chemical depletion of the O/H radical pool which is critical for ignition as seen in homogeneous mixtures. Therefore it is shown here that fuel bound CO_2 is irrelevant to the ignition chemistry. The sensitivity coefficients for methane oxidation steps show that in a non-premixed

environment the reaction pathways change their sensitivities with respect to the oxidizer temperature.

2.4 Conclusion

The ignition of methane and biogas in unsteady reaction-diffusion layers (IML) was investigated. In contrast with previous studies on the ignition of biogas in homogeneous mixtures [71], the current study shows that the addition of CO_2 has little influence on ignition delay in non-premixed mode. The largest influence of CO_2 addition is found in the flame spreading rate, that is, an increment in CO_2 level leads to a slower growth of the flame across the mixture fraction space. The differences between the ignition in a spatial mixing layer and a counterflow setup are also studied. Against ICF, IML shows increased ignition delay due to high initial scalar dissipation rate. It is shown in the results that in a non-premixed MILD environment, the properties of the hot oxidizer impart a far more significant influence on ignition delay than the inert components in biogas. A sensitivity analysis of ignition delay with respect to CO_2 levels in biogas shows weak relative sensitivity with respect to reactions involving any of the fuel components.

The results from the current study are important for modeling turbulent MILD combustion of biogas. This holds especially for of a Jet-in-Hot-Coflow burner where the turbulent mixing of fuel with the hot coflow leads to pockets of ignition, which stabilizes the flame. With respect to MILD combustion in practical applications, further investigation is required to understand the role of product recirculation, interaction of multiple mixing layers, higher dimensional effects and turbulence on the ignition of biogas in non-premixed systems. The influence of turbulence on non-premixed ignition was reviewed by Mastorakos [90]. An increase in the CO_2 content in biogas increases Z_{mr} , and therefore may enhance the effects of turbulence on ignition. The results from the current IML study helps in explaining the experimental findings in DJHC experiments with biogas, that a higher level of CO_2 in the fuel may not affect the ignition delay and thereby the lift-off height of the flame.

(a) $T_{ox} = 1200 \text{ K}$ (b) $T_{ox} = 1540 \text{ K}$ Figure 2.12: Relative sensitivity of τ_{ig} for methane and biogas with 90% CO_2 .

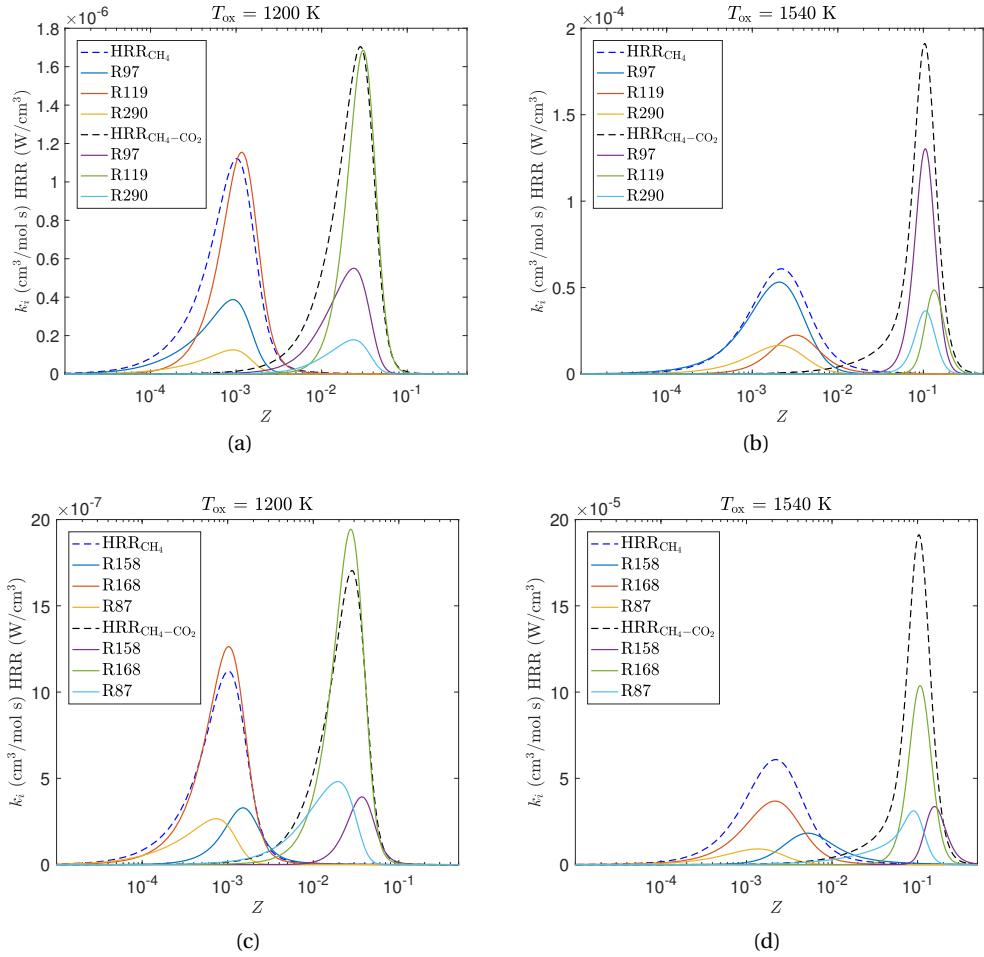


Figure 2.13: Reaction rates of selected (a,b) ignition promoting reactions and (c,d) ignition inhibiting reactions in IML at $t = \tau_{\text{ig}}$, the instantaneous heat release rates are plotted in dashed lines.

2.A Appendix

Table 2.3: Oxidizer boundary conditions. The stoichiometric mixture fraction is given for CH_4 .

Cases	T_{ox} (K)	Y_{O_2}	$Y_{\text{OH}} \times 10^6$	$Y_{\text{H}_2\text{O}} \times 10^2$	$Y_{\text{CO}} \times 10^7$	$Y_{\text{CO}_2} \times 10^7$	Y_{N_2}	$Y_{\text{NO}} \times 10^4$	Z_{st}
1	1600	0.04	53.94	4.14	34.21	5.18	0.87	8.78	0.01
2	1600	0.08	63.87	4.07	22.81	5.09	0.82	12.38	0.02
3	1540	0.04	33.22	4.15	14.82	5.18	0.87	6.69	0.01
4	1540	0.08	39.37	4.07	9.91	5.09	0.82	9.44	0.02
5	1480	0.04	20.43	4.15	6.40	5.18	0.87	5.10	0.01
6	1480	0.08	24.24	4.07	4.29	5.09	0.82	7.19	0.02
7	1428	0.04	12.56	4.15	2.76	5.18	0.87	3.88	0.01
8	1428	0.08	14.91	4.07	1.86	5.09	0.82	5.48	0.02
9	1380	0.04	7.72	4.15	1.19	5.18	0.87	2.95	0.01
10	1380	0.08	9.17	4.07	0.80	5.09	0.82	4.17	0.02
11	1334	0.04	4.74	4.15	0.51	5.18	0.87	2.25	0.01
12	1334	0.08	5.63	4.07	0.35	5.09	0.82	3.17	0.02
13	1290	0.04	2.91	4.15	0.22	5.18	0.87	1.71	0.01
14	1290	0.08	3.46	4.07	0.15	5.09	0.82	2.41	0.02
15	1250	0.04	1.79	4.15	0.09	5.18	0.87	1.30	0.01
16	1250	0.08	2.12	4.07	0.06	5.09	0.82	1.83	0.02
17	1200	0.04	1.10	4.15	0.04	5.18	0.87	0.99	0.01
18	1200	0.08	1.30	4.07	0.03	5.09	0.82	1.40	0.02
19	1176	0.04	0.67	4.15	0.02	5.18	0.87	0.75	0.01
20	1176	0.08	0.80	4.07	0.01	5.09	0.82	1.06	0.02

Chapter 3

FGM modeling of autoigniting non-premixed systems

Abstract

This paper introduces a new method to formulate reaction progress variables for the application of FGM in combustion systems. The method involves a multi-objective optimization to find a reaction progress variable that accurately reproduces complex reactive phenomenon of interest. In our current research, the method is applied to igniting non-premixed flames. The optimized progress variable combinations are evaluated for their accuracy in reproducing detailed chemistry results for the ignition of hydrocarbon fuels. Comparisons are made against conventional progress variable formulations used in literature. The current approach takes into consideration the table resolution and error reduction for the application of FGM in combustion problems. Methods that rely on maximizing the smoothness of the manifold or ensuring monotonic increase in progress variables alone are shown to be insufficient to capture ignition. The possibility of optimizing the progress variable with emphasis on accurately resolving a particular zone or phase of combustion, such as ignition, while maintaining minimum data loss is demonstrated. Through its application in a number of igniting counterflow flames, the effectiveness of the current method is verified. Progress variables optimized using specific flame databases are shown to accurately reproduce the ignition delays even with moderate variations in boundary conditions of the respective flames.

This paper closely follows by "A novel method to automate FGM progress variable with application to igniting combustion systems" Vasavan et al. [91].

3.1 Introduction

The combustion in a non-premixed configuration is a complex process involving ignition of a cold fuel mixture in the presence of an often oxygen lean coflow with a temperature above the ignition temperature. With the coflow being hot and diluted, the oxidizer mixture contains a high amount of product gases and traces of radical species, to which the ignition and thereby flame stabilization is sensitive. For stabilized turbulent jet flames and bluff body stabilized flames, models based on steady flamelets have been successfully used in the past [92–95]. In such cases, the interaction of hydrodynamic strain and chemistry plays a significant role in the stabilization and structure of the flame, where an assumption of locally laminar flamelets being embedded in a turbulent flow field holds well. For computational simulation of MILD combustion, ignition has a crucial role in flame stabilization as found in detailed numerical and experimental studies [50, 96, 97]. Unsteady

flamelet models based on igniting flamelets have been used in LES simulations of lifted JHC flames [56, 98], which capture the flame lift-off heights in the vitiated coflow burner of Cabra et al. [99] and the Delft JHC burner [43]. In methods based on non-premixed flamelets, the mixture fraction Z serves as a primary controlling variable that represents laminar mixing in a two stream problem or equivalence ratio in case of partially premixed flamelets. A reaction progress variable \mathcal{Y} is used to describe combustion progress and is used as the second controlling parameter for tabulating a manifold that is constructed from the laminar unsteady flamelets. It is then assumed that the obtained composition-space trajectories, which can be tabulated as a function of progress variable and parameters representative of the fresh gases' composition, possess a sufficiently high generic character to be applied to turbulent flames. The essential requirement for a progress variable is to have monotonic variation from a non-reactive state of the mixture to its maximum value at the completion or attainment of a steady state of chemical reactions. The reaction progress variable is usually formulated as a linear combination of reactive species, which makes it straight forward to solve a transport equation when applied in a combustion simulation. Various formulations of the progress variable have been employed in literature which are mostly manually selected, comprised of the mass fractions of major product species and significant radical species. A couple of examples for progress variables from literature are,

$$Y_1 = Y_{\text{CO}_2} + Y_{\text{H}_2\text{O}} + Y_{\text{CO}} + Y_{\text{H}_2}, \quad (3.1)$$

used by Ihme & Pitsch [100], Yu & Kurose [101]

$$Y_2 = Y_{\text{CO}_2} + Y_{\text{CO}}, \quad (3.2)$$

used by Fiorina et al. [102]

However, the major product species may exhibit non-monotonic changes in various cases, leading to non-monotonicity of the progress variable. Therefore ad-hoc formulations may not always provide an optimal outcome in application. Developing a generic approach for the formulation of a progress variable for practical applications therefore remains an open-ended problem.

A method for the regularization of progress variable was proposed by Ihme et al. [103] enforcing the constraint of monotonic variation in progress variable to obtain an optimal formulation, which was applied in 1D diffusion flames. However, this approach did not address the efficiency of the progress variable in reproducing phenomena like ignition, which is of paramount significance for FGM applications in igniting non-premixed systems such as MILD JHCs. Niu et al. [104] developed a method for optimization of the progress variable using a constrained gradient minimization approach. For the ignition of homogeneous mixtures and premixed flames the constrained gradient minimization method was shown to yield effective single progress variable formulations.

The current study starts by examining the application of this gradient minimization method to the case of a non-premixed Igniting Mixing Layer (IML). This method relies on solving a constrained linear optimization problem. The formulation of these linear constraint equations are described in the following section. However, this method proves to be increasingly complex to solve as the number

of linear constraint equations of progress variable change increases. As the linear programming problem becomes larger, it may contain many constraints which induce infeasibility. The application of a branch and bound approach [104] to avoid the constraints causing infeasibility is highly time consuming as the number of nodes in a branching tree becomes very large. Furthermore, there may not be a linear combination of reactive species that preserves monotonicity over the entire domain in a non-premixed system. To the authors' knowledge there exists no literature on the optimization of progress variable in a non-premixed system, which preserves the monotonicity of progress variable in the entire thermochemical domain. On the other hand, optimizing for smoothness of the manifold without constraints on the progress variable increment can result in loss of data due to non-monotonicity and may therefore be far from ideal for practical purposes. During its application, an FGM is tabulated onto a grid with predetermined spacing along the individual control variables. This discrete representation introduces an interpolation error, which needs to be minimized for optimal accuracy. In the current study, a new multi-objective optimization (MOOP) method for progress variable formulation is presented, which mitigates a) the loss of thermochemical information and b) the loss of accuracy due to interpolation errors. The MOOP method minimizes data loss by selecting a progress variable that is monotonic in an as large as possible area of the parameter space. However, the monotonicity of the progress variable is not maximized at any cost in this method, because enforcing monotonicity to maximal extent may result in increased interpolation errors in certain areas of the parameter space. Therefore, additional optimization objectives are introduced that minimize interpolation errors in specific areas of interest. These areas are user-defined and need to be well resolved to accurately predict parameters of interest such as ignition delay, flame speed, or pollutant emission. By adding these objectives, an optimized progress variable is obtained which yields accurate predictions of desired quantities, at the cost of losing monotonicity in regions of the parameter space that are less relevant.

The MOOP method can be applied to any kind of flamelet table, whether it is based on homogeneous reactors, premixed flamelets or non-premixed flamelets. However, in the present study it will be applied to non-premixed igniting flames, for which ignition delay is the main parameter of interest. Therefore, next to non-monotonicity, the interpolation error in the source term of the progress variable during the induction phase of ignition is minimized. The effectiveness of the optimized progress variables is evaluated for a number of test cases involving non-premixed ignition of methane and n-dodecane in high temperature environments.

In the next sections the multi-objective optimization approach for the selection of progress variable is explained, followed by results of optimization performed for three cases of igniting non-premixed flames that are well studied in literature.

3.2 Method

Unlike homogeneous mixtures, the ignition in partially premixed systems is affected by convective and diffusive transport across the ignition front. The ignition in a non-premixed system adds further complexity to homogeneous ignition as it

is affected by the convective and diffusive transport of reactants across mixture fractions. Therefore, a one-dimensional IML configuration considered here serves as a generic example that offers a broader problem definition encompassing the computational strategies for applying the new optimization approach in igniting flames.

An IML is the simplest physical representation of an igniting non-premixed combustion system [56, 58, 77, 78]. The IML configuration as considered here has an exponentially decaying scalar dissipation field and thereby incorporates the simultaneous reactive and diffusive processes on ignition. The computational procedure for generating the IML is explained in [58], for a range of boundary conditions as given in Tables 3.1 & 3.2. The degree of mixing in the IML is represented using Bilger's definition of mixture fraction Z , which is given as,

$$Z = \frac{0.5M_H^{-1}[Z_H - Z_{H,2}] + 2M_C^{-1}[Z_C - Z_{C,2}] - M_O^{-1}[Z_O - Z_{O,2}]}{0.5M_H^{-1}[Z_{H,1} - Z_{H,2}] + 2M_C^{-1}[Z_{C,1} - Z_{C,2}] - M_O^{-1}[Z_{O,1} - Z_{O,2}]} \quad (3.3)$$

The general formulation of progress variable \mathcal{Y} is given by a weighted linear combination of the reactive species as,

$$\mathcal{Y} = \sum_{i=1}^{N_{sp}} \alpha_i Y_i \quad (3.4)$$

where Y_i is the mass fraction of the i^{th} species, N_{sp} the total number of species and α_i the corresponding weighting coefficient for the i^{th} species. The values of α_i are constant in space and time. In the IML simulations \mathcal{Y} and Y_i are discrete functions of space and time which are represented as

$$\mathcal{Y} = \mathcal{Y}(t^k, x^j) \quad (3.5)$$

and

$$Y_i = Y_i(t^k, x^j), \quad (3.6)$$

where t^k is the time step, that varies from $k = 1, N_t$, with N_t being the total number of time steps, and x^j is the spatial coordinate that varies from $j = 1, N_x$ where N_x is the total number of spatial points in the IML.

For an optimal definition of progress variable, the values of α_i have to meet the following criteria [103–105] :

1. The progress variable should evolve monotonically along the chemical trajectories, so that the thermochemical coordinates in the flamelets maintain a one-to-one relationship with the progress variable.
2. The gradients in species concentrations with respect to the progress variable should be minimal, which reduces interpolation errors during lookup.

It follows from 1 & 2 that, during the application of FGM, the interpolation and inversion of database control variables should incur minimal errors. However, in

practice the database is constructed along a structured manifold mesh, where the grid resolution in progress variable definition is predetermined.

The IML data that is distributed along spatial coordinates is first remapped onto a grid of normalized mixture fraction Z transforming $Y_i(t^k, x^j) \rightarrow Y_i(t^k, Z^l)$, where $l = 1, N_Z$, with N_Z being the number of mixture fraction grid points. Any point Z^l in the mixture fraction grid is given by,

$$Z^l = \left(\frac{l-1}{N_Z-1} \right)^c \quad (3.7)$$

The grid used in the current study is in the range $[0,1]$ with $N_Z = 300$. Here c is an exponent of constant value that is manually chosen to resolve regions of importance in mixture fraction space. In the current study, a value of $c = 2$ is used to adequately resolve the region of low mixture fraction as the ignition starts at very low values of mixture fraction for cases with a hot oxidizer [58].

First, a gradient minimization algorithm is evaluated using the method developed by Niu et al. [104], which defines an optimum progress variable as the one with the minimum slope of any species against \mathcal{Y} . This method assumes that there is a solution for α_i that yields a monotonic progress variable. However, this is not generally true. In [104] the optimization is posed as a maximization problem by using the inverse of the slope as the objective, which is given by

$$y = \max \left(\left| \frac{\Delta \mathcal{Y}}{\Delta Y_i} \right|^{k,l} \right) : k \in 1, 2, \dots, N_t - 1; l \in 2, 3, \dots, N_Z - 1 \quad (3.8)$$

where,

$$\Delta \mathcal{Y} = \sum_{i=1}^{N_{\text{sp}}} \alpha_i \Delta Y_i. \quad (3.9)$$

and y corresponds to the inverse of the highest value of the slope of any species ($i = 1, 2, \dots, N_{\text{sp}}$) against the local progress variable change anywhere in the domain. Δ stands for the temporal change in the quantity at a constant Z , which is given as,

$$\Delta Y_i = Y_i(t^{k+1}, Z^l) - Y_i(t^k, Z^l) \quad (3.10)$$

A set of linear constraints is imposed at every (t^k, Z^l) to ensure monotonic increment in progress variable, as well as to limit the local maximum slope lower than the global maximum $y_i^{k,l}$:

$$\frac{\sum_{i=1}^{N_{\text{sp}}} \alpha_i \Delta Y_i}{|\Delta Y_i|_{\text{max}}} - y > 0 \quad (3.11)$$

where

$$|\Delta Y_i|_{\text{max}} = \max \{ |\Delta Y_1|, |\Delta Y_2|, \dots, |\Delta Y_{\text{sp}}| \}. \quad (3.12)$$

The total number of constraint equations amounts to $(N_Z - 2) \times (N_t - 1)$ where

N_Z is the total number of grid points in Z and N_t the total number of time steps. The boundaries of mixture fraction domain are omitted as there are no changes in species mass fractions at these locations.

Using the MATLAB linear programming toolbox, the system of linear constraint equations were solved to obtain the values of α_i for maximizing the variable y . The upper and lower bounds of α_i were set to $\pm 10^5$. Increasing this limit did not improve the optimal solution. However, for the IML case under consideration this approach did not yield a feasible solution for α_i , i.e. a progress variable that is monotonically increasing at all points in mixture fraction space was not found. Hence for non-premixed flamelets, the existence of a linear combination of species that satisfies the monotonicity criteria needs to be challenged.

A second optimization approach developed by Ihme et al. [103] makes use of a penalty term for non-monotonic points, which is integrated over the set of flamelets to obtain a cost function. The values of α_i are optimized for a minimum value of the cost function, i.e. for the lowest occurrence of non-monotonicity. The advantage of this method is that it does not depend on the assumption of existence of an α_i vector that ensures monotonic evolution of the progress variable everywhere in the domain, but obtains a definition for the progress variable that is monotonic to the maximum extent. However, this approach did not specifically take into consideration the accurate prediction of ignition delays in non-premixed systems and was also not verified for such test cases yet.

3.2.1 New optimization approach

Based on observations from both methods discussed above, the current optimization approach aims to maximize the monotonicity of progress variable, as well as to minimize the inaccuracy in predicting the ignition delay when FGM is applied in combustion systems. Considering the maximum monotonicity of progress variable as an objective for optimization, it will be possible to determine whether the progress variable is monotonic in important regions in the $Z - \mathcal{Y}$ space such as the region of ignition or any other important region depending on the critical physical phenomena to be captured by the database. To estimate the monotonicity, the species mass fractions have to be mapped on a normalized scale of time that evenly resolves fast and slow thermochemical processes. The normalization of time is readily available from the index of the output time step, which corresponds to every 10 computational time steps of the detailed chemistry simulations. The use of variable time stepping ensures an adequate resolution of fast and slow timescales. Therefore, at every output time step and for every point in Z , the monotonicity of progress variable is evaluated as

$$\Delta \mathcal{Y}^{k,l} = \sum_{i=1}^{N_{sp}} \alpha_i Y_i(t^{k+1}, Z^l) - \sum_{i=1}^{N_{sp}} \alpha_i Y_i(t^k, Z^l) > \varepsilon \geq 0 \quad (3.13)$$

where ε is a threshold value, to omit points with nearly no change in \mathcal{Y} from being counted as non-monotonic, which is given by

$$\varepsilon = (\mathcal{Y}^{N_t,l} - \mathcal{Y}^{0,l}) \times 10^{-10} \quad (3.14)$$

The first objective for optimization accounting for the monotonicity of the progress variable is written as

$$\epsilon(1) = \frac{1}{(N_t - 1)(N_Z - 2)} \left[(N_t - 1)(N_Z - 2) - \sum_{k=1}^{N_t-1} \sum_{l=2}^{N_Z-1} \Omega^{k,l} \right] \quad (3.15)$$

where

$$\Omega^{k,l} = \begin{cases} 0, & \text{if } \Delta \mathcal{Y}^{k,l} < \epsilon \\ 1, & \text{if } \Delta \mathcal{Y}^{k,l} \geq \epsilon \end{cases} \quad (3.16)$$

On tabulating the flamelet data as FGM lookup table, the temporal reaction trajectories are remapped along the progress variable for every mixture fraction coordinate. However, the a-posteriori reconstruction of time dependent flamelets using FGM, depends on the time integral of the source term of progress variable $\dot{\omega}_\mathcal{Y}$, along with the transport terms in the progress variable transport equation. For example in a purely reactive-diffusive IML, with the assumption of $Le_i = 1$ for every species, the transport equation for \mathcal{Y} is given by

$$\frac{\partial \mathcal{Y}}{\partial t} = \chi \frac{\partial^2 \mathcal{Y}}{\partial Z^2} + \dot{\omega}_\mathcal{Y} \quad (3.17)$$

where χ is the scalar dissipation rate. It is clear from 3.17 that the accurate reproduction of the time integral of $\dot{\omega}_\mathcal{Y}$ from detailed chemistry simulation is critical for an accurate reproduction of ignition delay in a-posteriori simulation of IML using FGM.

For convenience of representation, the time integral of $\dot{\omega}_\mathcal{Y}$ till ignition can be denoted as the change \mathcal{Y} from unburnt state \mathcal{Y}_u till ignition \mathcal{Y}_{ig} although it is not exact due to the transport terms in the scalar conservation equation. This quantity is written as $\Delta \mathcal{Y}_{\text{ig}}$ from here on, which is given as

$$\int_0^{\tau_{\text{ig}}} \dot{\omega}_\mathcal{Y} dt = \mathcal{Y}_{\text{ig}} - \mathcal{Y}_u = \Delta \mathcal{Y}_{\text{ig}} \quad (3.18)$$

where τ_{ig} is the ignition delay.

In the current study, the progress variable grid $\mathcal{Y}^{m,l}$ is defined in the range $[\mathcal{Y}^{1,l}, \mathcal{Y}^{N_\mathcal{Y},l}]$, with the total number of grid points $N_\mathcal{Y} = 300$, and a grid distribution based on an exponent value $c = 2$ in order to adequately resolve the region with low values of \mathcal{Y} , where the thermochemical events leading to ignition take place. The flamelet data will be interpolated along the \mathcal{Y} grid transforming $Y(t^k, Z^l) \rightarrow Y(\mathcal{Y}^m, Z^l)$ and $\omega_\mathcal{Y}(t^k, Z^l) \rightarrow \omega_\mathcal{Y}(\mathcal{Y}^m, Z^l)$, where $m = 1, N_\mathcal{Y}$.

As the flamelet data is interpolated along a predetermined \mathcal{Y} grid, the time integral of $\dot{\omega}_\mathcal{Y}$ before and after interpolation along \mathcal{Y} has to be the same to yield same τ_{ig} . In practice this is not the case. Figure 3.1 shows an example of the linear interpolation errors of $\omega_\mathcal{Y}$ for an FGM table. The dashed line shows the actual value of progress variable source term $\omega_\mathcal{Y}$ for progress variable \mathcal{Y}_1 , normalized with the initial value of ω_1 . The circles indicate the interpolated values of $\dot{\omega}_\mathcal{Y}$ on a predetermined \mathcal{Y} grid in the FGM table. The solid line corresponds to the values of the same normalized $\dot{\omega}_\mathcal{Y}$, but estimated by a linear look-up procedure based on the

interpolated points. Note that the solid line appears to be curved because time is presented in log scale along the x-axis. The difference between the area under the curve for solid and dashed lines results in an overestimation of reaction progress which leads to a shorter ignition delay during application of this FGM database.

Therefore, a second objective for optimization is devised to minimize the error while the progress variable is interpolated on a \mathcal{Y} grid of a given resolution. The loss of accuracy can be assessed by comparing $\Delta\mathcal{Y}_{ig}$ with $\Delta_g\mathcal{Y}_{ig}$ which is the time integral of $\omega_{\mathcal{Y}}$ over the linear lookup values on the \mathcal{Y} grid.

From the flamelet data $\Delta\mathcal{Y}_{ig}$ is computed using the trapezoidal rule, i.e.

$$\Delta\mathcal{Y}_{ig} = \sum_{k=1}^{N_{tig}-1} \frac{\dot{\omega}_{\mathcal{Y}}^{k,l} + \dot{\omega}_{\mathcal{Y}}^{k+1,l}}{2} \Delta t^k, \quad (3.19)$$

where N_{tig} is the time step index for the ignited flamelet. The progress variable source term, $\omega_{\mathcal{Y}}$ is evaluated at every time step as

$$\dot{\omega}_{\mathcal{Y}}^{k,l} = \sum_{m=1}^{N_{sp}} \alpha_i \dot{\omega}_i^{k,l} \quad (3.20)$$

Similarly, $\Delta_g\mathcal{Y}_{ig}$ is evaluated as

$$\Delta_g\mathcal{Y}_{ig} = \sum_{m=1}^{N_{\mathcal{Y}ig}-1} \frac{\dot{\omega}_{\mathcal{Y}}^{m,l} + \dot{\omega}_{\mathcal{Y}}^{m+1,l}}{2} \Delta t^m, \quad (3.21)$$

where $N_{\mathcal{Y}ig}$ is the nearest progress variable grid point, and Δt^m the interpolated time step. Considering the nearest \mathcal{Y} grid point to ignition introduces an error, $t^{N_{\mathcal{Y}ig},l}$ need not be the same as $t^{N_{tig},l}$. With an adequately refined \mathcal{Y} grid at the region of ignition, this error was found to be negligible when compared with total error in estimating the area under the curve. The relative error δ in estimating $\Delta\mathcal{Y}_{ig}$ is given as

$$\delta = \frac{\Delta\mathcal{Y}_{ig} - \Delta_g\mathcal{Y}_{ig}}{\Delta\mathcal{Y}_{ig}} \quad (3.22)$$

Thus the second objective for optimization is to minimize the relative error in δ on the interpolation of \mathcal{Y} for all values of mixture fraction, which is given by

$$\epsilon(2) = \sum_{l=N_{Z1}}^{N_{Z2}} \delta_l \quad (3.23)$$

where N_{Z1} and N_{Z2} are Z grid indices defining a mixture fraction interval of interest. For the cases considered here, N_{Z1} and N_{Z2} correspond to $Z = 0$ and $Z = 2Z_{st}$ respectively, as ignition of hydrocarbon fuels in hot oxidizer is barely dependent on chemistry at the fuel side of mixture fraction space. Equation 3.23 is further

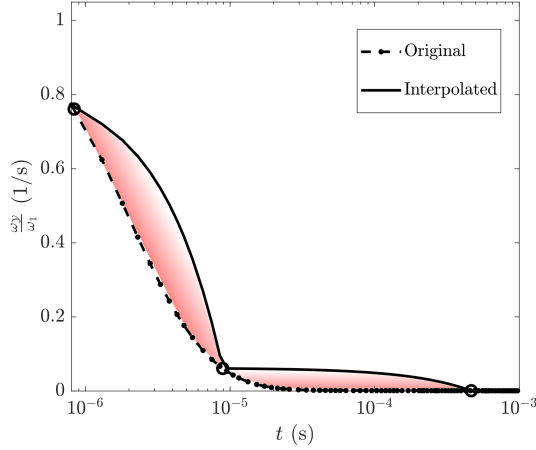


Figure 3.1: An example of interpolation error in ω_Y along the stoichiometric mixture fraction for an FGM database for an IML simulation. The dashed line corresponds to the actual value of progress variable source term $\dot{\omega}_Y$, while the solid line represents the estimated value of the variable by a rectilinear look up method.

rewritten as

$$\epsilon(2) = \frac{\sum_{l=N_{Z1}}^{N_{Z2}} \left(\sum_{k=1}^{N_{tig}-1} \frac{\dot{\omega}_Y^{k,l} + \dot{\omega}_Y^{k+1,l}}{2} \Delta t^k - \sum_{m=1}^{N_{Yig}-1} \frac{\dot{\omega}_Y^{m,l} + \dot{\omega}_Y^{m+1,l}}{2} \Delta t^m \right)}{\sum_{k=1}^{N_{tig}-1} \frac{\dot{\omega}_Y^{k,l} + \dot{\omega}_Y^{k+1,l}}{2} \Delta t^k} \quad (3.24)$$

The multi objective optimization is performed using the Genetic Algorithm (GA) toolbox in MATLAB. The solutions are plotted on a Pareto front, and the healthiest α vector is chosen as the one with maximum monotonicity over the domain. The upper and lower bounds for α_i are limited to $\pm 10^5$. The objective function tolerance is set to be 10^{-3} , over a maximum number of generations $N_{sp} \times 200$. The optimization terminates when the average relative change in the spread of Pareto solutions is less than 10^{-3} . The solution procedure can be made faster by reducing the dimension of the problem space. Species involving nitrogen and argon are omitted from the current optimization procedure and their weights are assumed to be zero as they are inactive in the combustion and inclusion of them did not vary the current results to any significance. Three different igniting non-premixed flames are studied, namely,

1. The vitiated coflow flame of Cabra et al. [40]
2. The Delft Jet in Hot Coflow flame by Oldenhof et al. [42]
3. ECN Spray-A using n-dodecane as fuel [106].

The computational set up used for generating unsteady 1D flames is summarized in Table 3.1. Table 3.2 summarizes the boundary conditions of the three cases. The computations are performed using the one-dimensional flame code CHEM1D [81].

Table 3.1: Summary of computational set up

Parameter	Values
Spatial domain	[-1 : 1] cm
Number of grid points	500 (with adaptive grid refinement)
Time step	Variable time stepping [10^{-8} : 10^{-4}] s
Ambient pressure	1 bar for cases 1&2, 6 bar for case 3.
Reaction mechanism	GRI-Mech [72] for cases 1&2, Yao mechanism [107] for case 3.
Transport model	Unity Lewis number based

Table 3.2: Boundary conditions for 1D simulations of Cabra, DJHC and ECN Spray - A experiments

Parameter	Cabra		DJHC - I				ECN Spray - A	
	Fuel	Oxidizer	Fuel	Ox 1	Ox 2	Ox 3	Fuel	Oxidizer
Temperature	320 K	1350 K	450 K	1380 K	1185 K	1525 K	320 K	900 K
$X_{H_2} \times 10^{-7}$	-	1.1	-	1.1	0.047	15	-	-
$X_H \times 10^{-9}$	-	96	-	1.3	0.011	29	-	-
$X_O \times 10^{-7}$	-	180	-	2.0	0.052	12	-	-
X_{O_2}	0.15	0.12	-	0.075	0.070	0.048	-	0.15
$X_{OH} \times 10^{-5}$	-	20	-	1.9	0.22	7.4	-	-
X_{H_2O}	-	0.15	-	0.089	0.12	0.12	-	0.036
$X_{HO_2} \times 10^{-8}$	-	450	-	3.4	0.58	8.5	-	-
X_{N_2}	0.52	0.73	0.15	0.79	0.74	0.76	-	0.752
X_{CO_2}	-	-	-	0.045	0.064	0.063	-	0.062
X_{CH_4}	0.33	0.0003	0.85	-	-	-	-	-
$X_{nC_{12}H_{26}}$	-	-	-	-	-	-	1.00	-

3.3 Results and Discussion

This section consists of comparisons of detailed chemistry and FGM based igniting non-premixed flames of the three aforementioned test cases. In section 3.1 a detailed analysis of optimized progress variables is made for the Cabra flame. Subsequently the main results are discussed for cases 2 and 3 in sections 3.2 and 3.3, respectively.

3.3.1 Application in Cabra vitiated coflow flame

The progress variable optimization results are presented for a 1D IML of the Cabra vitiated coflow system, at a strain rate of 10/s. The evolution of the temperature profile in this IML is shown in Figure 3.2. The IML has an unsteady gradient in scalar dissipation rate that decays from the initial high value towards a steady state at strain rate of 10/s as shown here.

Considering two widely used progress variable formulations, \mathcal{Y}_1 and \mathcal{Y}_2 see Eq. 3.1 and Eq. 3.2 for the tabulation of the thermochemical information in the IML, the

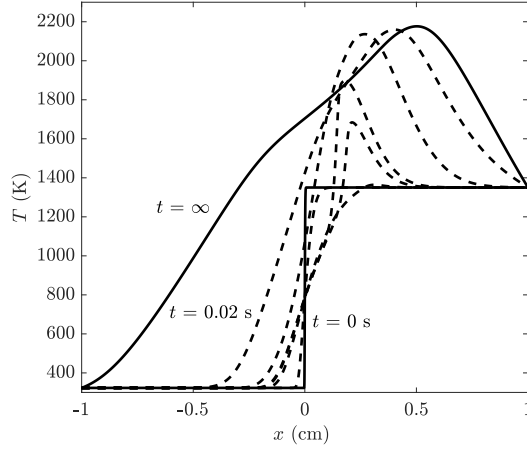


Figure 3.2: The evolution of temperature profile in an IML of the Cabra vitiated coflow system.

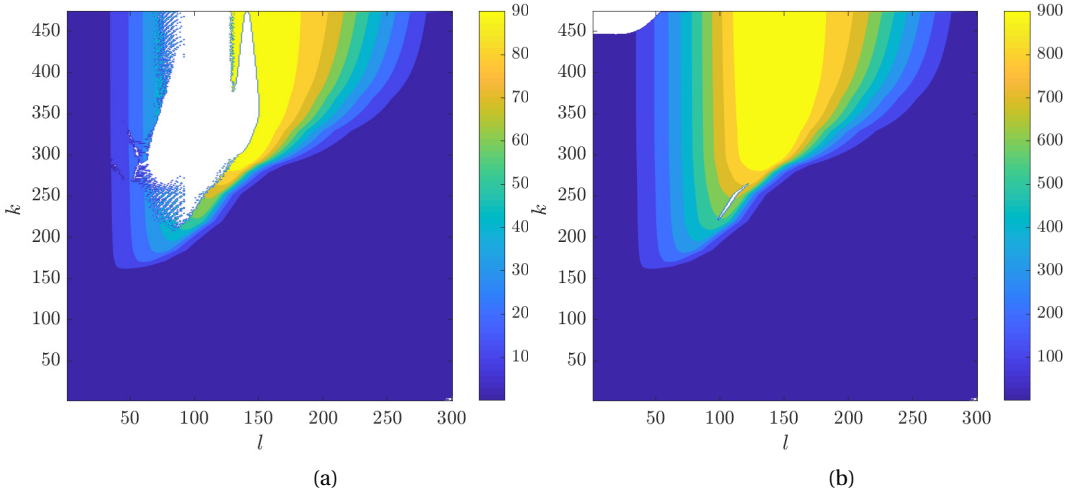


Figure 3.3: Contour plots of temperature rise, $\Delta T = (T^{k,l} - T^{1,l})$ along each point in Z space, also showing the monotonicity of two conventional ad-hoc progress variable definitions (a) \mathcal{Y}_2 , and (b) \mathcal{Y}_1 . The blanked areas indicate regions where the progress variable change is non-monotonic.

loss of data is visualized. Figure 3.3 shows the contour plots of temperature rise ΔT with respect to initial temperature evaluated at constant Z over the computational time $[0, 0.02]$ s for (a) \mathcal{Y}_2 and (b) \mathcal{Y}_1 . Here ΔT is given by

$$\Delta T = (T^{k,l} - T^{1,l}). \quad (3.25)$$

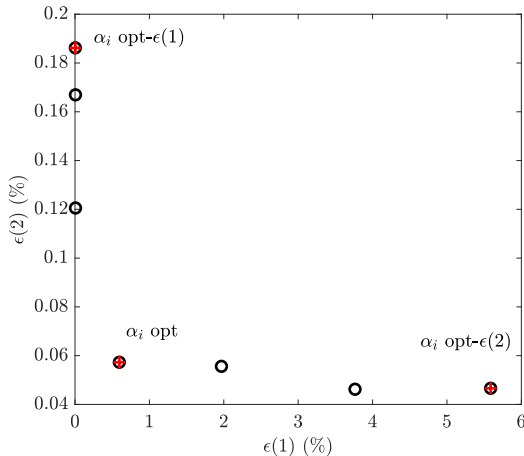


Figure 3.4: Pareto front of solutions for α_i obtained from the multiobjective optimization for progress variable weights in case 1. The plot shows the fitness of solutions with respect to either of the objectives $\epsilon(1)$ and $\epsilon(2)$.

The blanked regions in the plots indicate the loss of thermochemical information due to non-monotonicity in the progress variables while applying these conventional progress variable definitions. \mathcal{Y}_2 shows a greater loss of data when compared with \mathcal{Y}_1 . This implies that except for the representation of the peak CO_2 and CO , \mathcal{Y}_2 is a poor choice to represent the reaction progress for the case under consideration when compared against \mathcal{Y}_1 . Both \mathcal{Y}_1 and \mathcal{Y}_2 show monotonic behavior in regions with $\Delta T \lesssim 500$ K. Therefore, they must be able to reproduce the ignition delay although the accuracy of this will depend upon the estimation of the values of $\omega_{\mathcal{Y}}$.

Figure 3.4 shows the set of solutions of α_i following the multiobjective optimization method. The optimization is terminated when the spread of Pareto solutions is less than the objective function tolerance, i.e. the final seven pareto solutions have a lower spread than an objective tolerance of 10^{-3} . The best solution according to $\epsilon(1)$ is marked on the plot as “ α_i opt- $\epsilon(1)$ ”, for $\epsilon(2)$ it is “ α_i opt- $\epsilon(2)$ ” and for the knee point, “ α_i opt” respectively. The first objective $\epsilon(1)$ is minimized to zero at the left extremity of the Pareto front, indicating a possible progress variable definition that is monotonous everywhere in the domain for the IML under investigation. A minimum non-zero interpolation error is shown to remain even at the cost of 5.5% loss of data. The minimum interpolation error of approximately 0.05% might be limited by the \mathcal{Y} grid resolution considered here. A solution for α_i from the knee point of the Pareto front is chosen as the optimum, as going to any other point can result in decreasing either of the objectives. The progress variable computed based on the knee point values of α_i will be referred to as \mathcal{Y}_{opt} from here onwards. The values for the three sets of α_i are given in Appendix 1.

Figure 3.5 shows the contours of source term for \mathcal{Y}_{opt} in (a) the $Z - \mathcal{Y}$ plane and (b) ΔT contours, with blanked areas to represent the regions of non-monotonic variation in \mathcal{Y} . The $\omega_{\mathcal{Y}}$ contours appear smooth. Although there is a non-monotonic

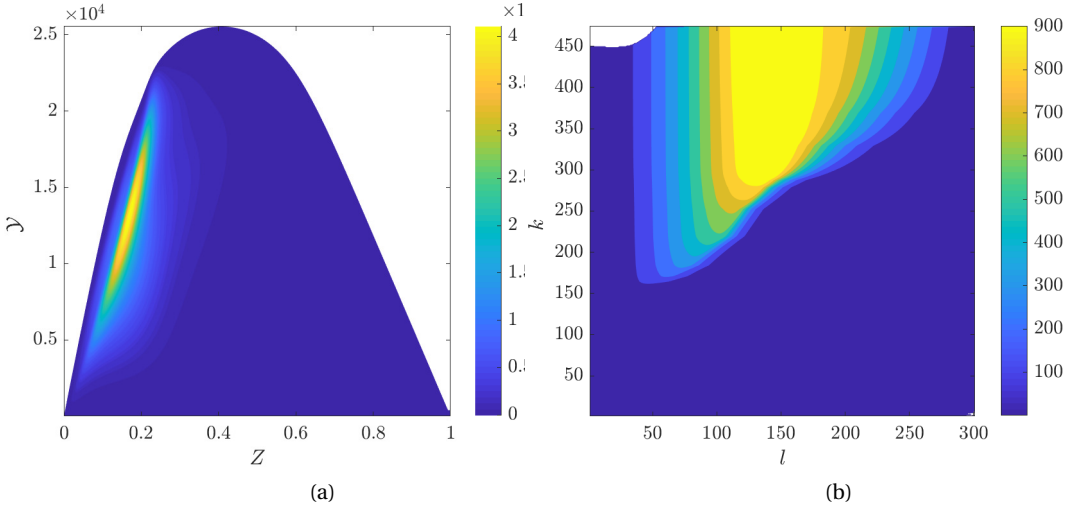


Figure 3.5: Contour plots of (a) source term of the optimized progress variable and (b) the corresponding ΔT .

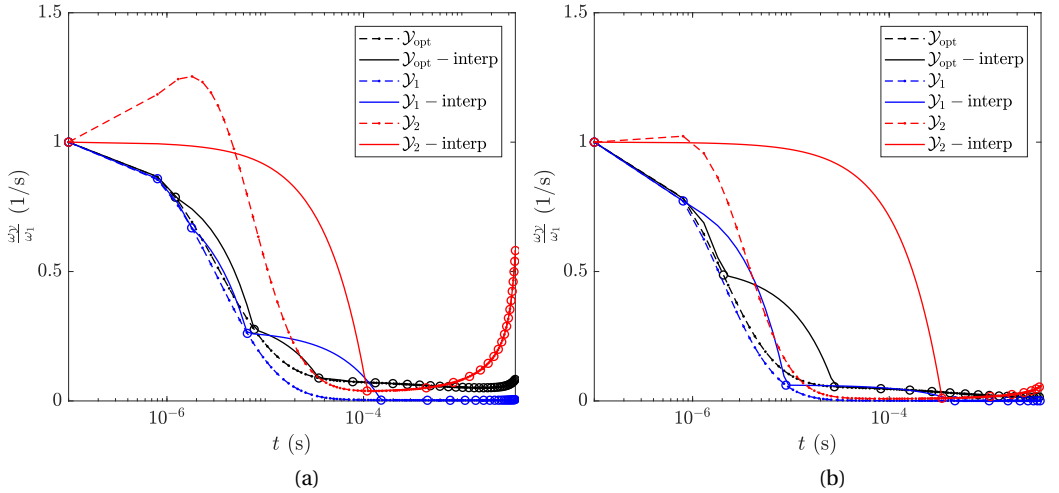


Figure 3.6: Progress variable source ω_γ/ω_1 as a function of time t for (a) $Z = 0.5Z_{st}$ and (b) $Z = Z_{st}$ for $t = [0, \tau_{ig}]$. Conventional progress variable combinations \mathcal{Y}_1 and \mathcal{Y}_2 are compared against an optimal progress variable \mathcal{Y}_{opt} .

region present in the top left corner of the plot, it is located away from the region of ignition as expected from the optimization routine.

Figure 3.6 shows ω_γ/ω_1 curves versus t for \mathcal{Y}_1 , \mathcal{Y}_2 and \mathcal{Y}_{opt} for two points in mixture fraction space, $0.5Z_{st}$ and Z_{st} . The dashed lines represent the original flamelet

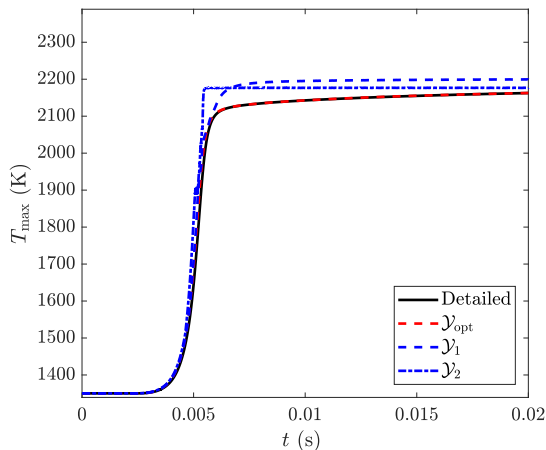


Figure 3.7: Comparison of ignition delay predictions for conventional and optimized progress variable combinations.

points and the circles show the values using interpolation to the \mathcal{Y} grid, where $\omega_1 = \omega_{\mathcal{Y}}(t = 0)$ to normalize the plots. The conventional progress variables require a higher resolution of the \mathcal{Y} grid to represent the strong curvature of $\omega_{\mathcal{Y}}$. Also it has to be noticed that fewer points from the detailed chemistry data are captured with \mathcal{Y}_1 and \mathcal{Y}_2 , with ≈ 5 interpolated points within the time of ignition whereas \mathcal{Y}_{opt} shows a higher number of grid points within the same duration. A smaller number of grid points in the case of conventional progress variables within the same time span indicates a lower growth in the progress variable, yielding a lower resolution of the pre-ignition regime compared to \mathcal{Y}_{opt} . The interpolated curve shows a large difference from the flamelet data in case of \mathcal{Y}_1 and \mathcal{Y}_2 , which may lead to inaccurate ignition delay predictions.

Figure 3.7 shows a comparison of maximum temperature T_{max} against time for simulation of an IML using detailed chemistry and FGM. The progress variables \mathcal{Y}_1 and \mathcal{Y}_2 are considered here along with \mathcal{Y}_{opt} obtained for this case. From the comparisons, \mathcal{Y}_{opt} reproduces the T_{max} curves to the best accuracy out of the three. The difference in ignition delay prediction for the three cases is negligible although it was shown that the formulation of \mathcal{Y} has an influence on the interpolation error during the estimation of $\omega_{\mathcal{Y}}$.

In Fig. 3.7 for $t > 0.007$ s, \mathcal{Y}_2 shows a flat profile due to non-monotonicity in progress variable. \mathcal{Y}_1 predicts the highest temperature and deviates from the detailed chemistry result, indicating that the non-monotonicity here occurs simultaneously with the peak in temperature. The optimized progress variable shows a perfect reproduction of T_{max} from the detailed chemistry result. Although \mathcal{Y}_1 and \mathcal{Y}_2 predict the ignition delay with a good accuracy, compared to \mathcal{Y}_{opt} they start to deviate from the detailed chemistry result after ignition. Further, the peak values of tabulated species are compared for the progress variable formulations under consideration.

Figure 3.8 shows the evolution of peak values of (a) CO_2 , a major product species

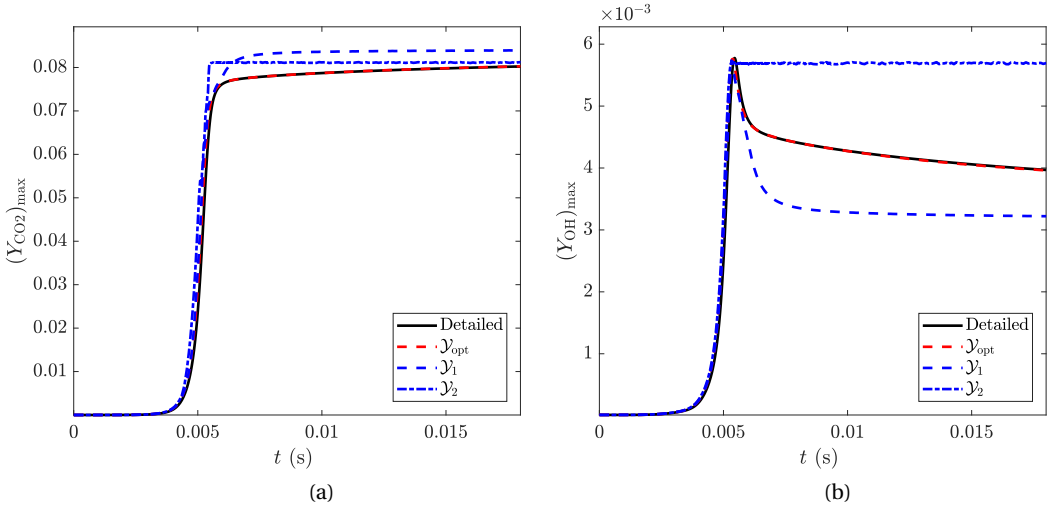


Figure 3.8: Results of IML simulations using detailed chemistry and FGM with different \mathcal{Y} definitions. The maximum mass fractions of (a) CO₂ and (b) OH are plotted against time.

and (b) OH, a radical species critical to ignition, for IML. The trends in peak CO₂ are similar to that of peak temperature in Figure 3.7. Large deviations are shown in the final value of OH, clearly indicating the points where the non-monotonicity sets in. Thus in cases with \mathcal{Y}_1 and \mathcal{Y}_2 the final values of peak OH are seen to deviate from the actual value, while \mathcal{Y}_{opt} reproduces the evolution of peak OH mass fraction accurately.

Figure 3.9 shows the comparison of best progress variable selections from the two optimization objectives considered. Here $\mathcal{Y}_{\text{opt}-\epsilon(1)}$ corresponds to the least value of the objective $\epsilon(1)$ on the Pareto front of optimized solutions and $\mathcal{Y}_{\text{opt}-\epsilon(2)}$ corresponds to the least value of $\epsilon(2)$. The three progress variables predict the ignition accurately, with $\mathcal{Y}_{\text{opt}-\epsilon(2)}$ showing the effect of over-optimizing $\epsilon(2)$ at the cost of monotonicity after ignition. Therefore the α_i solutions on the left branch of the Pareto front, which are optimized increasingly for $\epsilon(1)$, give a better overall results in the current analysis.

To study the effect of scalar dissipation rate profile on ignition delay, the Cabra flame is simulated as an Igniting Counterflow Flame (ICF) [79] with the same boundary conditions as IML, using detailed chemistry and FGM. ICF has a different initial profile and evolution of scalar dissipation rate than IML. In contrast to IML, the reactive process in ICF starts from a steady non-reacting counterflow solution with an applied strain rate, where the time dependent changes in scalar dissipation rate are not considered. Thereby the comparison of IML and ICF simulations shows the influence of a decaying scalar dissipation rate on the accuracy of ignition delay prediction while using an optimized progress variable. Figure 3.10(a) shows the evolution of spatial profile of temperature in an ICF and Figure 3.10(b) shows the corresponding ignition curves with respect to T_{max} . In contrast to IML, the differ-

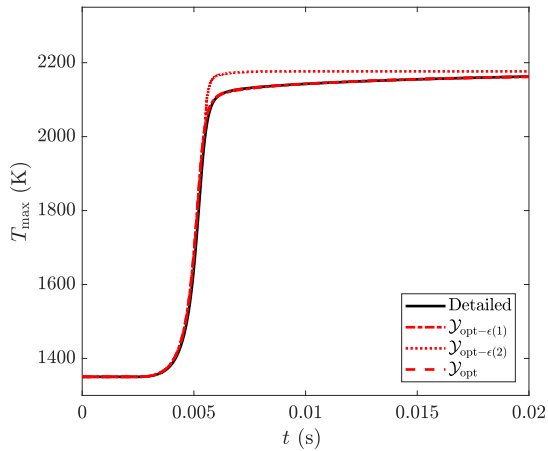


Figure 3.9: T_{\max} as a function of time for IML. A comparison of optimized progress variables from the extremities and knee point of the Pareto front is presented here.

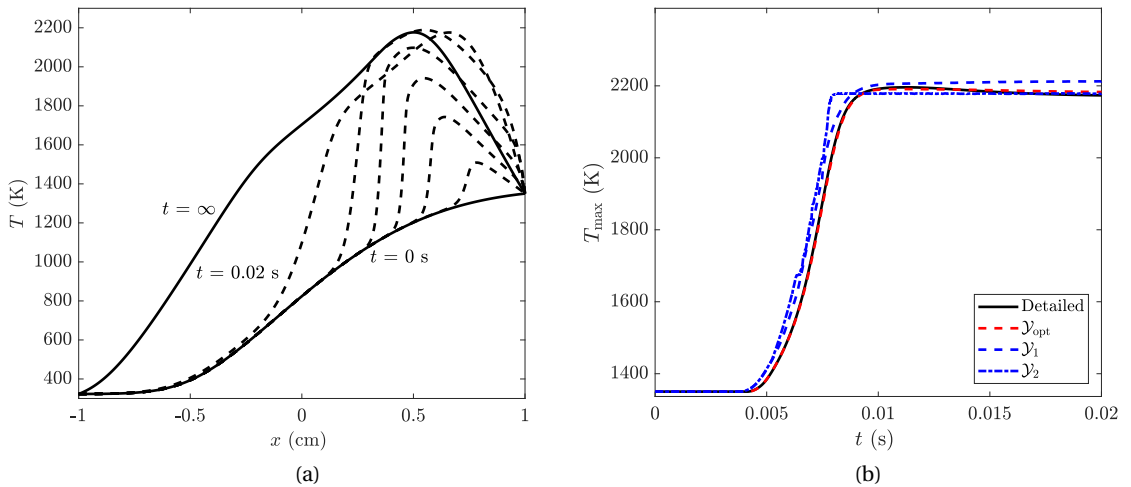


Figure 3.10: (a) The evolution of temperature profile in an ICF of the Cabra vitiated coflow system with a strain rate, $a = 10^{-1} \text{ s}^{-1}$ and (b) the comparison of ignition delays in the ICF using different progress variable definitions.

ence in ignition delay becomes more evident for ICF as the temporal evolution of the reaction progress relies more on the the accuracy of the predicted source terms than the transport of \mathcal{Y} . Here, the conventional progress variables show ignition slightly earlier than the detailed chemistry, while \mathcal{Y}_{opt} reproduces the T_{\max} curve very accurately.

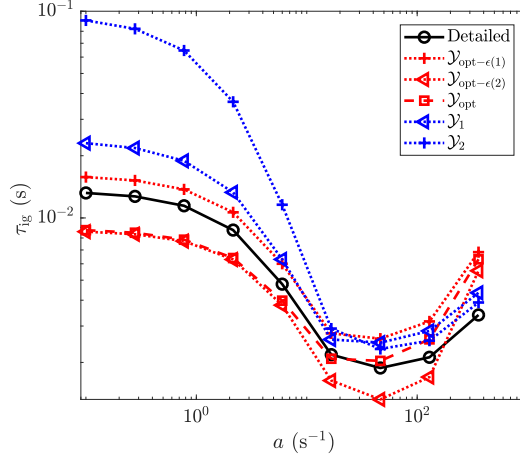


Figure 3.11: Ignition delay of ICFs as a function of strain rate computed using detailed chemistry and FGM table based on IML with different progress variables.

3.3.2 Application of IML based FGM in ICF

It is interesting to investigate how accurate the ignition delay predictions are when an IML based FGM database is used to simulate generic non-premixed ignition scenarios, and to what extent the progress variables play a role in predicting the ignition delays. Therefore, a test of progress variables is devised, to evaluate the efficiency of an optimized progress variable when used in an FGM database constructed from an IML, to simulate a range of ICFs at different strain rates. ICFs with strain rates evenly spaced between 0.1 to 300/s on a logarithmic scale are simulated using detailed chemistry and FGM tables with different progress variables. Manually chosen progress variables \mathcal{Y}_1 , \mathcal{Y}_1 , and the optimized definitions $\mathcal{Y}_{\text{opt}-\epsilon(1)}$, $\mathcal{Y}_{\text{opt}-\epsilon(2)}$, and \mathcal{Y}_{opt} are considered here for comparison. Figure 3.11 shows the trend in ignition delay of ICFs at different strain rates. The ignition delay τ_{ig} is evaluated as the time at which $\Delta T = 10$ K. Among the conventional progress variable formulations, \mathcal{Y}_1 shows a good approximation of ignition delays across the range of strain rates, especially at the high strain rates, which is increasingly dominated by the transport effects compared to the ignition chemistry. The optimized progress variables show better overall agreement especially at low strain rates, with \mathcal{Y}_{opt} bridging the $a - \tau_{\text{ig}}$ curves of $\mathcal{Y}_{\text{opt}-\epsilon(1)}$ and $\mathcal{Y}_{\text{opt}-\epsilon(2)}$. On one hand a good agreement between detailed chemistry and FGM IML results shows the flexibility of an IML FGM table to predict the ignition delays for varying strain rates and on the other, the flexibility is shown to be dependent on the choice of progress variable from the Pareto front of optimal solutions.

3.3.3 Application in DJHC flame

An ideal progress variable needs to be flexible across moderate variations in boundary conditions so that it can be used to construct a higher dimensional FGM, for

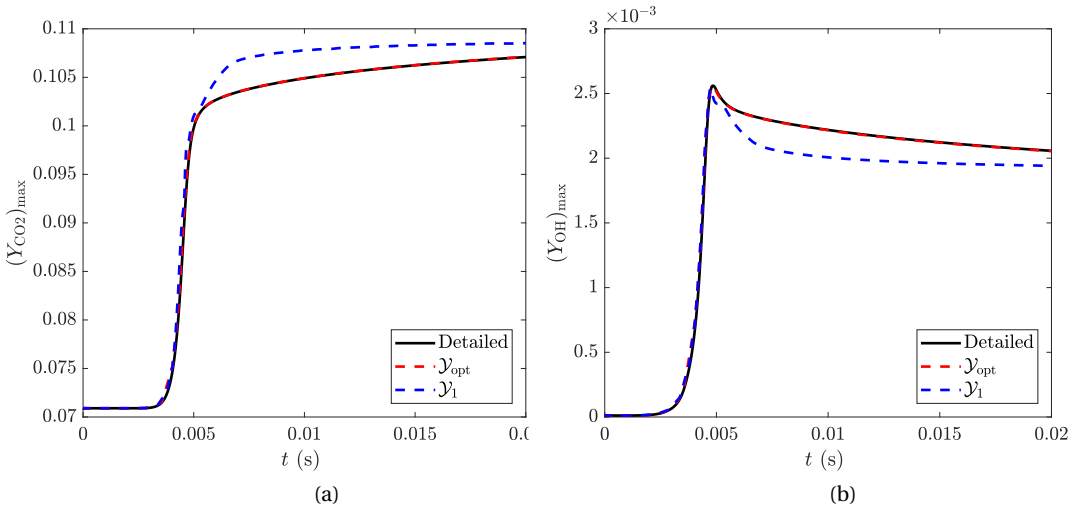


Figure 3.12: The peak mass fractions of (a) CO_2 and (b) OH plotted against time for $Y_{\text{O}_2, \text{ox}} = 0.084$, and $T_{\text{ox}} = 1382 \text{ K}$. The optimized and conventional progress variable formulations are compared here.

instance with heat loss or oxidizer dilution. The DJHC flame provides a test case for varying boundary temperature and oxidizer levels. The DJHC burner consists of a coflow jet that has a radially nonuniform oxygen and temperature distribution, with the lowest temperatures at the periphery of inner and outer bounding surfaces of the coflow jet, along which thermal boundary layers are present [42]. The highest coflow temperatures are observed at about half the radial distance. Similarly, the oxygen distribution shows a trend inverse to that of temperature. Assuming IMLs to represent the reactive-diffusive ignition of a fuel parcels issued from the central fuel jet, a range of ignition delays can be expected. For modeling chemistry in LES of DJHC, FGM tables based on IML flamelets have been used by Abtahizadeh et al. [108] using a manually selected \mathcal{Y} .

The current progress variable optimization method is used on an IML with DNG (Fuel-I) [43] as fuel and an oxidizer with mean oxygen concentration, $Y_{\text{O}_2, \text{ox}} = 0.084$, and a mass weighted average coflow temperature, $T_{\text{ox}} = 1382 \text{ K}$. The values of α_i for this progress variable are given in Appendix 1. A manifold is created with this optimized progress variable and is used to simulate an IML.

Figure 3.12 shows the maximum values of Y_{CO_2} and Y_{OH} against time, from simulations using detailed chemistry and the FGM tables with the optimized progress variable formulation \mathcal{Y}_{opt} and \mathcal{Y}_1 . Both \mathcal{Y}_{opt} and \mathcal{Y}_1 give an accurate reproduction of ignition delay and tabulated species such as CO_2 and OH .

In practical burners with thermochemically non-uniform inlet boundary conditions such as DJHC, manually arriving at a progress variable combination that can accurately capture the ignition delay is more complicated. In case there is a large variation in the performance of \mathcal{Y} with moderate changes in oxidizer temperature and composition, it will be needed to optimize \mathcal{Y} for a larger set of con-

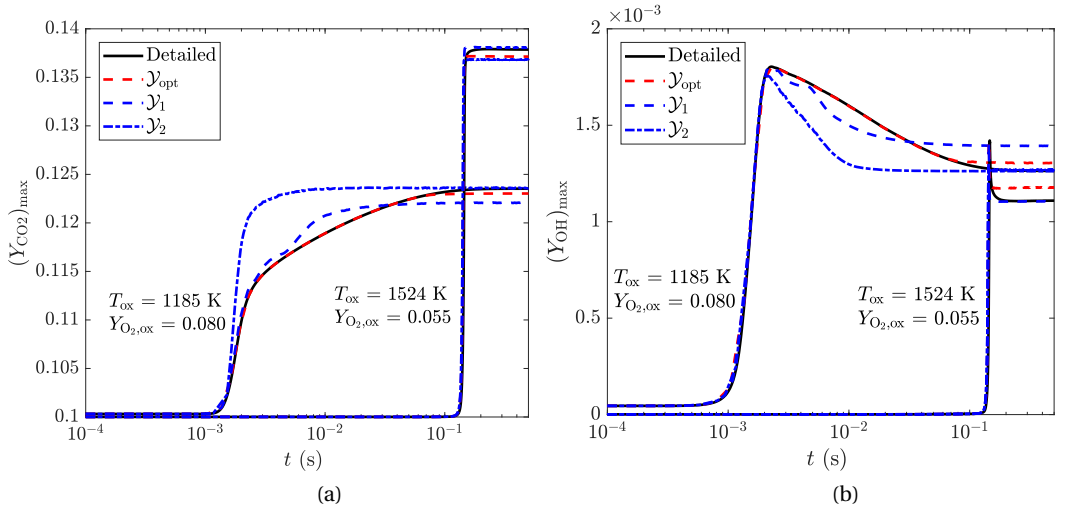


Figure 3.13: Maximum mass fractions of (a) CO_2 and (b) OH plotted against time for the oxidizer conditions from two extreme points in the DJHC-I coflow. The FGM tables are compared against the results from detailed chemistry computations.

ditions to accommodate for instance non-adiabatic effects. However, if the optimized progress variable for averaged coflow properties can prove to be flexible across moderate variations in temperature and composition of the oxidizer, a computationally heavier procedure for optimizing for a 3D flamelet database can be avoided. Hence, the \mathcal{Y}_{opt} obtained for the average coflow properties of DJHC is tested next for flexibility across two extreme points in the coflow.

Figure 3.13 shows the plots of peak mass fractions of CO_2 and OH with oxidizer composition representing two distinct points with the highest and lowest measured temperatures in the DJHC-I coflow. The progress variable \mathcal{Y}_{opt} which is optimized for the mean coflow temperature and oxygen concentration shows very accurate representation of the peak species profiles even with different oxygen and temperatures in coflow, reproducing the ignition delays accurately. The conventional progress variables \mathcal{Y}_1 and \mathcal{Y}_2 reproduce the ignition delays as well. However, deviations are seen from the detailed chemistry results after ignition. So far in this study, the conventional progress variables show a reasonable prediction of ignition delay. Therefore a test case with higher complexity of ignition is investigated in the next section.

3.3.4 ECN Spray-A using n-dodecane.

ECN Spray-A with n-dodecane as fuel has a two-stage ignition, which makes it an interesting candidate to study the current optimization approach further. The reaction mechanism used in this simulation is developed by Yao et al. [107] for n-dodecane, which consists of 54 species and 269 reactions. For an ICF with strain rate $a = 100$ /s, \mathcal{Y}_{opt} is found using the current optimization method. For \mathcal{Y}_{opt} ,

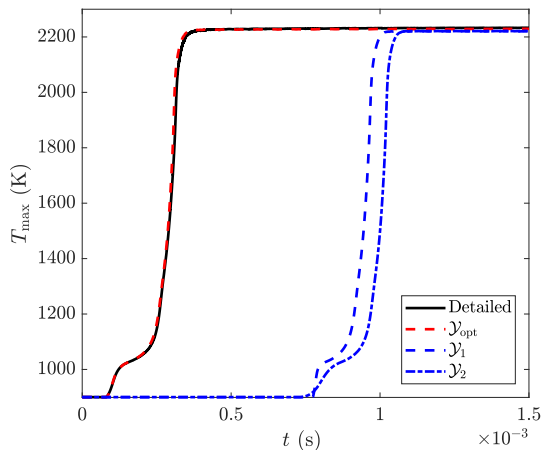


Figure 3.14: Comparison of maximum temperature for ECN Spray-A, with n-dodecane as fuel in an igniting counterflow flame configuration with detailed chemistry and FGM with multiple progress variable combinations. The strain rate is 100/s.

the non-monotonicity $\epsilon(1) = 1.9\%$ and the interpolation error $\epsilon(2) = 0.8\%$. The FGM table used here have 500 grid points in \mathcal{Y} , with the grid distribution based on a power of 3. A grid power of $c = 2$ was found to give slightly inferior results which is not presented here for the sake of brevity. The α_i corresponding to \mathcal{Y}_{opt} is given in the Appendix.

Figure 3.14 shows the ignition delay curves for n-dodecane under Spray-A conditions. The T_{max} plots show a significant improvement in ignition delay prediction by \mathcal{Y}_{opt} over \mathcal{Y}_1 and \mathcal{Y}_2 , which overpredict the ignition delay of n-dodecane to a great extent. Although \mathcal{Y}_1 and \mathcal{Y}_2 are known to be inaccurate for this case, it gives a convincing evidence for the performance of the optimized progress variable. Further, to investigate the dependency of \mathcal{Y}_{opt} 's performance with respect to strain rate, \mathcal{Y}_{opt} for $a = 100/\text{s}$ is used to construct FGM tables for ICFs with strain rates 500/s and 1500/s,

Figure 3.15 shows the ignition delay for ICFs with $a = 100, 500,$ and $1500/\text{s}$, using detailed chemistry and FGM based simulations. T_{max} is predicted with a good accuracy by \mathcal{Y}_{opt} in all three cases. The optimized progress variable accurately captures the two stage ignition for the range of strain rates. T_{max} is slightly advanced at temperatures above 1000 K in simulations using FGM when compared to detailed chemistry results. Interpolation errors in the look-up of progress variable source terms might be the reason for this trend, as the accuracy of progress variable source term interpolation after ignition is not considered in the current optimization procedure.

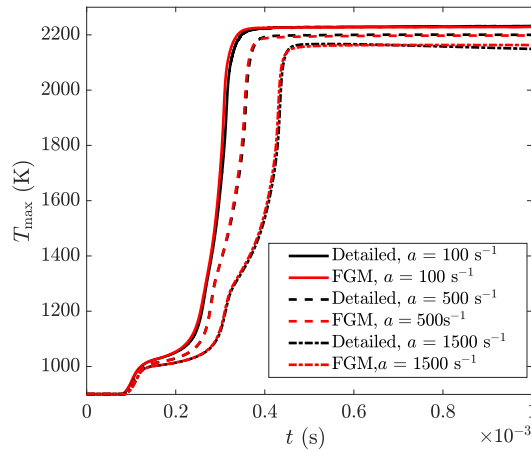


Figure 3.15: Comparison of maximum temperatures in ECN Spray-A at strain rates 100, 500, and 1500/s using detailed chemistry and FGM simulations. The FGM tables are constructed for each of the strain rates using the same progress variable optimized at $a = 100/\text{s}$.

3.4 Conclusion

A new optimization approach to tabulate flamelet generated manifolds for combustion systems is investigated in the current paper for non-premixed flames. The new approach considers the monotonicity of the progress variable as an objective rather than a constraint. Furthermore, a second objective is introduced to minimize the rectilinear interpolation error along the progress variable grid. Such a second condition is very important in cases of sudden/large activity in reactive systems, for instance ignition phenomena as in the current study. A multi-objective optimization is performed using a genetic algorithm for two distinct jet-in hot coflow experiments with methane based fuels and the ECN Spray-A case with n-dodecane. The optimized progress variable reproduces the ignition delay with the highest accuracy, and this becomes visible in case of complex two stage ignition as the ECN Spray-A case, where the conventional progress variables fail to capture ignition delay accurately. The progress variable optimized for a strain rate of 100/s predicts ignition accurately for strain rates 500/s and 1500/s as well, proving a clear advantage of the optimized progress variable over manually chosen progress variables.

The second test case for the new optimization technique is the DJHC experiment, which has a non-adiabatic coflow. The optimization is performed for an IML with the mass-weighted average of coflow temperature and the mean oxygen concentration in the coflow. The optimized progress variable for this condition gives accurate ignition delay predictions for the small variations in the coflow oxygen concentration and temperature. This shows that the optimized progress variable can be used to construct multi-dimensional FGM tables with small variations in boundary conditions or the strain rate. Further analysis is required to evaluate the effectiveness of the optimum progress variable under non-unity Lewis number ef-

fects, as well as for three-dimensional turbulent flames.

Given that the objectives for the optimization method presented here are intended for ensuring accurate ignition delay in non-premixed systems, for cases with a priority on the accurate prediction of other flame characteristics such as pollutant emissions, it will be possible to modify the second objective to accommodate the errors in prediction of the respective parameters.

3.A Appendix

Table 3.3: Optimized progress variable weight composition for Cabra and DJHC flames, based on GRI 3.0 mechanism

Species	α_i Cabra (opt)	α_i DJHC (opt)
H ₂	239540.1474	507.3584
H	21445.4555	-181870.0787
O	158488.2006	122161.8399
O ₂	-15313.4940	-325856.7850
OH	-384736.7618	-132286.5389
H ₂ O	-73692.5653	438091.2953
HO ₂	45151.0942	372661.1847
H ₂ O ₂	-115766.9400	-411192.5910
C	-302076.7942	-764127.8838
CH	221885.0229	55817.8813
CH ₂	323053.6583	-633982.0924
CH ₂ (S)	379907.3805	369836.8699
CH ₃	-540092.9404	513343.8253
CH ₄	-278006.1275	-476049.8038
CO	27556.8739	-111491.3454
CO ₂	153410.5098	-35493.9484
HCO	141827.8596	505564.7988
CH ₂ O	156524.2701	-87371.2555
CH ₂ OH	365843.937	-210370.1379
CH ₃ O	293348.5055	-441392.2708
CH ₃ OH	-317000.8764	-239100.9653
C ₂ H	-56248.7476	623751.0519
C ₂ H ₂	-265942.6137	-663990.0326
C ₂ H ₃	-112969.0757	-444030.5587
C ₂ H ₄	-169602.2704	-777755.5232
C ₂ H ₅	295252.5288	-451579.8401
C ₂ H ₆	276074.4301	119287.5093
HCCO	18780.8503	69062.2359
CH ₂ CO	-325967.1754	718356.6993
HCCOH	73669.0277	-794042.8597
C ₃ H ₇	588835.2732	167173.5427
C ₃ H ₈	465357.1369	-250619.9724
CH ₂ CHO	139650.1377	4598.4231
CH ₃ CHO	48927.5552	-454171.3751

Table 3.4: Optimized progress variable weight composition for ECN Spray-A, based on the mechanism of Yao et al. [107].

ECN Spray-A flame with n-dodecane			
Species	α_i	Species	α_i
H	318653.5802	PC ₄ H ₉	-376612.4552
O	-134639.3971	C ₅ H ₉	-45181.911
OH	-81619.9339	C ₅ H ₁₀	-112986.4359
HO ₂	380937.7077	PXC ₅ H ₁₁	52466.2718
H ₂	30649.21	C ₆ H ₁₂	606744.4967
H ₂ O	10607.6322	PXC ₆ H ₁₃	-292408.0596
H ₂ O ₂	-279798.2194	C ₇ H ₁₄	85913.1702
O ₂	-793569.0819	PXC ₇ H ₁₅	55441.7571
CH ₂	285202.6232	C ₈ H ₁₆	11385.9905
CH ₂ ·	-115385.3507	PXC ₈ H ₁₇	204692.1879
CH ₃	-159138.5916	C ₉ H ₁₈	-493574.436
CH ₄	210539.261	PXC ₉ H ₁₉	326570.1117
HCO	-520660.1328	C ₁₀ H ₂₀	-238556.4302
CH ₂ O	-13578.6333	PXC ₁₀ H ₂₁	-763709.7565
CH ₃ O	-558785.1456	NC ₁₂ H ₂₆	-169925.8099
CO	-630537.5679	PXC ₁₂ H ₂₅	-338507.3069
CO ₂	-567262.9672	SXC ₁₂ H ₂₅	-265189.9112
C ₂ H ₂	685892.358	S ₃ XC ₁₂ H ₂₅	-416606.331
C ₂ H ₃	335641.4872	C ₁₂ H ₂₄	64491.9859
C ₂ H ₄	203514.3022	C ₁₂ H ₂₅ O ₂	446999.8539
C ₂ H ₅	-25879.1021	C ₁₂ OOH	-429210.2443
C ₂ H ₆	6849.9661	O ₂ C ₁₂ H ₂₄ OOH	231022.0618
CH ₂ CHO	-609531.9081	OC ₁₂ H ₂₃ OOH	-7152.4839
AC ₃ H ₅	204879.7827		
C ₃ H ₆	402952.0406		
NC ₃ H ₇	-345673.3907		
C ₂ H ₃ CHO	-72462.4524		
C ₄ H ₇	-143415.4815		
C ₄ H ₈ ₁	-153997.1677		

Modeling Jet in Hot Coflow Flames

Abstract

An Igniting Mixing Layer (IML) based Flamelet Generated Manifold (FGM) approach is implemented in LES modeling of Jet in Hot Coflow (JHC) flames. The modeling criteria required for accurate representation of various flame characteristics are evaluated. Flames in two well-known JHC experimental burners are simulated, namely, the Cabra vitiated coflow burner using methane, and the Delft burner using Dutch Natural Gas (DNG) and a biogas like mixture. Three mixture fraction variance models are applied in the LES of the Cabra burner, and the impact of each model is accessed by comparison of temperature measurements against the simulation results. After validation of the flow field statistics for DJHC, the impact of adiabatic and non-homogeneous boundary conditions on flame lift off heights is investigated. Furthermore a comparison of algebraic and transported variance models for computing sub-grid variance of mixture fraction is performed. A new model for calculating sub-grid scale variance of mixture fraction is formulated, which is based on spatial gradients of mixture fraction obtained from 1D Igniting Mixing Layers. The results obtained using various sub-grid variance models are compared against experimental measurements. Transported variance models are found to be an effective way to capture the flame behavior in DJHC flames. With a refined set of modeling criteria, the variation in flame lift off height with respect to jet Reynolds number is investigated for DJHC flames. Finally, the impact of fuel dilution with CO₂ on flame behavior is analyzed. The study concludes that IML based FGM together with well-chosen submodels for sub-grid scale variance of mixture fraction is able to predict auto-igniting flames in a broad range of conditions 4.3.5.

This chapter closely follows "Modeling Jet in Hot Coflow Flames using an LES-FGM approach" by Vasavan et al. (to be submitted).

4.1 Introduction

Several JHC burners have been introduced lately to study the effects of ignition and MILD combustion. JHC flames serve as the basis for the analysis of effects of recirculation of hot combustion products leading to ignition and flame stabilization. JHC flames show a lifted flame behavior dominated by autoignition where the stabilization is achieved by means of ignition along with a significant influence of turbulence on chemistry [37, 42, 109]. One of the widely studied burners is the Cabra vitiated coflow burner, in which the coupling between turbulence and chemistry was studied by Cabra et al. [40]. In this study a reasonably uniform coflow temperature of 1350 K was achieved using H₂-air flames, at an oxygen concentration of 15%. The fuel jet had a Reynolds number of 28000. Ihme and See [98] studied the

Cabra flame using LES, using an unsteady flamelet based approach for chemistry, accurately predicting the flame lift off height. The Cabra flame was shown to be in the autoigniting regime, rather than in the MILD regime as suggested by Evans et al. [82]. Dally et al. [37] conducted an experimental study with the intention of studying MILD or flameless behavior on a JHC burner called Adelaide JHC (ADJHC) burner, with a mixture of methane and hydrogen as fuel. In this study, a reduction in O_2 from 9% to 3% in the coflow showed a transition of the flame structure from autoigniting to MILD flame according to the definition put forth by Evans et al. [82], along with a significant reduction in CO and NO profiles. Medwell et al. [39] took the study on the ADJHC burner further, by measuring OH, CH_2O and temperature simultaneously for O_2 levels of 9% and 3% in the coflow.

Another jet flame that behaves closer to MILD than the Cabra flame is the Delft JHC (DJHC) flame, in which a range of parameters such as the impact of jet coflow temperatures, oxygen concentration in the coflow, the fuel jet Reynolds numbers, and the fuel types were studied [42, 45, 49]. In this setup the coflow has a radially varying temperature and oxygen concentration, giving rise to additional complexities in CFD modeling of the flames. The fuel jet Reynolds numbers involved here were in the range of 3000 – 8000. The effect of turbulence on autoignition in DJHC flames was analyzed using an LES approach in previous studies [56, 110, 111], and a strong influence of turbulence on chemistry was observed. Abtahizadeh et al. [108] studied the DJHC flame with mixtures of Dutch natural gas and H_2 , by applying the FGM method in LES. A uniform composition, adiabatic, two stream boundary assumption was invoked to simplify the model. DJHC with DNG as fuel was studied using non-homogeneous boundary conditions and a Conditional Source term Estimation approach by Labahn and Devaud [55], obtaining a good agreement with experimental measurements for fuel jet Reynolds numbers of 4500 and 8000.

In a conventional autoigniting flame, a larger oxygen content is present in the hot oxidizer, which leads to a higher temperature rise, whereas achieving the MILD condition requires the system to be oxygen lean. The differences in flame behavior from the Cabra and Delft experiments correspond to the thermophysical changes of a jet flame that undergoes transition from being a conventional autoigniting flame to a MILD flame [23]. The goal of this research is to develop a reliable overarching modeling strategy which is capable of predicting JHC flames undergoing autoignition in MILD or conventional autoigniting flames. By applying various modeling approaches while investigating Cabra and DJHC burners, the criteria for effective modeling of JHC flames are evaluated. In this paper, Cabra and Delft flames are simulated first using uniform heat loss boundary conditions, with the application of Igniting Mixing Layer (IML) based FGM, incorporating the effect of sub-grid scale scalar variances via a presumed β -PDF assumption. This will be the basic reference model used in this study. We further study the influences of

- i. sub-grid scale variance models for mixture fraction,
- ii. IML and ICF based FGM database,
- iii. thermally and compositionally non-uniform inlet condition,
- iv. jet Reynolds number, and

v. fuel composition.

The results thus obtained are compared against experimental measurements for validation and analysis. In the following sections, the computational model for simulating different JHC burners is discussed, followed by the results for the Cabra and DJHC burners. Furthermore, the JHC combustion of biogas is investigated in section 4.3.3, followed by the influence of fuel Reynolds number on flame behavior in section 4.3.5.

4.2 Model description

The Delft and Cabra burners consist both of a concentric pair of burners. For the Delft case, a primary non-premixed gas burner of diameter $d = 4.5$ mm is placed at the center of a coflow jet of 82.8 mm diameter. The fuel considered in the study by Oldenhof et al. [42] is DNG. The coflow is equipped with a ring burner, which operates in a partially premixed mode. The combustion products from this secondary burner produce the hot coflow with a reduced oxygen concentration. The primary burner tube is air-cooled to reduce preheating of the fuel flowing within. The coflow is surrounded by ambient air, and the coflow mixes with the fuel jet on its inner periphery and with ambient air on the outer periphery. Compared to a simple round jet turbulent flame, this configuration leads to a number of challenges in the modeling context:

- A lifted flame stabilizes by autoignition,
- The presence of thermal boundary layers at the peripheries of the fuel and coflow jet,
- Non-uniformity in oxygen concentration across the coflow and fluctuations in coflow temperature and composition.

For the Cabra burner, a large set of small premixed H_2 /air conical flames form the coflow to a central fuel jet of 4.57 mm diameter, ensuring a uniform temperature and velocity distribution in the coflow [40]. The coflow diameter is 210 mm. The above mentioned design aspects are taken into consideration while setting up a numerical model for the simulation of these burners.

In the present work, the jet-in-coflow problem is numerically solved using an LES formulation of the Navier-Stokes equations where the turbulent flow structures of larger, coherent scales are resolved with respect to a mesh dependent implicit filter and the fluid properties and the fluid motion in numerically unresolved sub-grid scales are modeled. The mass and momentum conservation equations are given by,

$$\frac{\partial \bar{p}}{\partial t} + \frac{\partial \bar{\rho} \tilde{u}_j}{\partial x_j} = 0, \quad (4.1)$$

$$\frac{\partial \bar{\rho} \tilde{u}_i}{\partial t} + \frac{\partial \bar{\rho} \tilde{u}_i \tilde{u}_j}{\partial x_j} + \frac{\partial \bar{p}}{\partial x_i} = \frac{\partial}{\partial x_j} \left[\bar{\tau}_{ij} - \bar{\rho} \widetilde{u_i'' u_j''} \right]. \quad (4.2)$$

Here, u_i , p , ρ stand for the velocity components, pressure, and density. Reynolds filtered quantities are represented with an over-line. Favre filtered quantities are represented by a tilde. In Equation (4.2), the RHS stands for the turbulent stress tensor, where $\overline{\tau_{ij}}$ is the laminar part and the turbulent stresses are given by $\overline{\rho u_i'' u_j''}$. The closure of the turbulent stresses is formulated as usual:

$$\frac{\partial}{\partial x_j} \left[\overline{\tau_{ij}} - \overline{\rho u_i'' u_j''} \right] = 2 \frac{\partial}{\partial x_j} \left[(\mu + \mu_t) \widetilde{S}_{ij} \right] \quad (4.3)$$

where the strain tensor \widetilde{S}_{ij} is given by

$$\widetilde{S}_{ij} = \frac{\partial \widetilde{u}_i}{\partial x_j} + \frac{\partial \widetilde{u}_j}{\partial x_i} - \frac{2}{3} \frac{\partial \widetilde{u}_k}{\partial x_k} \delta_{ij}. \quad (4.4)$$

The turbulent viscosity μ_t is calculated based on the Vreman model [112] and μ is the laminar viscosity. The filtered governing equations for mixture fraction, enthalpy and reaction progress variable are solved with the application of the FGM method for representing the combustion chemistry [57].

Favre filtering is applied for every scalar quantity ϕ , using

$$\widetilde{\phi}(t, \vec{x}) = \frac{1}{\overline{\rho}} \int \rho(t, \vec{y}) \phi(t, \vec{y}) G(t, \vec{x}, \vec{y}; \Delta) d\vec{y} \quad (4.5)$$

where G stands for the applied implicit filter kernel and Δ the filter size. The density filtered quantities are related to the corresponding Reynolds filtered values as

$$\widetilde{\phi} = \frac{\overline{\rho \phi}}{\overline{\rho}}. \quad (4.6)$$

Further, the conservation equations for the filtered scalars are given by,

$$\frac{\partial \overline{\rho} \widetilde{Z}}{\partial t} + \frac{\partial \overline{\rho} \widetilde{u}_j \widetilde{Z}}{\partial x_j} = \frac{\partial}{\partial x_j} \left[\left(\overline{\rho} \widetilde{D}_Z + \frac{\mu_t}{Sc_t} \right) \frac{\partial \widetilde{Z}}{\partial x_j} \right], \quad (4.7)$$

$$\frac{\partial \overline{\rho} \widetilde{h}}{\partial t} + \frac{\partial \overline{\rho} \widetilde{u}_j \widetilde{h}}{\partial x_j} = \frac{\partial}{\partial x_j} \left[\left(\overline{\rho} \widetilde{D}_h + \frac{\mu_t}{Pr_t} \right) \frac{\partial \widetilde{h}}{\partial x_j} \right], \quad (4.8)$$

$$\frac{\partial \overline{\rho} \widetilde{Y}}{\partial t} + \frac{\partial \overline{\rho} \widetilde{u}_j \widetilde{Y}}{\partial x_j} = \frac{\partial}{\partial x_j} \left[\left(\overline{\rho} \widetilde{D}_Y + \frac{\mu_t}{Sc_t} \right) \frac{\partial \widetilde{Y}}{\partial x_j} \right] + \overline{\dot{\omega}}_Y. \quad (4.9)$$

where \widetilde{Z} , \widetilde{Y} and \widetilde{h} stand for the filtered scalar quantities, i.e. mixture fraction, reaction progress variable, and enthalpy, respectively. The flames that are studied here burn methane based fuels, where preferential diffusion effects are considered negligible. Therefore, a unity Lewis number assumption is made to calculate the laminar diffusivities of the transported scalars as \widetilde{D}_Z , \widetilde{D}_Y and \widetilde{D}_h ;

$$\tilde{D}_z = \tilde{D}_y = \tilde{D}_h = \frac{1}{\bar{\rho}} \frac{\bar{\lambda}}{c_p}, \quad (4.10)$$

where λ and c_p refer to thermal conductivity and specific heat at constant pressure respectively.

The enthalpy equation is solved neglecting radiation heat losses. The density ρ , the progress variable source term $\tilde{\omega}_y$ and the thermochemical quantities are obtained from an FGM table, which will be discussed further on.

4.2.1 FGM model

The FGM technique is used to model reaction chemistry [77]. The tables for FGM are computed using laminar 1D IML, which account for the effect of a free decaying scalar dissipation rate on ignition [56]. The mixing and reaction of the fuel jet with oxidizer with varying temperature and oxygen concentration need to be taken into account while using 1D IMLs with detailed chemistry. Therefore, the oxidizer boundary conditions in IML simulations are determined based on the temperature and oxygen levels in the coflow.

The 1D mixing layer is formulated as an unsteady counterflow problem, which is numerically solved using the following equations,

$$\frac{\partial \rho}{\partial t} + \frac{\partial \rho u}{\partial x} = -\rho G, \quad (4.11)$$

$$\rho \frac{\partial Y_i}{\partial t} + \rho u \frac{dY_i}{dx} + \frac{\partial}{\partial x} \left(\frac{\lambda}{c_p} \frac{dY_i}{dx} \right) - \dot{\omega}_i = 0, \quad (4.12)$$

$$\rho \frac{\partial h}{\partial t} + \rho u \frac{\partial h}{\partial x} - \frac{\partial}{\partial x} \left(\frac{\lambda}{c_p} \frac{\partial h}{\partial x} \right) = 0, \quad (4.13)$$

where G is the tangential velocity gradient of velocity, and N_{sp} the number of species in the chemical mechanism considered. An ideal IML initial condition ($t = 0$) is given by a Heavyside function separating the fuel and oxidizer at $x = 0$. In practice, the distributions of the mass fractions Y_i and enthalpy h are taken from a counterflow non-reactive solution at a high strain rate of 10^4 s^{-1} to be used as an initial condition for IML simulations. The initial strain field $G(x, t = 0)$ is scaled down from 10^4 s^{-1} to an applied strain rate of 10 s^{-1} at the oxidizer boundary. A small positive strain rate is applied to keep the flame within the prescribed computational domain, with no thermal or concentration gradients at the boundaries. The flamelet equations (4.11-4.13) are solved with CHEM1D [77] using GRI-Mech 3.0 [72] detailed chemistry. Also in the 1D case, a unity Lewis number assumption is introduced while estimating the transport coefficients for the species, ignoring preferential diffusion effects.

The unsteady IML flamelets are simulated over the time interval $t = [0, 1] \text{ s}$ for a range of oxidizer boundary temperatures, T_{ox} , varying from 1100 K to 1600 K and oxygen mole fraction varying from 0.04 to 0.08. T_{ox} and Y_{O_2} are changed simultaneously following the experimental profiles in the coflow (see App. 4.A.2).

Other species at the oxidizer boundary are computed based on the assumption of constrained chemical equilibrium. The laminar flamelets are tabulated as an FGM database along three control variables, namely mixture fraction Z , the reaction progress variable \mathcal{Y} accounting for temporal variations and enthalpy h that parametrizes the variation in enthalpy and oxygen mole fraction in the oxidizer. The mixture fraction Z is defined by using Bilger's definition [113], with a normalization such that, $Z = 0$ at the oxidizer boundary and $Z = 1$ at the fuel boundary. In chapter 3, the progress variable definitions using CO_2 and H_2O are shown to predict the ignition delay accurately in case of methane JHC flames. Therefore, a manually defined progress variable is used for all JHC burners considered in the current study. The reaction progress variable for the current study is defined as

$$\mathcal{Y} = \frac{1}{W_{\text{CO}_2}} Y_{\text{CO}_2} + \frac{1}{W_{\text{H}_2\text{O}}} Y_{\text{H}_2\text{O}} + \frac{1}{W_{\text{H}_2}} Y_{\text{H}_2} . \quad (4.14)$$

where W is the molar mass of the respective species. This definition is considered based on available literature on application of the FGM method in methane flames [114].

The turbulent chemistry interaction for the various thermo-chemical variables is determined using a presumed beta probability distribution function (PDF), which has been successfully used in previous studies [108, 112, 115]. In this method, the non-resolved thermo-chemical quantities at the sub-grid scales are interpreted as the statistical means which follow a PDF distribution defined by $P(Z, \mathcal{C})$, where \mathcal{C} is the normalized progress variable such that at every Z , $\mathcal{C} = 0$ in the unburned mixture and $\mathcal{C} = 1$ in fully burned mixture. The normalization enhances the statistical independence of Z and \mathcal{C} . The non-resolved thermo-chemical quantities are obtained by,

$$\tilde{\phi} = \iint \phi(Z, \mathcal{C}) P(Z, \mathcal{C}) dZ d\mathcal{C}. \quad (4.15)$$

The joint PDF distribution can be expressed as the product of two marginal β -PDFs as,

$$P(Z, \mathcal{C}) \approx P(Z)P(\mathcal{C}), \quad (4.16)$$

where P is the beta distribution computed based on the first two moments of the respective scalars as,

$$P(Z) = P(Z; \tilde{Z}, \tilde{Z}''^2), \quad (4.17)$$

$$P(\mathcal{C}) = P(\mathcal{C}; \tilde{\mathcal{C}}, \tilde{\mathcal{C}}''^2). \quad (4.18)$$

The scaling of mean progress variable and the progress variable variance is obtained based on literature [116]. The above mentioned approach is used for cases with uniform heat loss boundary conditions. For this scenario, the PDF integrated FGM table is prepared with dimensions \tilde{Z} , \tilde{Z}''^2 , $\tilde{\mathcal{C}}$, and $\tilde{\mathcal{C}}''^2$ of size $201 \times 11 \times 201 \times 11$ respectively. The grid for the variances $\tilde{\mathcal{C}}''^2$ and \tilde{Z} , \tilde{Z}''^2 are distributed based on a

power law with an exponent 2, and the grid of the means \tilde{Z} and \tilde{C} are distributed with a power of 1.5, giving maximum resolution in the most sensitive region in the manifold.

For cases with non-homogeneous inlet boundary, h has to be taken into account as well. To restrict the dimension of the FGM database, the following approach is used to calculate the thermo-chemical quantities in the sub-grid scales,

$$\tilde{\phi} = \iiint \phi(Z, C, h) P(Z, C, h) dZ dC dh \quad (4.19)$$

$$P(Z, C, h) \approx P(Z) P_\delta(C) P_\delta(h) \quad (4.20)$$

where $P(Z, C, h)$ refers to joint PDF, and $P(Z)$, $P_\delta(C)$, $P_\delta(h)$ represents marginal PDFs. The suffix δ implies a Dirac-delta distribution of the parameter given by,

$$P_\delta(C) = \delta(C - \tilde{C}). \quad (4.21)$$

The enthalpy fluctuations in the coflow are assumed to be negligible and the sub-grid fluctuations of enthalpy are assumed to be caused by the fluctuations in mixture fraction alone. This assumption simplifies the PDF integration by $P(Z, h) = P(Z)$. In this scenario, the PDF integrated FGM tables are of dimensions \tilde{Z} , \tilde{Z}''^2 , \tilde{h} , and \tilde{C} of size $201 \times 11 \times 11 \times 201$ and grid powers [1.5, 2, 1, 1.5] respectively.

During the turbulent flame computations \widetilde{Z}''^2 and \widetilde{C}''^2 are determined using the following models.

- (i) Algebraic model: Similar to the viscous sub-grid model, the model assumes the SGS characteristic mixing time to be proportional to the SGS turbulent characteristic time [117], yielding

$$\widetilde{\phi''^2}_{\text{alg}} = \alpha \Delta^2 \left(\frac{\partial \tilde{\phi}}{\partial x_j} \right)^2 \quad (4.22)$$

where Δ the filter width, which is obtained from the local cell dimensions as, $(\Delta x \times \Delta y \times \Delta z)^{\frac{1}{3}}$. The value of α is 1/12, as obtained from the Taylor-expansion of the gradient term [118]. This model is based on a local equilibrium assumption and is simpler in application than transported variance models. The quantities \widetilde{Z}''^2 and \widetilde{C}''^2 are computed using this model.

- (ii) Transport model: A more complex model for the transport of scalar variances was proposed by Jimenez et al. [119] which considers the inequality in the generation and dissipation of sub-grid fluctuations for conserved scalars for a more accurate representation of the underlying physics. The transport equa-

tion is given by [57]

$$\begin{aligned} \frac{\partial \bar{\rho} \widetilde{Z''^2}}{\partial t} + \frac{\partial \bar{\rho} \tilde{u} \widetilde{Z''^2}}{\partial x_j} &= \frac{\partial}{\partial x_j} \left(\bar{\rho} (\tilde{D} + D_t) \frac{\partial \widetilde{Z''^2}}{\partial x_j} \right) \\ &+ 2\bar{\rho} (\tilde{D} + D_t) \left(\frac{\partial \tilde{Z}}{\partial x_j} \right)^2 - 2\bar{\rho} D \chi_Z^{\text{sg}} \end{aligned} \quad (4.23)$$

For the transport of scalars, the eddy diffusivity D_t is estimated using a fixed value for the turbulent Schmidt number $Sc_t = 0.4$ [120].

A gradient transport assumption is invoked to obtain the variance production term and the dissipation term is modeled as [100],

$$2\bar{\rho} D \chi_Z^{\text{sg}} = \frac{D_t}{\Delta^2} \widetilde{Z''^2} \quad (4.24)$$

where χ_Z^{sg} is the sub-grid scalar dissipation of Z in the current LES model and Δ the filter width. The mixture fraction variance $\widetilde{Z''^2}$ is computed using this model.

- (iii) Transport model based on laminar gradients: This model uses the same formulation as $\widetilde{Z''^2}$, except the variance source term $\left(\frac{\partial \tilde{Z}}{\partial x_j} \right)^2$ is estimated based on laminar IML flames as, $\frac{\partial Z}{\partial x}(x, t)$ which is projected on the FGM as, $\frac{\partial Z}{\partial x}(Z, \mathcal{Y}, t)$. Further, the laminar FGM is subjected to PDF integration to obtain $\frac{\partial \tilde{Z}}{\partial x}$, which is added as a quantity to be looked up based on the controlling variables $(\tilde{Z}, \widetilde{Z''^2}, \tilde{h}, \tilde{\mathcal{Y}})$ of the table. This assumption is used mainly to artificially enhance $\widetilde{Z''^2}$ at very low values of mixture fraction (close to Z_{mr}), where the resolved gradients in mixture fraction are small. This approach offers a mathematically forced way of reducing the reactivity at low mixture fractions and therefore delaying the ignition, though it could add inaccuracies which are explored in the results section. The mixture fraction variance $\widetilde{Z''^2}$ is computed using this model.

4.2.2 Computational set-up

Table 4.1 provides an overview of the coflow and fuel boundary conditions for the simulations. The 1D flamelets are generated for each burner based on the values provided here. Enthalpy transport is only used for the DJHC flames. The turbulent Prandtl number used in the enthalpy transport equation is assumed to be equal to the turbulent Schmidt number. For every transported scalar, the advective terms are computed following Van Leer's MUSCL scheme, which is third-order accurate, with a minmod flux limiter [121, 122].

In its original implementation, as employed in previous studies [56, 57, 115] the LES solver used a non-conservative form of the scalar transport equations, in which the fluxes were not conserved. In the current study, scalar transport and momentum equations are solved in their conservative form, ensuring continuity of scalar

	Coflow			Fuel				
	T [K]	X_{O_2}	vel. [m/s]	Re	T [K]	Comp.	Vel. [m/s]	Re
Cabra Vitiated Coflow	1375	0.115	5	23300	300	$X_{CH_4} = 0.3275$ $X_{O_2} = 0.1452$ $X_{N_2} = 0.5243$ $X_{H_2O} = 0.0029$	100	28000
	1442	0.076	1.5	2000	400	$X_{CH_4} = 0.85$ $X_{N_2} = 0.15$	25 30 57	3000 4500 8500
	1436	0.088	1.5	2000	400	$X_{CH_4} = 0.81$ $X_{N_2} = 0.144$ $X_{C_2H_6} = 0.037$ $X_{CO_2} = 0.006$	26	3100
	1436	0.088	1.5	2000	400	$X_{CH_4} = 0.567$ $X_{N_2} = 0.105$ $X_{C_2H_6} = 0.026$ $X_{CO_2} = 0.3$	22	3100

Table 4.1: Boundary conditions for various set-ups considered in the current study, indicating which type of boundary condition is used for the coflow, which flamelet type is used for FGM, and which variance model is used for simulation of the Cabra (C) burner, the DJHC-I (D) and DJHC-X (DX) burner.

fluxes and mass. This proved to yield a better match of the centerline profile of average mixture fraction for the simulation of the Cabra burner. The time integration of non-convective terms is performed using the first-order Euler method. The convective terms are computed using the 3rd order Adams-Bashforth scheme.

For DJHC simulations, the computational domain is a Cartesian grid of size 240 mm \times 240 mm \times 360 mm with the largest dimension in the streamwise direction. 160 \times 160 \times 450 cells are used in the computational domain with a minimum cell size of 0.375 mm at the inner core of the fuel jet, which is of the order of the Taylor length scales, to 9 mm at the outer periphery of the coflow jet. The grid resolution varies in stream wise and lateral directions. There are approximately 11.2 million grid cells that are distributed non-equidistantly, stretching from the fuel injection point in all three directions. Velocity components, and the transported scalars have uniform Neumann boundary conditions at the side planes in both x and y direction and at the outflow-plane in z-direction. For pressure, a Dirchlet $P = P_0$ boundary condition is applied at the side planes, in order to prevent cross flow in x and y direction while a Neumann boundary condition is applied at the inflow and outflow plane.

The thermal boundary layer around the fuel jet in case of the DJHC-I and DJHC-X flames are modeled following the experimental measurements, which shows two distinct thermal boundary layers bound to i) the outer surface of the fuel tubing, and ii) the inner surface of the outer tube. The difference between DJHC-I and X is that in the latter there is a greater degree of mixing in the coflow, and therefore the oxygen and temperature profiles have lower radial gradients.

The turbulent velocity inlet is prescribed following the means of the velocity components and Reynolds stress terms measured at a height of 3 mm from the fuel tube exit. The turbulent fluctuations are modeled following a synthetic eddy approach [123]. It captures the means and fluctuations in velocity components at the inlet that matches the measured Reynolds stress components. The LES is initialized with a uniform flow velocity in the domain downstream of the coflow, which is equal to the inlet coflow boundary. A similar initial distribution of scalars is created downstream of the coflow, for the entire domain. The domain downstream of the fuel jet is initialized with zero flow velocity, with the scalars being identical to the coflow. During the initialization of the simulation, the fuel jet velocity is increased from zero to maximum velocity in 500 time steps using a ramp function. The statistics are collected after one domain flow-through time of the jet, $\tau = \frac{L_z}{u_{\text{jet}}} \approx 0.012$ s after every 10 time steps from the center-plane. For flame simulations of the DJHC burner, the timestep $\Delta t = 8 \mu\text{s}$ and for the Cabra burner, $\Delta t = 4 \mu\text{s}$.

4.3 Results and Discussion

Coflow Boundary, h	Flamelet	\widetilde{Z}''^2	C	DI NG	DX NG	DX Bio
Uniform	IML	alg	x	x		
Uniform	ICF	alg	x			
Uniform	IML	1	x	x		
Uniform	IML	2	x	x		
Non-homogeneous	IML	alg		x		
Non-homogeneous	IML	1		x	x	x
Non-homogeneous	IML	2		x		

Table 4.2: Details of LES models used in the simulations

Table 4.2 gives a summary of the various mixture fraction variance models and FGM tables used in the LES for DJHC and Cabra flames. The JHC flames, Cabra, DJHC-I, DJHC-X, are listed from left to right in the table, which is subjected to various modeling assumptions. Further in this chapter, the influence of these modeling assumptions on the LES of JHC are discussed. The results from the current study are organized in steps of complexity of model building. This enables us to discuss the build up of the model from LES with adiabatic boundary to non-homogeneous boundary condition with transported variance model for \widetilde{Z}''^2 . In section 4.3.1 the LES of the Cabra flame which uses adiabatic coflow boundary conditions, is discussed first. With a thermo-chemically uniform coflow, any flame dynamics brought by variation of coflow entrainment is absent, which makes it an ideal case to investigate the influence of variance modeling on flame stabilization. In section 4.3.2 insights acquired from this part of the study is further leveraged in modeling the DJHC-I flame, where an non-homogeneous boundary condition is applied along with different variance modeling approaches. Thereafter, in section 4.3.3, DJHC-X flames are investigated, and the difference in flame stabilization of biogas with respect to DNG is analyzed. Finally in section 4.3.5, using the same LES model, a DJHC-I flame with a varying fuel jet Reynolds number is discussed, and the observations are compared against experimental measurements.

4.3.1 Jet in a uniform hot coflow (Cabra)

Large eddy simulations of JHC flames with the assumption of a thermo-chemically uniform coflow have shown matching results with experimental measurements in previous studies [56, 98]. For experimental setups with relatively uniform coflow conditions, e.g. the Cabra vitiated coflow, a uniform coflow assumption can yield correct flame lift off heights. Using LES with flamelet based models, the flame lift-off behavior of the Cabra flame is well predicted as reported by Ihme and See [98]. Moreover, Abtahizadeh et al. [108] showed that the impact of radiative heat loss on ignition in JHC flames is negligible at low axial distances where ignition occurs. In the current study, the sensitivity of flame lift off height to sub-grid scale variance of mixture fraction is investigated. The performance of IML and ICF based FGM databases in modeling combustion in the Cabra burner is also compared here.

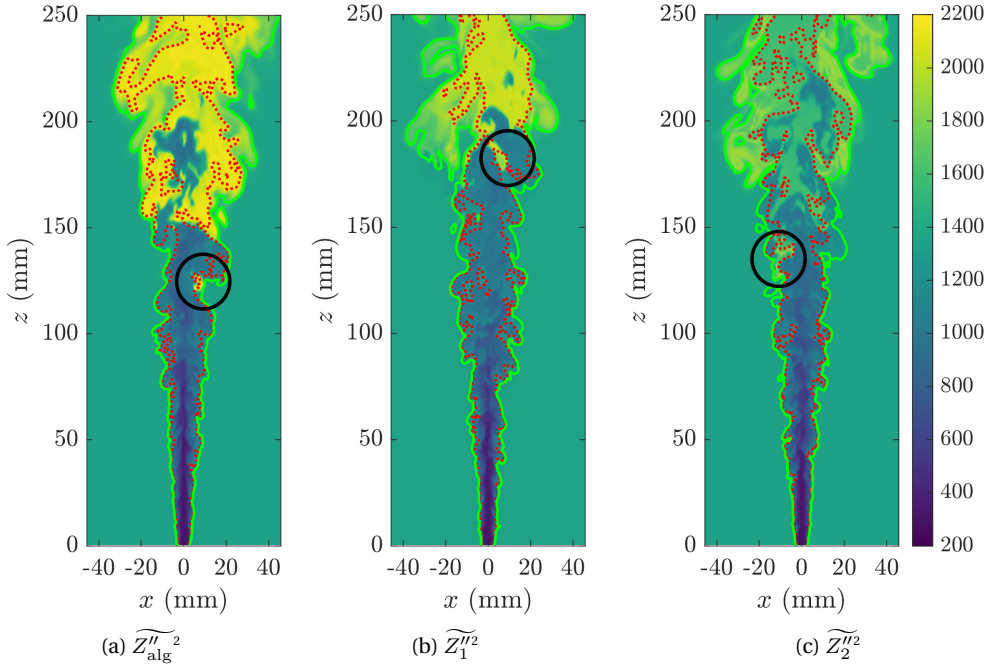


Figure 4.1: Instantaneous center-plane contour plots of temperature \tilde{T} of the Cabra flame, using different sub-grid variance models for mixture fraction: a) $\widetilde{Z''^2_{\text{alg}}}$, b) $\widetilde{Z''^2_1}$, c) $\widetilde{Z''^2_2}$ with iso-contours of $\tilde{Z} = Z_{\text{st}}$ (red) and $\tilde{Z} = Z_{\text{mr}}$ (green). The black circle indicates an ignition kernel.

Figure 4.1 shows instantaneous temperature contours for LES of the Cabra flame. Figure 4.1(a), (b) and (c) correspond to mixture fraction variance calculated with the algebraic model and the transport models $\widetilde{Z''^2_1}$ and $\widetilde{Z''^2_2}$ respectively. The iso-contours of the most reactive mixture fraction $Z_{\text{mr}} = 0.04$, and stoichiometric mixture fraction $Z_{\text{st}} = 0.16$, are indicated as red and green contours respectively. In all three cases, ignition occurs at isolated points, which is a characteristic of autoigniting jet flames. At low axial heights, turbulent mixing is strong enough to dissipate the ignition kernels curbing their growth. As the flow continues further downstream, the mixture fraction iso-contours grow apart, indicating a drop in scalar dissipation and diffusive fluxes. Simultaneously, the ignition kernels form at the most reactive region represented by the iso-contour for Z_{mr} . The black circles in the figure indicate the growth of ignition kernels.

Subsequently the ignition front spreads to higher values of mixture fraction achieving the peak temperatures close to the stoichiometric mixture fraction Z_{st} in case of $\widetilde{Z''^2_{\text{alg}}}$ and $\widetilde{Z''^2_1}$. In the case of $\widetilde{Z''^2_2}$, the peak temperatures occur between the iso-contours of Z_{mr} and Z_{st} , and it shows a much lower temperature at the core of the jet.

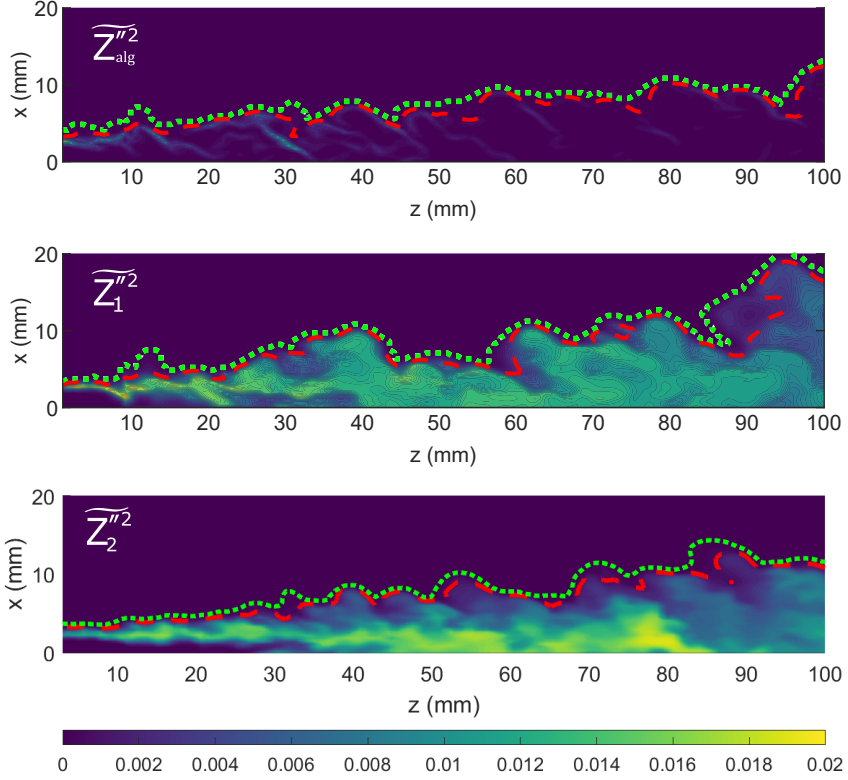


Figure 4.2: Instantaneous mixture fraction variance $\widetilde{Z''^2}$ plot for $\widetilde{Z''^2}_{alg}$ (above), $\widetilde{Z''^2}_1$ (middle) and $\widetilde{Z''^2}_2$ (below) with iso-contours of $\widetilde{Z} = Z_{st}$ (red dashed) and $\widetilde{Z} = Z_{mr}$ (green dashed). Only part of the domain is shown here.

The impact of the model for sub-grid scale variance of mixture fraction, $\widetilde{Z''^2}$ is investigated further for this flame. Transported models for variance result in visible differences in the structure of the flame when compared to the algebraic model. Figure 4.2 shows the center-plane contour plots of $\widetilde{Z''^2}_{alg}$, $\widetilde{Z''^2}_1$ and $\widetilde{Z''^2}_2$ for the Cabra burner. The iso-contours of Z_{mr} and Z_{st} are highlighted in the figure in green and red respectively. It can be seen here that $\widetilde{Z''^2}_{alg}$ is very low in magnitude with the peaks limited to sharp gradients in mixture fraction within the envelope of the Z_{st} iso-contour. As a result, the algebraic variance model shows a spotty flame behavior in Fig 4.1(a) when compared to Fig 4.1(b) and (c). Transported variance models result in significantly higher variances downstream due to the non-equilibrium condition, with $\widetilde{Z''^2}_2$ resulting in high values of variance at the jet core compared to $\widetilde{Z''^2}_1$. This explains the low temperatures at the jet core for $\widetilde{Z''^2}_2$ in Fig 4.1(c).

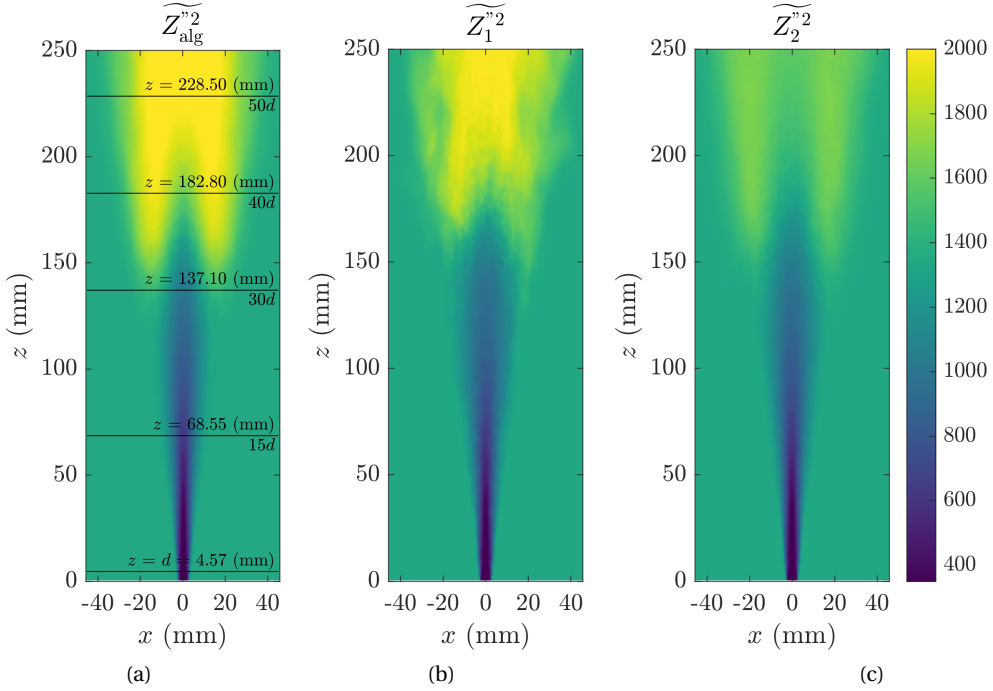


Figure 4.3: Time averaged center-plane contour plots of temperature using different sub-grid variance models for mixture fraction ($\widetilde{Z_{alg}''^2}$, $\widetilde{Z_1''^2}$, $\widetilde{Z_2''^2}$).

Figure 4.3 shows the time averaged temperature contours on the center-plane for the three different models for $\widetilde{Z''^2}$. The flames in all three cases stabilize at and slightly above 137 mm ($30d$, where $d = 4.57$ mm), depending on the sub-grid mixture fraction variance model. This follows that in the simulations, despite the ignition kernels occurring at heights less than $30d$ as shown in Fig 4.1(a), a stable flame base defined by a mean temperature peak occurs slightly above 137 mm height from the fuel jet exit. The main difference due to the variance models is the maximum flame temperature. The various heights at which the experimental measurements were made are indicated in Fig 4.3(a).

Figure 4.4 shows the comparison of radial plots of averaged \widetilde{Z} for different variance models used at various heights above the burner rim. Until a height of 228.5 mm all results are comparable to the experimental measurements in terms of mean mixture fraction profiles. Thereafter, getting a good agreement requires a longer simulation time to generate sufficient statistics. However, for analyzing the autoignition, which occurs at a lower height between 137 mm to 182.8 mm, the mixture fraction profiles from LES are in close agreement with the experiment. An increased radial spread of mixture fraction is visible from 137 mm and above. This is caused by a radially dropping grid resolution, in addition to an early ignition that makes the density drop, causing the fluid pockets to expand radially.

Figure 4.5 shows the comparison of radial plots of averaged \widetilde{T} for different vari-

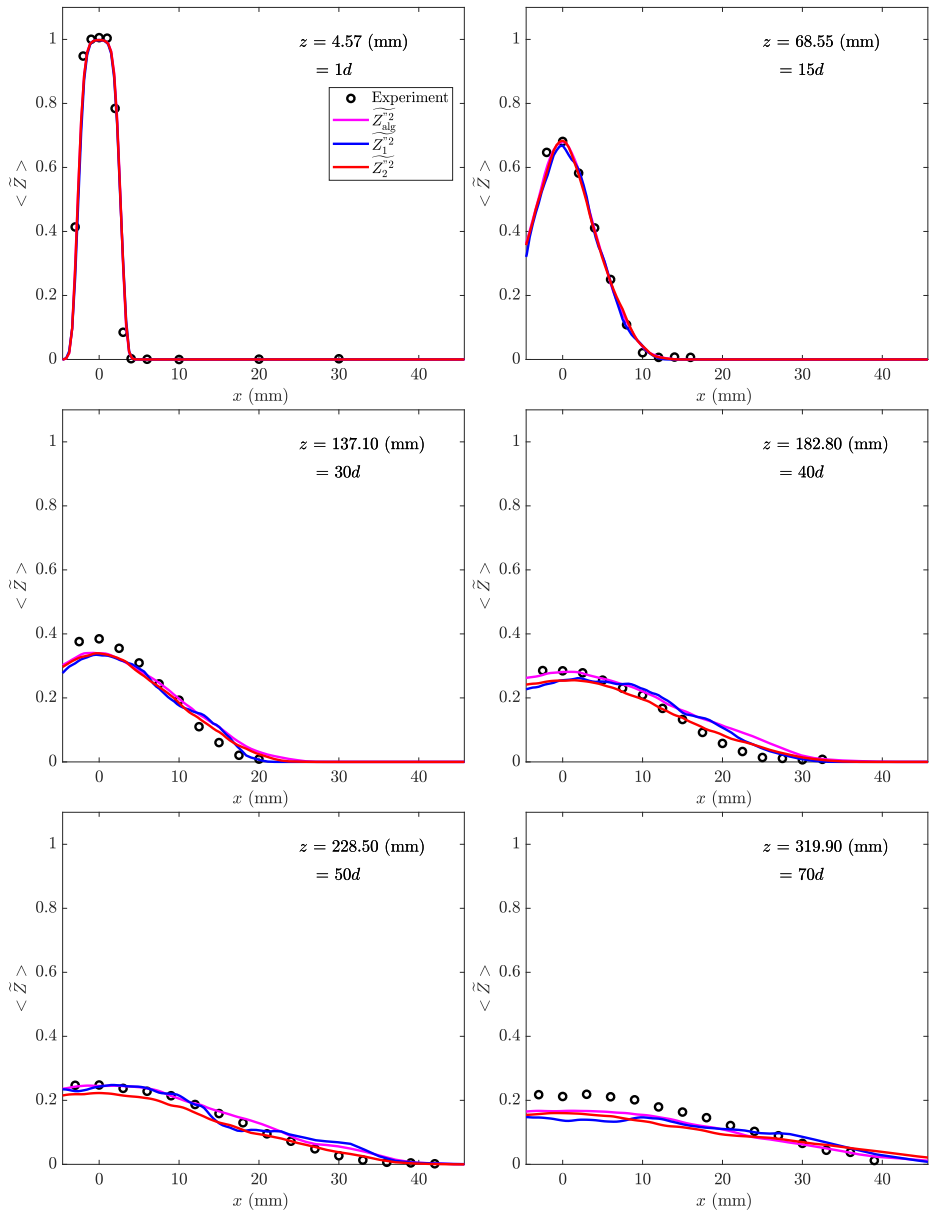


Figure 4.4: Time averaged radial profiles of mixture fraction for Cabra simulation using various sub-grid variance models for mixture fraction.

ance models used for various heights. From a height of 68.55 mm onward, the central region is shown to be mixing with an intensity higher than in the experiment, resulting in a temperature rise at the center of the jet. Further above 137 mm, the presence of a stabilized flame is visible as the peaks in mean temperature, which are higher than the temperature measured. Thereafter, the temperature re-

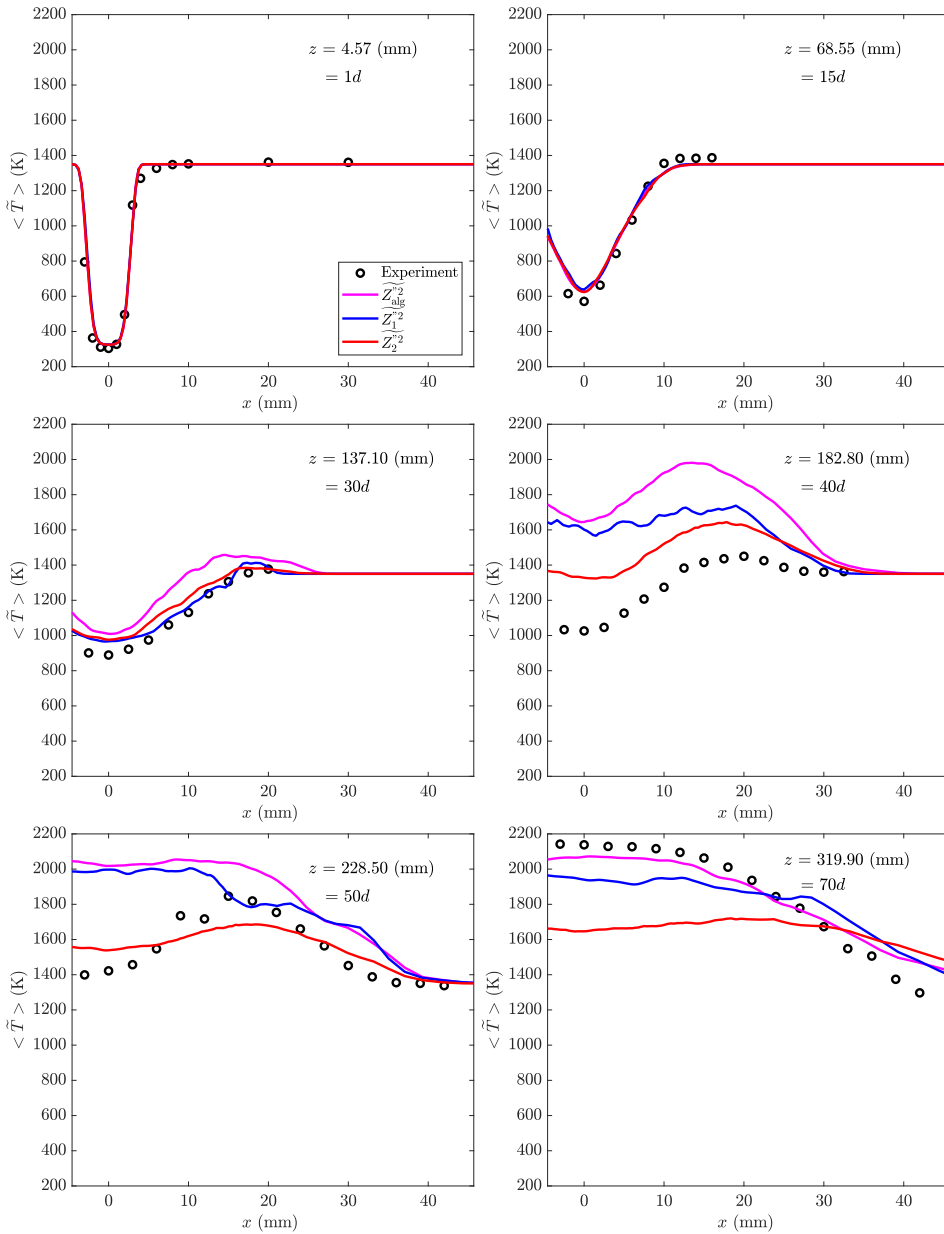


Figure 4.5: Time averaged radial profiles of temperature for Cabra simulation using various sub-grid variance models for mixture fraction.

mains higher than the measured values with the central low temperature region disappearing sooner than in the experiment. This could be related to faster flame spreading, that may originate from the IML assumption [124]. Further investigation is needed to verify the effect of the IML assumption on the flame behavior. An

initial estimate of the influence of an IML based FGM table on the Cabra LES is made by comparing against a simulation that uses an ICF based FGM table. The FGM-IML shows the formation and growth of ignition kernels in the jet flame. The FGM-ICF requires flamelets at any given strain rate applicable to the jet, which if considered in the model, adds a dimension to the FGM database.

Figure 4.6 shows instantaneous snapshots of temperature at the center-plane of LES cases with, i) a mesh with lower resolution than the reference case, ii) a mesh with higher resolution, and iii) with an ICF based FGM table instead of IML (at a strain rate of 10/s). A change in mesh resolution is shown to have minor influence on the flame lift-off height compared to the ICF assumption. The size of the ignition kernels shows a dependence on the grid resolution as in larger cell volumes the filtered progress variable source term increases along with the mesh dependent filter size. With larger cells, the ignition kernels are seen to be larger thus the flame lift-off is reduced. With the ICF assumption, the flame is ignited further above 137 mm, and the spotty behavior that is seen with IML is diminished. It is expected that in IML the assumption of a high scalar gradient results in an enhanced diffusion flux of reactive radicals from the most reactive mixture fraction Z_{mr} , therefore leading to an earlier ignition. Hence it can be seen that with the use of FGM-IML, the effects of decaying mixture fraction gradient is represented by the mixing layer assumption, leading to the formation of ignition kernels further upstream when compared with FGM-ICF. FGM-ICF is constructed with flamelets of a low strain rate (10/s) therefore the development of flame ignition is estimated under low scalar dissipation. When applied in a turbulent environment with a large scalar dissipation, the progress variable source term in FGM-ICF is strongly dissipated and flame development is delayed till local scalar dissipation is low enough to allow the ignition to develop into a stable flame front. An FGM-ICF model with scalar dissipation as an additional controlling parameter can represent the interplay between scalar dissipation and ignition. However, this is a computationally costly step. Therefore FGM-IML, which incorporates the effect of a decaying scalar dissipation rate on ignition without requiring an additional controlling parameter, is chosen to model the lifted flames in the current study.

With the available results of FGM-IML, the differences between the variance models can be analyzed from the instantaneous iso-surfaces of mixture fraction. Figure 4.7 shows 3D iso-surfaces of $Z_{mr} = 0.04$, where the onset of ignition is captured as the color contours of \tilde{Y} on the iso-surface of Z_{mr} . The figures are corresponding to simulations with $\widetilde{Z''_{alg}{}^2}$ and transported variance model $\widetilde{Z''_1{}^2}$. It is seen in Figure 4.7(a) that the peaks in \tilde{Y} occur at the inner edges of smaller eddies, where the oxidizer gets entrained between the eddies creating zones with a fast drop in the scalar dissipation rate that stimulate ignition. Figure 4.7(c) further elucidates this mechanism, where a section of the center-plane temperature contours is shown. The mixture fraction iso-contour for Z_{mr} is indicated in red here. From the varying normal distance between the mixture fraction iso-contours, it can be seen here how the gradient in mixture fraction decreases at the meeting point of two adjacent eddies, which results in an ignition spot. FGM-IML incorporates the combined effect of decreasing scalar dissipation and reactions leading to ignition, thereby not requiring an additional controlling variable for scalar dissipation or strain rate for the FGM table. The Z_{mr} iso-surface also shows that further downstream the flame

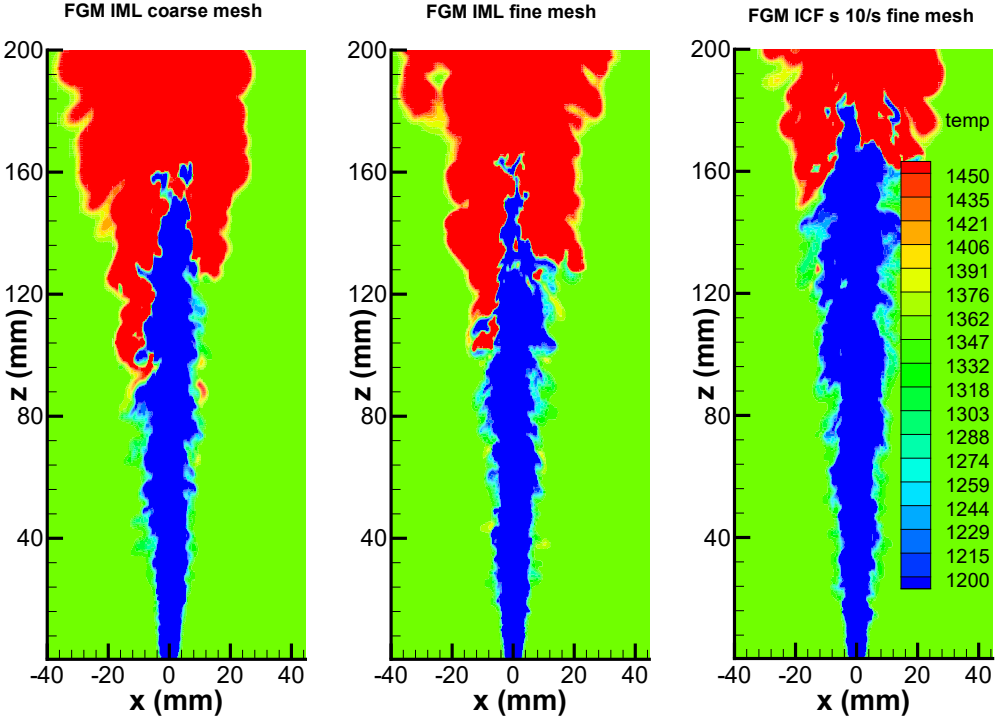


Figure 4.6: Contour plots a) & b) have a coarser and finer grid resolution than the nominal value. c) uses an FGM table based on ICF instead of IML, showing delayed ignition. The color range is limited to 1200, 1450 K.

is stabilized. Figure 4.7(b) shows the formation of a flame further downstream than found in Fig. 4.7(a). In Fig. 4.7(b), a more gradual increase in $\tilde{\gamma}$ is seen along the flow structures further downstream, where the scalar dissipation rates are low. As shown in Fig. 4.5, at heights $30d$ and $40d$, the radial profile of $\langle \tilde{T} \rangle$ shows a better match with measurements for $\widetilde{Z_1''^2}$ and $\widetilde{Z_2''^2}$, compared to $\widetilde{Z_{alg}''^2}$, which suggests that the algebraic variance model predicts significantly higher rate of ignition at the turbulent flame base. This results in a too small flame lift-off height. As the main interest of the study is around flame lift-off heights, from here onwards transported variance models are given preference to estimate the sub-grid variance levels of mixture fraction for JHC flames.

4.3.2 Jet in non-uniform coflow (DJHC-I)

The DJHC-I flame presents a non-uniform coflow boundary where the temperature and oxygen concentration varies radially. In the DJHC-I flame considered here, the fuel jet has a Re of 4500. In such a scenario, the entrainment of coflow into the jet

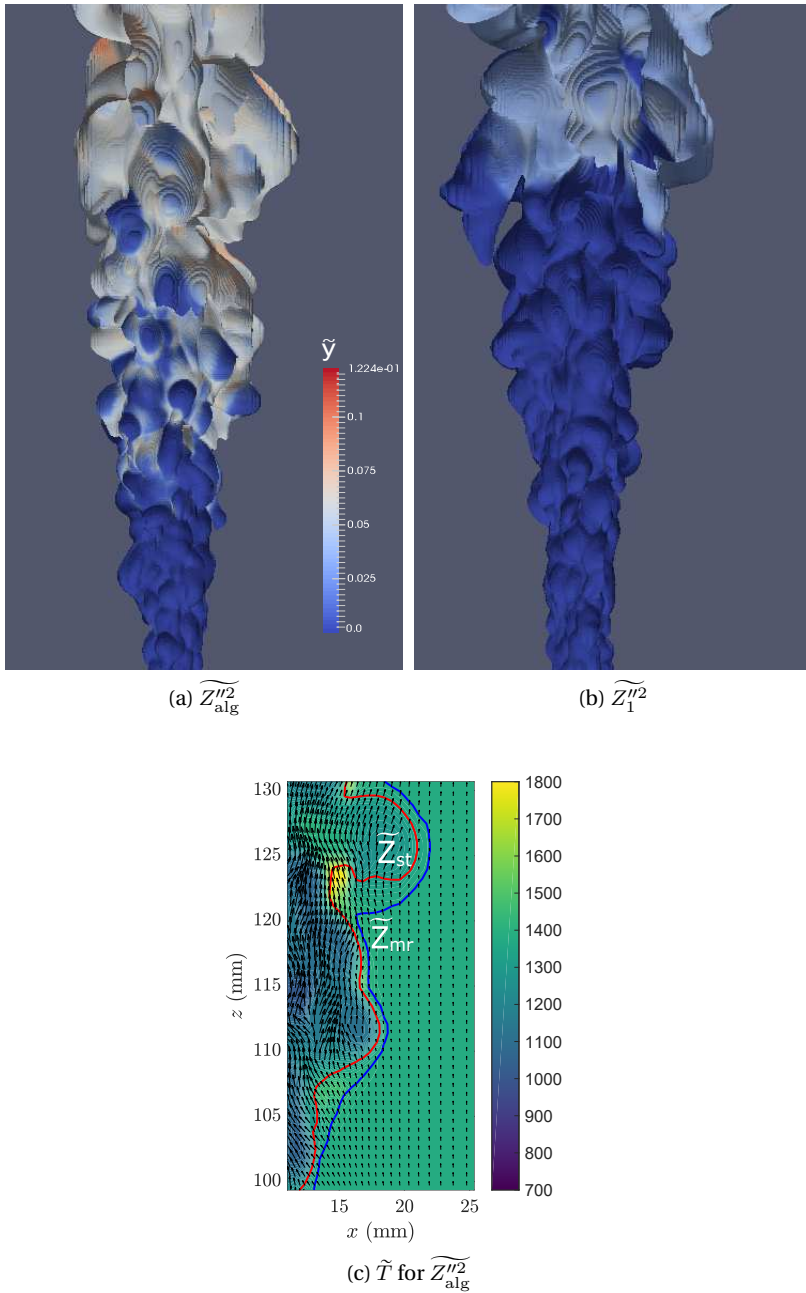


Figure 4.7: Instantaneous iso-surfaces of $\widetilde{Z} = Z_{mr} = 0.04$ colored by \widetilde{y} for a) \widetilde{Z}''^2_{alg} and b) \widetilde{Z}''^2_1 . The figure is oriented to have a view on the inner edges of the iso-surfaces. c) Shows the center-plane contours of instantaneous temperature \widetilde{T} for \widetilde{Z}''^2_{alg} , with iso-contours of Z_{mr} in blue and Z_{st} , along with the local velocity vectors.

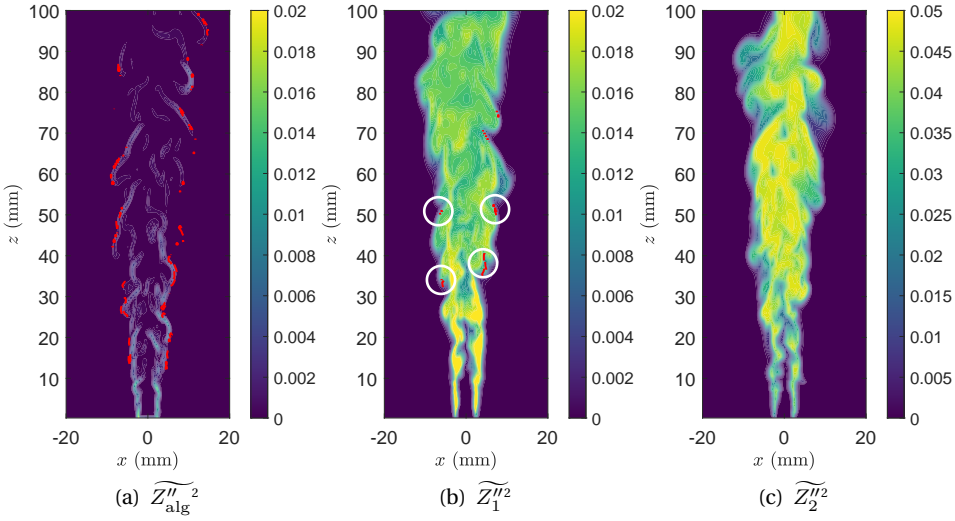


Figure 4.8: Instantaneous center-plane contours of \widetilde{Z}''^2 using three different variance models, with iso-contours of the progress variable source term $\tilde{w}_y = 100 \text{ s}^{-1}$ (red) on top. Note that the whole domain is not shown.

has a larger influence on flame stabilization than in a jet with homogeneous coflow.

Figure 4.8 shows the instantaneous center-plane contours of the sub-grid variance of mixture fraction, computed using algebraic and transported variance models for a jet Re of 4500. The figure shows iso-contour of the \tilde{w}_y (1/s) to indicate ignition, which is defined as,

$$\tilde{w}_y = \frac{\overline{\rho \dot{w}_y}}{\overline{\rho}} = \frac{\dot{w}_y}{\overline{\rho}} \quad (4.25)$$

where \dot{w}_y ($\text{kg}/\text{m}^3\text{s}$) is the mass based progress variable source term. The iso-contour of $\tilde{w}_y = 100 \text{ s}^{-1}$ indicates the spots of ignition. The algebraic model results in the least variance magnitudes and therefore ignition occurs approximately at $z = 15$ mm. In Fig. 4.8(b) isolated ignition spots occur at heights above 30 mm with $\widetilde{Z}_1''^2$, which has a significant difference in magnitude and distribution than $\widetilde{Z}_{\text{alg}}''^2$. Here the flame kernels are unable to sustain or grow in the immediate vicinity of the fuel jet where a laminar IML flamelet could have achieved ignition (in ≈ 1 ms). For $\widetilde{Z}_2''^2$ in Fig. 4.8(c), there are no ignition spots observed till a height of 100 mm, due to a possible suppression of reactivity resulting from the highest variance levels among the three models considered here. The effect of variance models on the flame behavior is further analyzed in the next section.

In comparison with the Cabra flame, DJHC flames have non-homogeneous coflow boundary conditions leading to a higher reactivity at low mixture fractions. A uniform temperature coflow is a possible modeling simplification of the DJHC setup that has been previously applied in studies [56, 108], reducing the degrees of free-

dom of the FGM required to describe the composition and temperature, simplifying the chemistry tabulation. This assumption also results in overcoming the need to transport enthalpy and thus reducing the overall computational time. In a uniform coflow, the fuel jet entrains the coflow stream with uniform thermo-chemical composition and the flame stabilization depends mainly on the entraining flow structures. In this case the flow field alone can control the flame stabilization by means of entrainment leading to ignition.

When non-uniform coflow conditions are considered, the effect of history of diffusion along a mixture fraction iso-contour is not isolated from the thermal mixing with the coflow. Instead, as the fuel jet progressively mixes with the higher temperature region in the coflow, the ignition sets in due to the high temperature of the oxidizer. Therefore, flame quenching effects near the nozzle are expected to play a less significant role in deterring the flame stabilization, when compared to a uniform coflow. In this section we investigate in detail the influence of variance modeling strategies on the mechanism of flame stabilization. The LES simulations are run with the configuration applied by Abtahizadeh et al. [56] for the DJHC flames with a non-uniform coflow temperature and oxygen concentration. To draw a comparison between non-homogenous coflow boundary condition and uniform coflow assumption, the DJHC-I flame is also simulated using a uniform coflow boundary condition with radially averaged temperature and oxygen concentration. The results from the DJHC-I flame simulations with uniform and non-uniform coflow assumptions are discussed in the following sub-sections.

Mean axial velocity

Firstly, the mean axial velocity measured with the DJHC experiment is compared against the values from the LES simulations in Fig. 4.9 at various axial positions with the two transported variance models $\widetilde{Z}_1''^2$ and $\widetilde{Z}_2''^2$. In both simulations with non-uniform coflow, the mean values of velocity show a good match with the experiment in the central region of the jet. At radial locations larger than 10 mm, both models start to diverge from the measurements. The two variance transport models perform quite similar, but $\widetilde{Z}_1''^2$ shows a slightly better overall agreement in terms of velocity, and $\widetilde{Z}_2''^2$ yields a higher velocity in the regions close to the jet origin than the measurements, which decays faster than the experimental measurements in subsequent downstream locations. This could be a result of a higher sub-grid scale variance, that results in increased mixing, lowering the density in the initial section of the jet, and increased viscosity slowing down the jet downstream. The coflow velocity starts to depart from the measurements as the height increases. The outer radial locations have lower resolution than the inner region. This constitutes to higher predicted values on sub-grid viscosity, resulting in an increased deceleration of the coflow in the simulations. This may affect the entrainment of coflow downstream, which is important for the ignition of fluid pockets emerging from the central jet.

The results for cases with a uniform coflow inlet boundary condition is presented in Fig. 4.9 with UC (Uniform Coflow) in the legend entries, where the averaged velocity profiles for uniform coflow show slightly larger spread than the corresponding non-homogeneous cases. The uniform coflow boundary condition uses

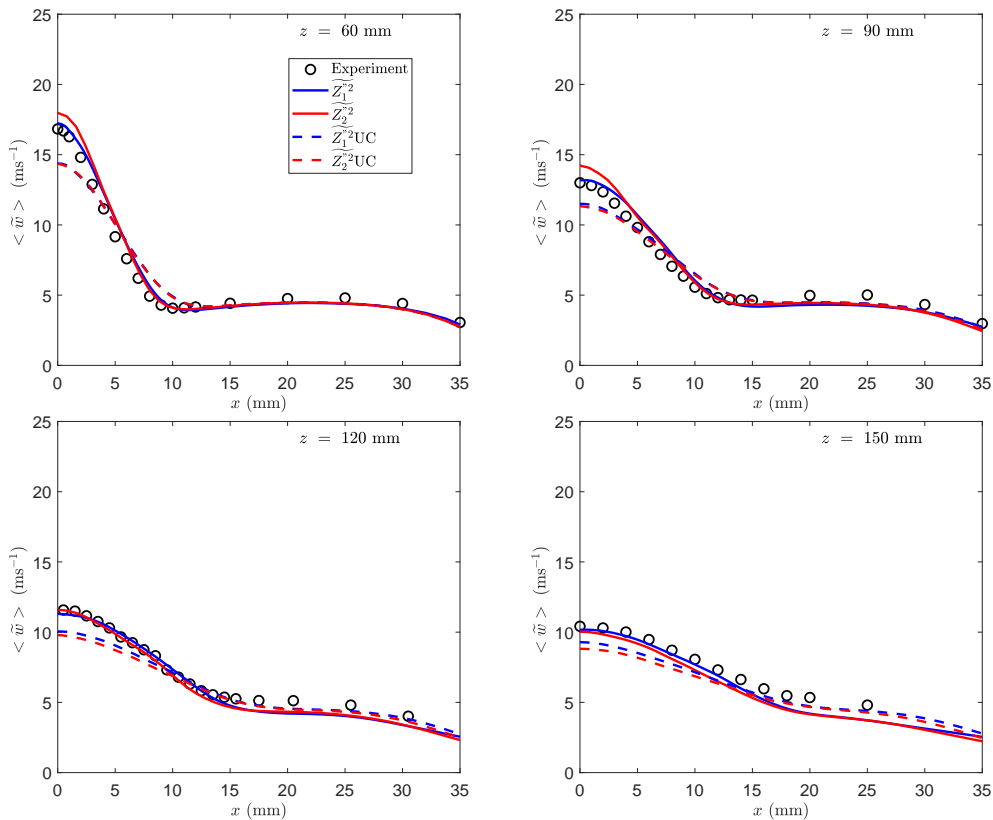


Figure 4.9: Time averaged radial profiles of axial velocities $\langle \tilde{w} \rangle$ in DJHC-I at various axial locations for various models, compared with experiment. UC in the legend entries correspond to cases where a Uniform Coflow boundary condition is applied.

temperature and oxygen levels that are radially averaged from experimental measurements of coflow inlet. In the simulations, the coflow velocity was not adjusted when the coflow temperature is changed. Therefore, the density distribution necessary for an accurate representation of the velocity field is correctly represented with the non-homogeneous boundary.

Mean and rms temperatures

Figures 4.10 and 4.11 show the measurements of mean (\tilde{T}_{mean}) and rms (\tilde{T}_{rms}) temperatures for the DJHC-I flame against the Reynolds averaged radial profiles from LES. Cases with uniform and non-uniform coflow enthalpy are presented here. Using $Z_1^{\prime\prime 2}$, for non-uniform coflow inlet, there is a clear peak in the temperature profile at heights of 60 mm and 90 mm at a radial location near 10 mm. From the plots of rms temperature, the fluctuation in temperature at this radial location exceeds the measurements by 100 K. However at heights of 120 mm and 150 mm, the tem-

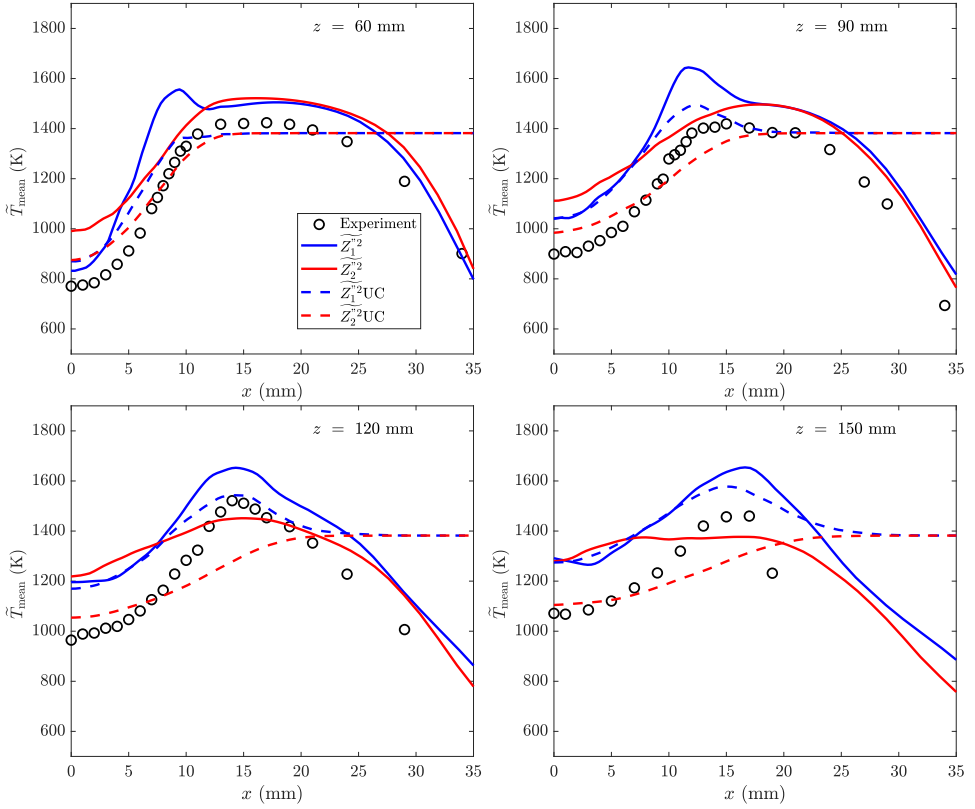


Figure 4.10: Time averaged radial profiles of Favre filtered temperature \tilde{T} at various axial positions in DJHC-I.

perature profiles have a matching shape of the measured temperature and fluctuation profiles with a difference of roughly 100 K, and the temperature rms fluctuation appears to match better with the measured values. These results indicate that at a lower height of 60 mm, a higher mean temperature is predicted in LES than what is given by the measurements. This intense flame results in a greater temperature rise and in the absence of radiative heat loss the temperature rise is sustained further downstream resulting in a uniform offset from the measured values.

With both coflow boundary conditions, the mean and rms profiles of \tilde{T} for $\widetilde{Z_1''^2}$ indicate the presence of a flame. In the range of 15-20 mm radially, at heights of 90-120 mm, the temperature fluctuations show a close match with measurements. This shows that, for a flame region with stable burning, the fluctuations are correctly captured by both the inlet modeling approaches. In the case of $\widetilde{Z_1'' UC^2}$, the presence of a flame is not evident from the temperature fluctuations.

In the non-homogeneous coflow case, the variance model $\widetilde{Z_2''^2}$ leads to a temperature profile without a clear peak at $z = 60$ mm and the peak rms temperature fluctuations are matching the experiment. At a height of 90 mm, the mean temperature profile still is without a peak, and the rms values flatten out as if there is

no reaction. The results start to deviate further from the experimental results at heights of 120 mm and 150 mm. For the uniform coflow inlet, with $\widetilde{Z}_2''^2$, there is also no visible peak in mean temperature occurring at the axial locations considered here. The peak temperature fluctuations keep decreasing with downstream distance.

From both coflow inlet models with $\widetilde{Z}_2''^2$, we see that in the absence of a clear peak in the mean temperature, the temperature fluctuations are predicted correctly at 60 mm. This suggests that in the experiment there is no ignition there, and the temperature fluctuations correspond to turbulent mixing alone. By 90 mm and above we see that the temperature fluctuations with $\widetilde{Z}_1''^2$ match better with the experimental measurements, however the ignition is visible already at 60 mm in the simulated temperature fluctuations.

The major difference in the outcome of these two variance models points to ignition between 60 and 90 mm in the experiment. $\widetilde{Z}_2''^2$ has a stronger variance in source term in sub-grid level, which leads to reduced reactivity. $\widetilde{Z}_1''^2$ yields a relatively lower mixture fraction variance, leading to a higher reactivity for the flame at the heights of 60 mm and 90 mm. The temperature variance shows that the flame dynamics from 90 mm onwards is captured better by this model. Thus from here on $\widetilde{Z}_1''^2$ will be used for DJHC flames.

4.3.3 Biogas JHC simulations (DJHC-X)

Compared to DJHC-I, DJHC-X has a significantly more uniform oxygen and temperature profile in the coflow. The average oxygen concentration in the coflow is the same for both cases, however the fuel jet $Re = 4500$ for DJHC-I and 3100 for DJHC-X. The transported variance model $\widetilde{Z}_1''^2$ is used here. The top row of Fig. 4.12 shows the instantaneous temperature and OH center-plane contours for the DJHC-X flame using DNG, while the bottom row shows the biogas results. The temperature contour plot for DNG shows the hot oxidizer being entrained into the fuel stream, and pockets of ignition are visible from a height of 60 mm. The corresponding instantaneous contours of OH show the independent ignition kernel formation in the periphery of the fuel stream. The averaged contour plot of OH also contains temperature iso-contours of 1100 K and 1200 K, and mixture fraction iso-contours of Z_{mr} where the ignition starts and Z_{st} where the flame stabilizes. The averaging of ignition kernels over time yields a gradually increasing OH mass fraction from $z = 50$ mm till 100 mm, where the ignition kernels form and interconnect to develop into a continuous flame front. The peak OH mass fraction lies on the stoichiometric mixture fraction iso-contour, and the base of the flame coincides with the point where the temperature iso-contour of 1200 K from the oxidizer side meets the iso-contour of Z_{mr} , which indicates the triggering of ignition due to the increased availability of hot oxidizer from the core of the oxidizer stream.

The bottom row of Fig. 4.12 shows the instantaneous center-plane contours of temperature and OH mass fraction, along with the averaged center-plane contour of OH for the biogas-like fuel (DNG+CO₂). Compared to Fig. 4.12(a) the instantaneous temperature contour shows a thicker flame that has larger wrinkling structures than the DNG flame. The instantaneous OH contour shows a similar behav-

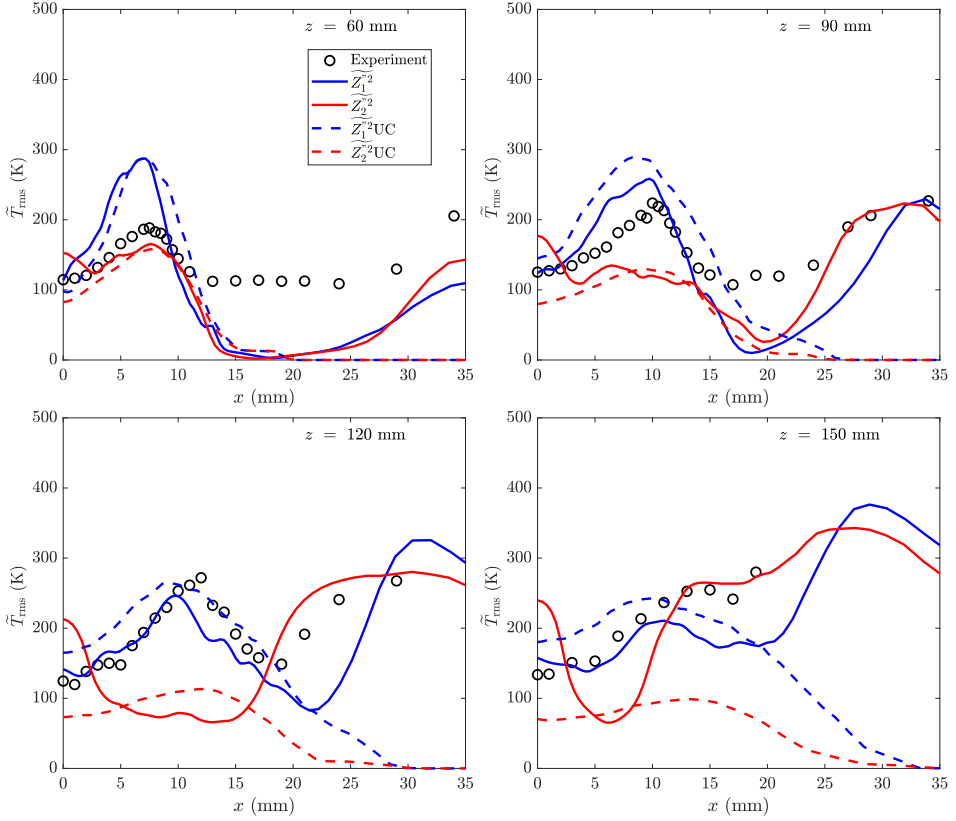


Figure 4.11: Radial profiles of rms of temperature compared against DJHC-I measurements.

ior with independent spots of OH appearing closer to the center line of the jet. Two factors could be contributing to the flame thickening effect: i) a higher value of Z_{mr} leads to a faster spread of the reaction zone, ii) a wider zone of heat release that leads to the suppression of turbulence, suppressing small eddies. These effects lead to larger flow structures in the appearance of the instantaneous flame, leading to a faster mixing towards the center of the jet. In the averaged center-plane contour we see that compared to the DNG OH distribution, the growth in OH mass fraction between 50 mm to 100 mm is slower in the case of biogas. However the center-plane contours of mean OH do not directly ensure that ignition kernels are originating separately, or being the cross sections of an interconnected 3D flame structure. Therefore, a series of depth-integrated OH contour plots are presented next.

Figure 4.13 shows three snapshots of OH mass fraction integrated normal to the depth of the center-plane, given by $\int_{-\infty}^{\infty} \tilde{Y}_{OH} dy$ [m], at three time intervals with a gap of 0.8 ms. The center-plane contours of Z_{mr} and Z_{st} serve as the reference for visualizing the shape of the mixing field and thereby the flame. In Figure 4.13(a), the iso-contours of mixture fraction show dents at a height of approximately 60

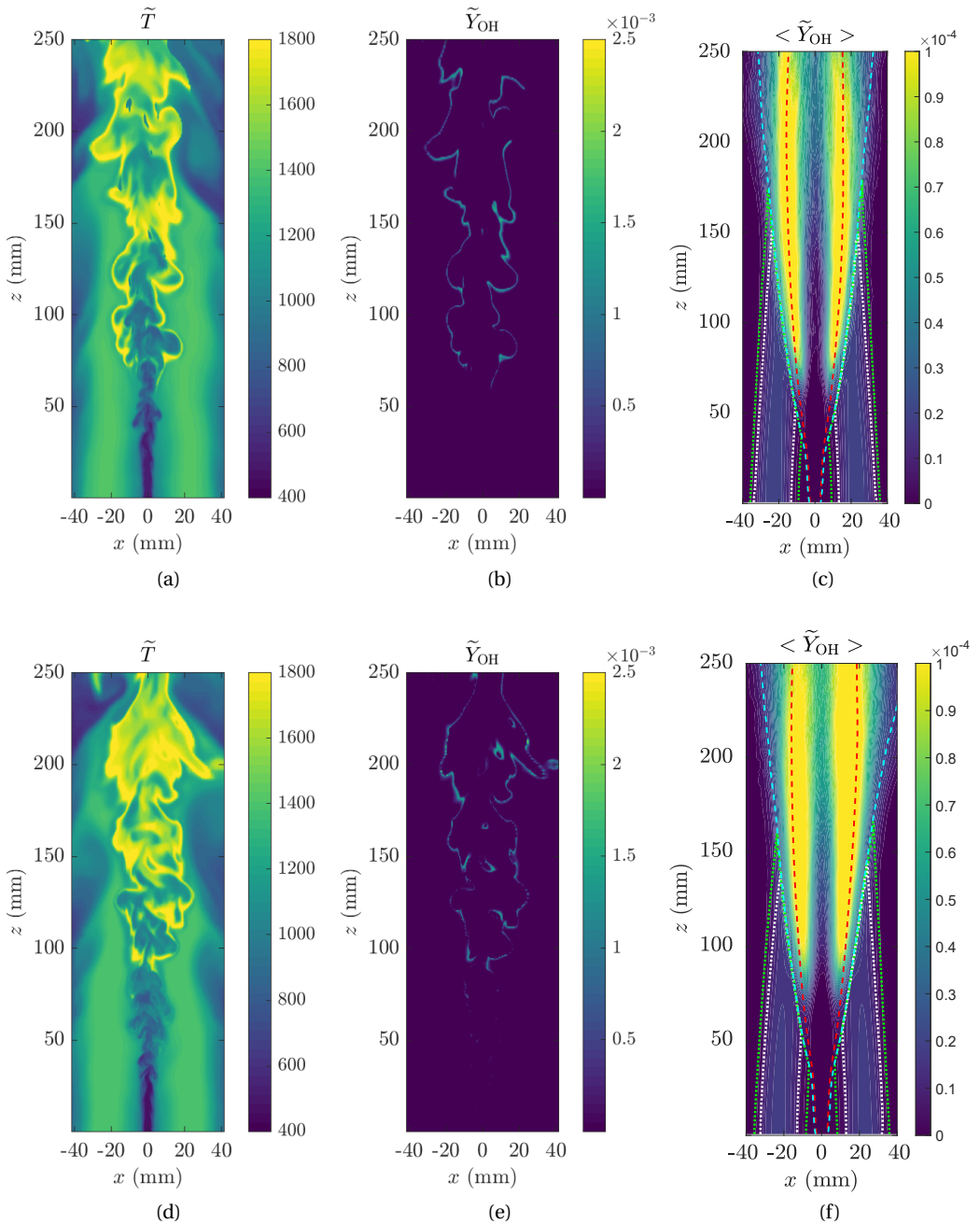


Figure 4.12: Instantaneous temperature and \tilde{Y}_{OH} iso-contours and the average iso-contours of \tilde{Y}_{OH} are shown here for DNG (top row) and biogas DJHC-X flame simulations (bottom row). The dotted lines are; $\tilde{T} = 1200$ K (white) and $\tilde{T} = 1100$ K (green). The dashed lines are $\tilde{Z} = Z_{mr}$ (cyan) and $Z_{st} = 0.16$ (red).

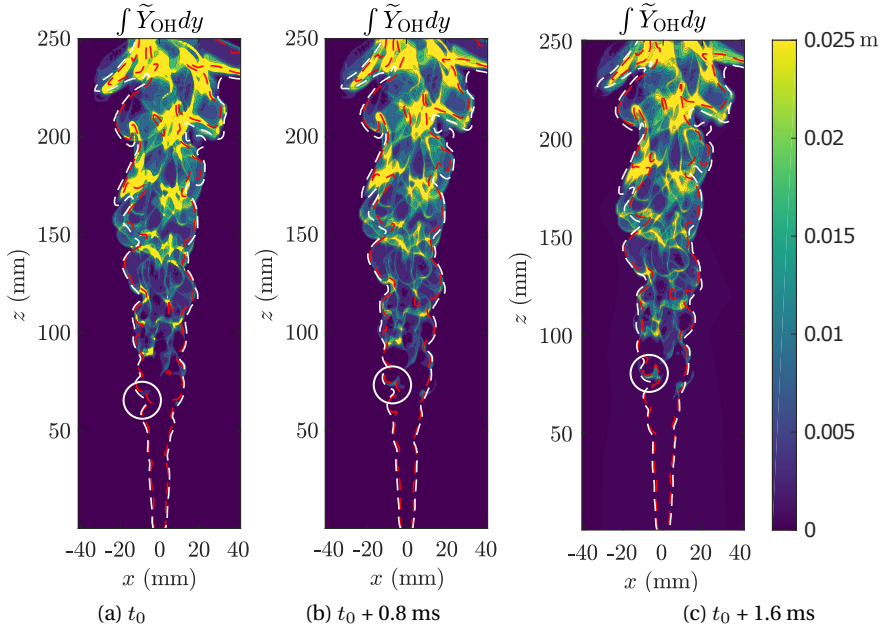


Figure 4.13: Distribution of instantaneous \tilde{Y}_{OH} integrated normal to the center-plane in the biogas DJHC-X flame. The center-plane contours corresponding to $Z_{\text{mr}} = 5.5 \times 10^{-3}$ (red) and $Z_{\text{st}} = 5.5 \times 10^{-2}$ (black) are shown. The white circle indicates how an incursion of the oxidizer results in the formation of an ignition kernel downstream.

mm, which develop into the first peaks of OH mass fraction in Figures 4.13(b)&(c) between $z = 50$ mm to 100 mm. The initial dents signify the entrapment of hot oxidizer pockets from the coflow, where the temperature is about 1200 K. Subsequently in Figure 4.13(c), the kernels expand along the mixture fraction iso-contour. The propagation along the mixture fraction iso-contour is favored in the direction of decreasing scalar dissipation rate. This behavior is made further clear in Fig. 4.14. Figure 4.14 (a) to (c), and (f) to (j) show the development of ignition kernels at two separate instances in the simulation. The dashed lines show the iso-contour lines of Z_{mr} and Z_{st} . In both cases, ignition occurs along the most reactive mixture fraction at a peak in OH mass fraction, visible at $t = 0.8$ ms. By $t = 1.6$ ms the OH values peak at the iso-contour of Z_{st} . However this happens specifically at the region where the mixture fraction iso-contours are diverging, that is at low scalar dissipation rates. The iso-contours of $\tilde{T} = 1100$ K and 1200 K are also shown here. The development of OH kernels occurs in the vicinity of the temperature iso-contours. Therefore, the indicated levels of mixture fraction and temperature play a role in the development of ignition kernels.

Figure 4.15 shows the maximum temperature rise $\Delta\tilde{T}_{\text{max}}(z)$ against time, where $\Delta\tilde{T} = \tilde{T} - T_{\text{mix}}(Z)$, with $T_{\text{mix}}(Z)$ being the initial mixing layer temperature at the same mixture fraction. The subscript $\text{max} = \text{maximum at every } z$, for all (x, y) with

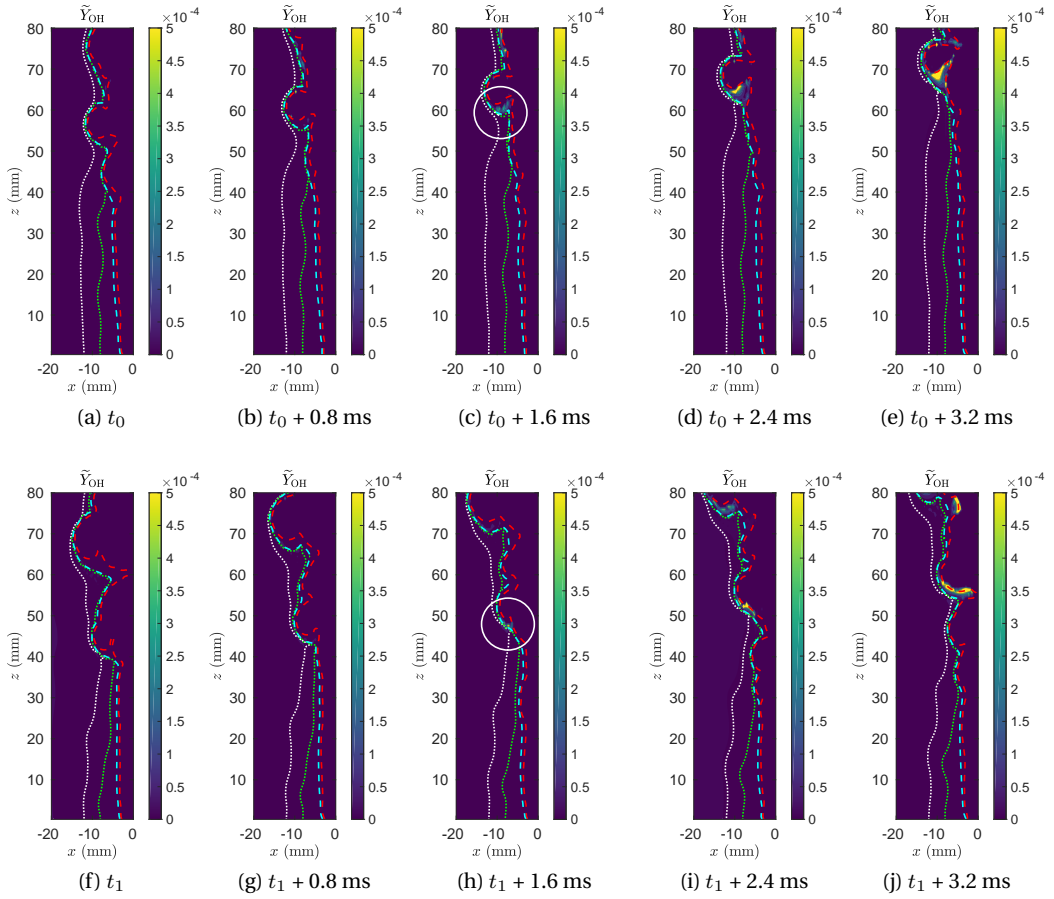
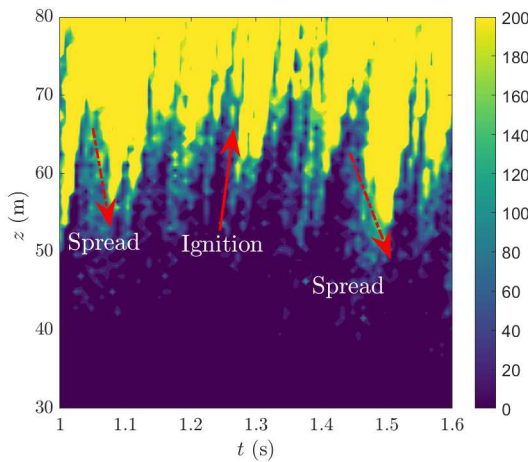
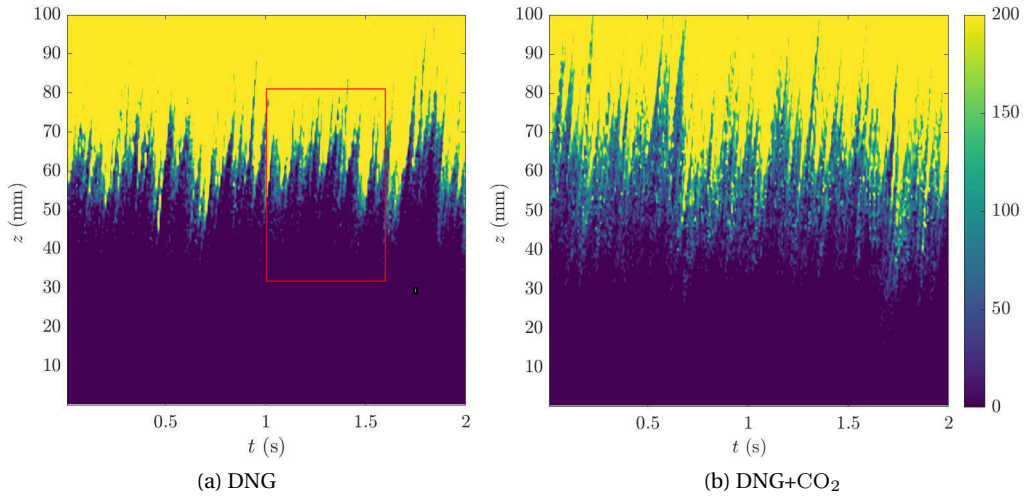


Figure 4.14: Development of OH kernels in biogas DJHC-X flame. The center-plane contours corresponding to $Z_{mr} = 5.5 \times 10^{-3}$ (red) and $Z_{st} = 5.5 \times 10^{-2}$ (cyan) are shown. Also the iso-contour lines of $\tilde{T} = 1200$ K and 1300 K. The white circles indicate the locations where ignition occurs.

mixture fraction $\tilde{Z} > Z_{mr}$ and $\tilde{Z} < Z_{st}$ to isolate the ignition kernels. As shown in Fig. 4.15, a positive inclination of iso-contours of $\Delta\tilde{T}_{max}(z)$ in time indicates the development of an ignition kernel. The individual ignition kernels merge downstream to establish a stable flame front. A negative inclination, visible mainly with the ignition of the DNG flame, indicates the possible propagation of the flame front upstream. The biogas flame has higher reactivity and has an earlier ignition when compared with DNG, as indicated by a rise in temperature at the heights between 30 mm and above, whereas for DNG the temperature rise takes place from 40 mm and above. For the DNG flame, the peak $\Delta\tilde{T}$ streaks appear more clustered than for biogas due to a higher degree of propagation of the ignition front along the mixture fraction iso-contours in DNG. Figure 4.15(c) shows distinct events of ignition



(c) DNG ignition and spread of flame, enlarged view of the red box in (a)

Figure 4.15: Contour plot of maximum temperature rise per z level vs time. The maximum temperature rise is evaluated between mixture fraction iso-contours with $\tilde{Z} = Z_{\text{mr}}$ and $\tilde{Z} = Z_{\text{st}}$.

and spreading of ignition, which are indicated by bold and dashed arrows respectively. The early temperature rise in biogas compared to DNG is further elucidated by their corresponding ignition behavior in IML.

Figure 4.16 shows the evolution of peak temperature rise in a laminar IML with detailed chemistry for DNG and biogas under the DJHC-X boundary conditions. The temperature rise $\Delta\tilde{T}$ is evaluated with respect to frozen mixing temperature

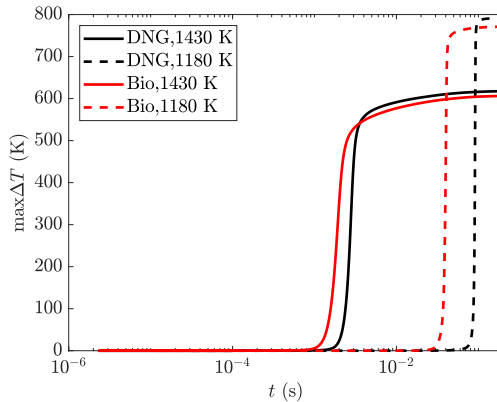


Figure 4.16: Evolution of temperature rise in time for laminar mixing layers with DNG and biogas at conditions representative of the DJHC-X flame. Biogas is indicated as Bio in the legend.

at the same mixture fraction. The faster temperature rise in the biogas DJHC-X flame is consistent with the behavior observed here. The 1D IML ignition delay comparison of biogas against DNG shows that biogas ignites earlier than DNG, as shown in Fig. 4.16.

4.3.4 Comparison to measurements

Figure 4.17 shows the time averaged radial temperature profiles of DJHC-X flame at heights of 3, 65, 110, and 140 mm against the experimental measurements. The experimental results show a lateral shift in the positive x direction with increasing axial height. This could be due to a vertical alignment error of the experimental setup. The LES results show no distinct peak in mean temperature, although there are temperature and OH peaks visible in the instantaneous plots of Fig. 4.12. The experimental measurements show even a decrease in mean temperature at increasing heights, whereas the LES shows no such drop in temperature for both fuels, probably due to the lack of a radiation or any other heat loss mechanisms in the model. Temperature is seen to be increasing in the core of the fuel jets with axial height, indicating a vigorous mixing or dissipative effects in the LES. This happens especially at greater axial heights where the cell volumes are also higher. In the simulation, the flame zones for biogas are wider than DNG as shown in Figure 4.12. A larger spread of the flame zone also means heat release induced destruction of turbulent structures in the small scales, which results in higher mean temperatures close to the jet core for the biogas flame. Therefore, in the simulations the mean temperature increases in the jet core faster for biogas as opposed to DNG. Besides the flame zone, the coflow's mixing with the ambient air near the outer radius of the coflow also produces a radial temperature gradient. At radial distances above 20 mm, the temperature drops due to the mixing with ambient air, which is represented by low-temperature oxidizer and rms temperature in the simulation. The overall difference between the two flames remains small in both

experimental measurements and averaged values in the simulation, although the instantaneous flame behavior shown in Fig. 4.15 and Fig. 4.12 indicates clear differences.

Figure 4.18 shows the rms of temperature, corresponding to Fig. 4.17. In the simulations, no temperature fluctuation is provided at the coflow boundary. Even though velocity fluctuations are simulated at the boundary using Synthetic Eddy Method (SEM), this doesn't lead to a significant increase in the rms for temperature downstream. Further downstream the rms temperature starts to rise in experiment due to mixing with the surroundings. For the DNG flame, the closest match to experimental measurements are obtained at $z = 65$ mm, where ignition is expected. For biogas the rms of temperature shows smaller peaks than in the experimental measurements at $z = 65$ mm. Finally, for both DJHC-X flames, the presence of a flame becomes evident from the second moment of temperature, as the mean temperatures do not show a clear temperature peak. Again, the difference in flame structure that is seen from the instantaneous flame contours in Fig. 4.15 and Fig. 4.12 is not reflected in the rms temperature measurements.

4.3.5 Influence of Reynolds number in DJHC-I

The influence of fuel jet Reynolds number on flame behavior is investigated in the current study using a set of LES simulations on the DJHC-I set up with DNG as the fuel, for three different fuel jet Reynolds numbers, 3000, 4500, and 8500 as given in Table 4.1. The simulations were set up following a study by Oldenhof et al. [42] where the flame lift-off behavior was studied with respect to Reynolds numbers ranging from 3000 to 9500 on the DJHC burner. The variance transport model $\widetilde{Z_1''^2}$ is used in these cases. As seen from the biogas flame in section 4.3.3, the leading edge of an ignition kernel is formed when the most reactive mixture fraction meets the hot region in the coflow. This suggests that the flame lift off height is sensitive to fuel jet Re. Also, from the experiments in JHCs, the lift-off height of the flames is shown to be sensitive to the jet Reynolds number [42, 125].

Figure 4.19 shows the time-averaged results of center-plane OH mass fraction and mixture fraction variance. The lift-off height is represented in the figure by the bold horizontal line, which is the height at which 10% of maximum $\langle \widetilde{Y_{OH}} \rangle$ level in a flame is attained. Additionally, the dashed horizontal line shows the height at which 50% of maximum $\langle \widetilde{Y_{OH}} \rangle$ level in a flame is attained. In the simulations, we see that the flame lift-off heights are not significantly altered by the changes in the fuel jet velocity, characterized by jet Re = 3000, 4500 and 8500. Here Re is estimated at the jet nozzle exit based on the bulk velocity of fuel and the density and dynamic viscosity of DNG, and density is estimated for the nozzle exit temperature. With the increase in bulk velocity of the fuel jet, the entrainment of the coflow increases, in agreement with [43], yet this does not lead to a significant variation in the flame lift-off height. For Re = 8500, the ignition does not occur at a lower height although the enhanced entrainment draws in the hottest oxidizer from the mid-annular region in the coflow. This could be due to the high scalar dissipation preventing the ignition. Further, the effect of scalar dissipation also decreases the growth in $\langle \widetilde{Y_{OH}} \rangle$ downstream, as indicated by the increasing gap between the bold and dashed horizontal lines with Re.

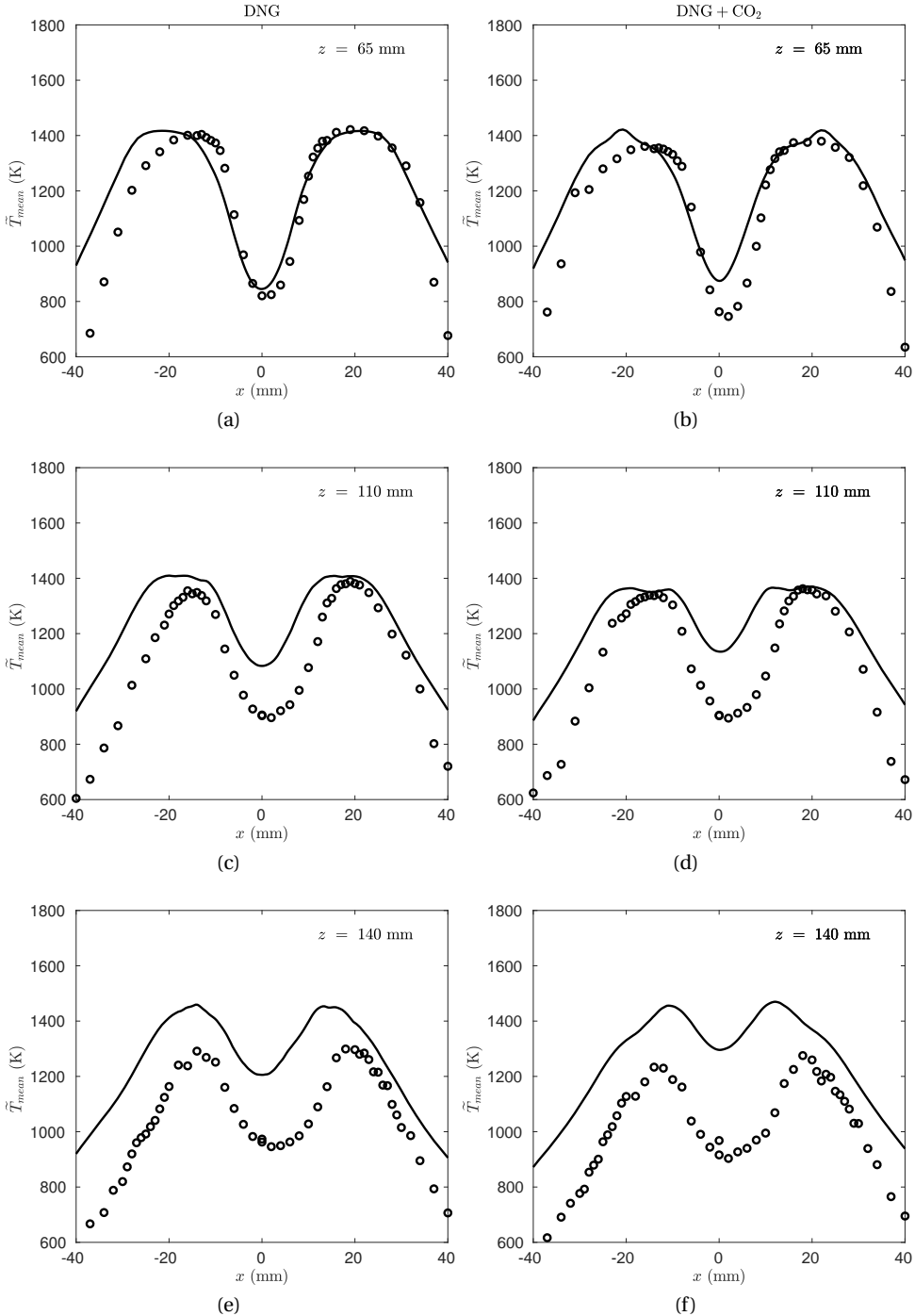


Figure 4.17: Radial plots of Reynolds averaged \tilde{T} from DJHC-X flame simulation, with the plots on the left side (a,c,e) showing the results of the DNG flame, and plots on the right side (b,d,f) showing the results for the biogas flame. Dots and lines in the plots represent the measured and simulated profiles respectively.

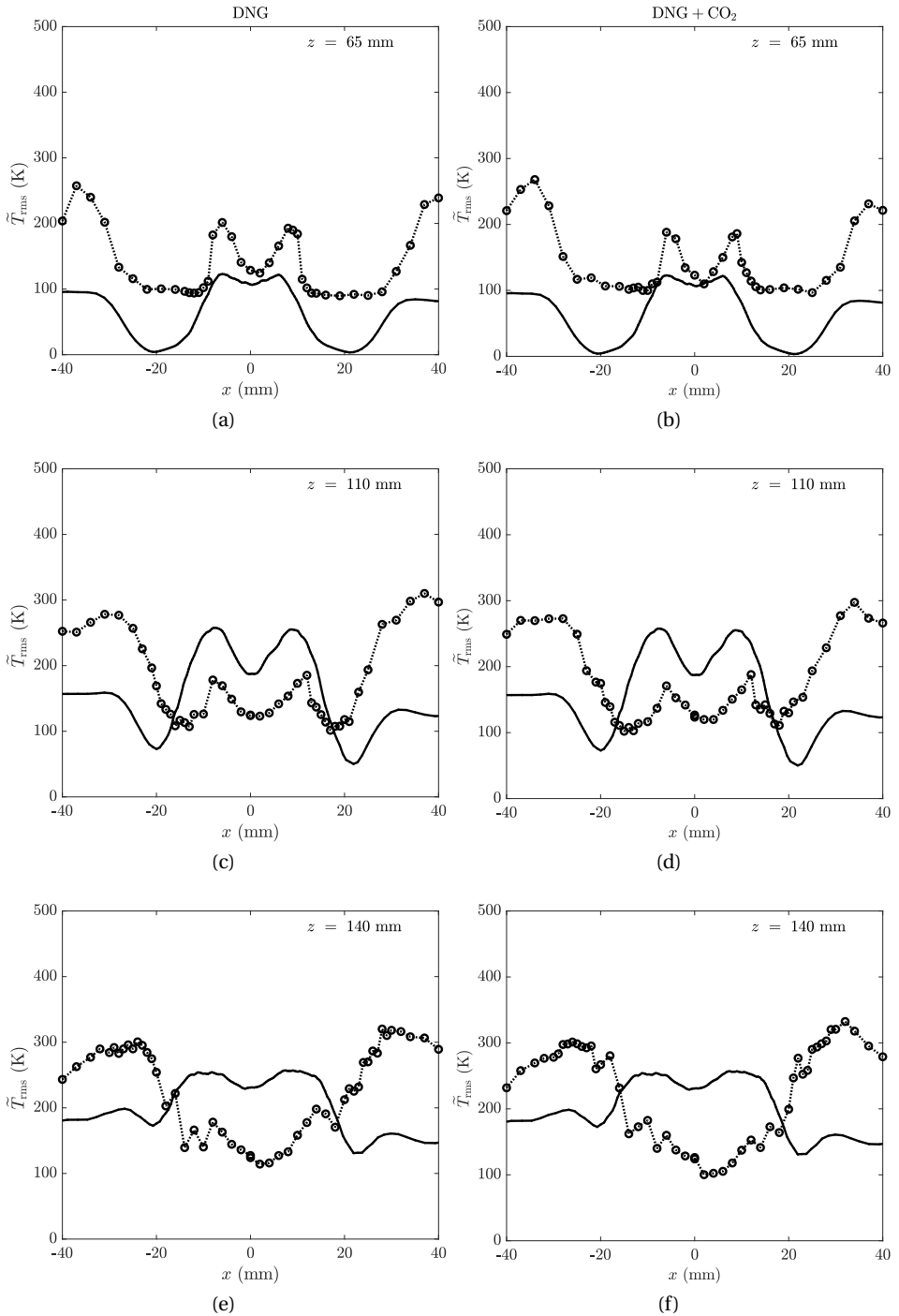


Figure 4.18: Radial plots of the rms of Reynolds averaged \tilde{T} from DJHC-X flame simulation with DNG in the left column and biogas (DNG + CO₂) in the right column. Dots and lines in the plots represent the measured and simulated profiles respectively.

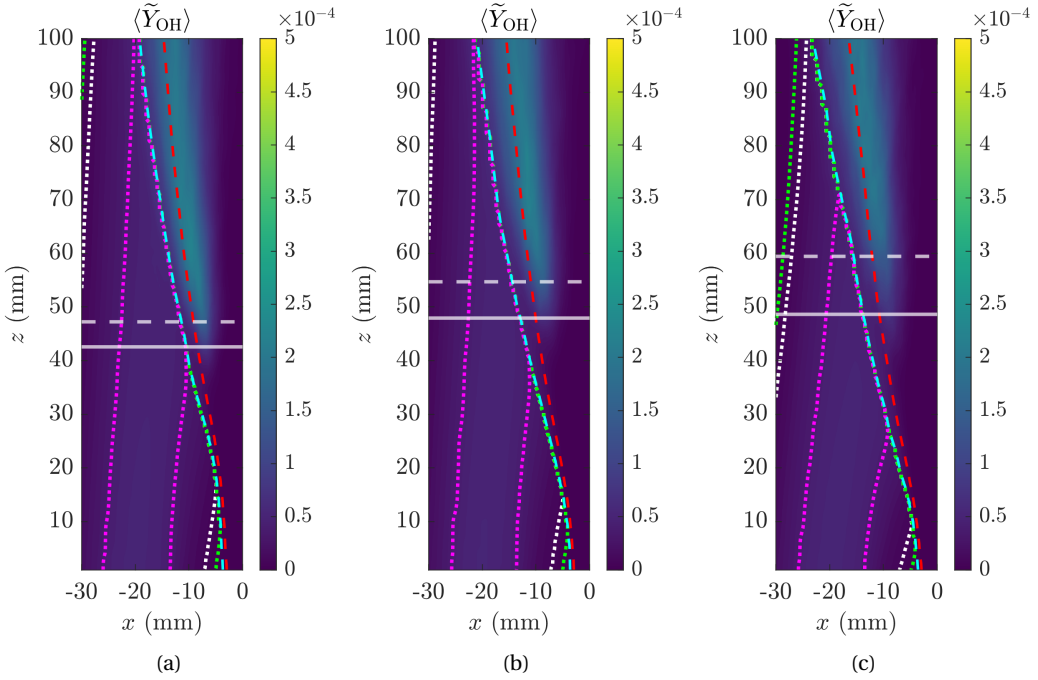


Figure 4.19: Time averaged OH mass fraction at $Re = 3k, 4.5k$ and $8.5k$. Mixture fraction iso-contours with $\langle \tilde{Z} \rangle = Z_{st}$ (red) and $\langle \tilde{Z} \rangle = Z_{mr}$ (cyan) are shown along with the iso-contours of oxidizer temperature $T_{ox} = 1100$ K, 1200 K and 1500 K (green, white and magenta respectively). The bold and dashed horizontal lines represent the respective heights at which 10% and 50% of the maximum $\langle \tilde{Y}_{OH} \rangle$ level in the flame is attained.

4.4 Conclusion

The current study shows that Cabra and DJHC burners have different flame stabilization mechanisms, and the LES-FGM model is formulated to model the range of behaviors from the high oxygen autoigniting flame of the Cabra burner and the low oxygen autoigniting flames of the DJHC burners. Table 4.3 provides the major observations based on the simulation results. The results suggest that for the Cabra flame with high fuel jet Re , the algebraic variance model predicts the ignition with the least accuracy, whereas the transported variance models that results in comparatively higher levels of downstream variance in mixture fraction captures the lift off behavior better. Therefore, to study ignition and lift-off phenomena, the transported variance models are preferred. However, it has to be noted that further downstream in the flame, the algebraic model results in a mean temperature profile that matches the measurements better than transported variance models. For DJHC flames, $\widetilde{Z}_1''^2$ is shown to predict the measurements better than $\widetilde{Z}_2''^2$.

The modeling criteria required for representing the lifted jet flames in LES, un-

	<p>Cabra flame $Z_{st} = 0.16$, 12% O₂, Re = 28000</p>	<p>DJHC-I $Z_{st} = 0.025$, 8% O₂, Re = 4500</p>	<p>DJHC-X, Biogas $Z_{st} = 0.035$, 8% O₂, Re = 3100</p>
$\overline{Z_{alig}''^2}$	<p>Too low lift-off heights</p>	<p>Low lift-off heights</p>	<p>–</p>
$\overline{Z_1''^2}$	<p>Radial temperature profiles show improvement over the algebraic model</p>	<p>Lift off height close to physical observation, Temperature peak is visible in radial profile at ignition. Thermal fluctuations are captured better.</p>	<p>Lift off height close to physical observation, but ignites early. Radial trend in thermal fluctuations is captured.</p>
$\overline{Z_2''^2}$	<p>Radial temperature profiles match closest with the experimental measurement.</p>	<p>No visible peak in radial profiles, however thermal fluctuations show considerable difference with experimental observation.</p>	<p>–</p>

Table 4.3: Summary of mixture fraction sub-grid variance modeling approaches.

der the two sets of distinct boundary conditions is outlined here. Combustion chemistry in Cabra's vitiated coflow flame and the DJHC flame are represented in the LES using IML based FGM tables. The lower oxygen concentration in the coflow of DJHC moves the most reactive mixture fraction to the periphery of the jet compared to Cabra flame, where the effects of turbulence are less intense but not absent. Therefore an accurate prediction of the sub-grid scale variances are important in this case, as the sub-grid scale mixture fraction variance can be under-predicted by the local equilibrium assumption. Due to this reason, the flame lift-off height in DJHC burners are shown to be sensitive to the mixture fraction variance modeling. The flame lift-off in the Cabra flame is shown not to be sensitive to the sub-grid scale variance models as the strong jet turbulence prevents flame stabilization at low axial heights from the burner rim. In DJHC flames, a radially non-uniform coflow makes the flame-lift-off sensitive to the entrainment of the coflow as observable from the comparison of uniform vs non-uniform coflow inlet modeling. The flame lift-off behavior with varying fuel jet Reynolds number alone causes the flame lift-off to monotonously increase with fuel jet Re as captured in the simulations.

The scalar boundary conditions at the inlet mark a clear distinction between the Cabra and DJHC flames in their turbulent modeling. For the Cabra flame, the assumption of uniform inlet boundary condition holds true as the coflow has a near uniform temperature distribution. Owing to the high jet Reynolds number compared to the DJHC flame, flame kernels are unable to sustain or grow in the immediate vicinity of the fuel nozzle in the Cabra burner where a laminar IML flamelet could have achieved ignition. This is due to intense turbulent dissipation smearing out the progress variable source term in the simulation. A lifted flame is captured in the LES for DJHC flames. The predicted flame lift-off position is lower than the experimentally observed lift-off height for DJHC-I, as observed from the temperature fluctuations. In the simulation for DJHC-I the flame is visible at a height of 60 mm in the mean and rms temperature profiles, while in the experiment the increase in rms temperature is only visible at 90 mm. A comparison of uniform and non-uniform coflow boundary condition shows that at 60 mm non-uniform boundary condition leads to higher peak temperatures than measurement. As the flame is highly sensitive to oxidizer temperature, the temperature fluctuations in the coflow inlet could play an important role, which was not considered in the current study. The assumption of a uniform boundary condition in the case of DJHC-I flame captures the peak flame temperatures and peak temperature fluctuations from the measurements. However, the non-uniform boundary condition better represents the overall radial temperature profiles downstream in flame. Although the DJHC-I flame has a low fuel Re compared to the Cabra flame, its lift-off height is shown to be influenced by the non-uniform coflow. The flame lift-off with respect to fuel jet Re is not only attributed to the increased moment and scalar dissipation rates, but also the entrainment of hot coflow adds a competing factor. The competition is manifested in such a way that an increased jet momentum leads to stronger dissipative forces, making flame stabilization at lower heights less probable. On the other hand, the enhanced coflow entrainment caused by the increased jet momentum enables ignition at relatively lower heights owing to the higher temperature, in line with explanation of Oldenhof et al. [42]. Though ignited, the effect

of higher scalar dissipation rate is visible in the delay in flame development downstream with increasing fuel jet Re .

4.A Appendix

4.A.1 Inlet turbulence generation

The inflow boundary for the jet and coflow are modeled based on a synthetic eddy approach that was first developed by Jarin 2006 [126] for homogeneous turbulence, where 3D virtual eddies are generated to satisfy the statistics of first and second order, satisfying the conditions of zero mean, unity variance and zero covariance for the fluctuating velocity field, which is written as,

$$\langle u_j^* \rangle = 0 \quad (4.26)$$

$$\langle u_j^{*2} \rangle = 1 \quad (4.27)$$

$$\langle u_i^* u_j^* \rangle = 0 \quad (4.28)$$

Where the angle brackets stand for the Reynolds average of the quantity. u_j^* stands for the velocity fluctuation in j direction. According to SEM, the fluctuating velocity field is given by the cumulative influence of a fixed number of synthetic eddies of compact support as,

$$u_j^*(x, t) = \sum_{i=1}^N \sqrt{\frac{V_{\text{box}}}{V_{\text{eddy}} N}} \epsilon_j f(x - x_{\text{eddy}}, \sigma_{\text{eddy}}) \quad (4.29)$$

where V_{eddy} is the synthetic eddy volume and N , the number of eddies generated in a virtual Cartesian box of volume V_{box} . ϵ stands for the directionality of the eddy ($\epsilon = \pm 1$), the values of which are assigned with equal probability in each direction. The shape function f defines the shape of eddy relative to its centre x_{eddy} and the eddy radius σ_{eddy} . The chosen shape function has to satisfy the normalization condition over the eddy volume,

$$\frac{1}{V_{\text{eddy}}} \iiint f^2(x - x_{\text{eddy}}, \sigma_{\text{eddy}}) dx = 1. \quad (4.30)$$

Shape of an eddy determines how its contribution gets distributed over its region of influence as well as the spectral content of the fluctuations. The 1D shape function used in the present study is a truncated Gaussian, active over $x \in [-\sigma_{\text{eddy}}, \sigma_{\text{eddy}}]$. The velocity fluctuation field obtained for every time step is scaled to meet the prescribed second order statistics at every grid point on the inlet plane, and is added to the mean flow velocity to obtain the instantaneous velocity signal $\tilde{u}_j(x, t)$.

$$\tilde{u}_j(x, t) = \langle u_j(x, t) \rangle + L_{ij} u_j^*(x, t) \quad (4.31)$$

Where the scaling coefficient matrix L is given by the Cholesky decomposition of the prescribed Reynolds stress tensor R as follows,

$$L = \begin{bmatrix} \sqrt{R_{11}} & 0 & 0 \\ \frac{R_{21}}{L_{11}} & \sqrt{R_{22} - L_{21}^2} & 0 \\ \frac{R_{31}}{L_{11}} & \frac{R_{32} - L_{21}L_{31}}{L_{22}} & \sqrt{R_{33} - L_{31}^2 - L_{32}^2} \end{bmatrix} \quad (4.32)$$

This instantaneous velocity field is applied to the inlet boundary, to match the prescribed statistical description of the flow, as verified from a test setup using MATLAB. However this velocity field is not divergence free. In the LES code, the pressure Poisson solver further corrects the applied velocity field to making it divergence free. The Reynolds stress terms and mean velocities are compared against the prescribed values in the results section.

4.A.2 Simplification of coflow boundary

Figure 4.20 shows the measured points of oxygen concentration and temperature in coflow of DJHC-I. A set of 1D steady state counterflow solutions are plotted here with varying degrees of heat loss on the oxidizer side. These steady flames are constructed with air and methane at room temperature as boundary conditions. Varying degrees of heat loss are applied on the oxidizer side to limit the peak temperature, as occurs in a thermal boundary layer. Although a premixed configuration with heat loss is physically close to the coflow conditions, a counterflow arrangement is sought for computational ease to approximate the species composition. The inner branch of the coflow measurements, that is entrained into the flow immediately from the jet exit is considered with foremost importance. The outer branch is replaced with the same Temperature-oxygen coupling as the inner branch. This consideration follows from the physical significance of the inner branch of coflow, which is immediately entrained by the fuel jet prior to ignition. This follows that a reduced level of oxygen is available to the fuel jet at an axial location where the outer branch is interacting with the fuel jet. However, this aspect is expected to play a minor role in flame lift off heights in the current study. Also this assumption simplifies the FGM generation, and tabulation. For table generation, 1D IMLs are simulated with oxidizer boundary composition obtained by interpolating the measurement points under the steady counterflow solutions that are shown in the figure. A laminar IML based FGM table generated thereafter requires further accounting for thermochemical effects imparted upon by a turbulent environment.

4.A.3 Conservative scalar transport

The lack of conservation of fuel mass flux using the original implementation of Vreman model [112] in LESCO caused a loss of mass in the jet stream, and the flame lift off heights were low due to early spreading of the fuel jet due to the loss of mass. With the implementation of a conserved formulation of scalar convection scheme in the LES transport model, fuel mass flux is conserved. Figure 4.21 shows the fuel mass flux $\dot{m}_F = \dot{m}Z$, where \dot{m} is the total mass flux at any axial height. Here at axial heights of 15, 30, 60, 120 mm the fuel mass flux is fluctuating about the same mean value of 1.51 kg/s, confirming the conservation of mass in LES. Figure 4.12(a),(b),&(c) shows the instantaneous temperature and OH center plane contours for DJHC-X flame using DNG. An averaged center plane contour of OH is also shown here. The temperature contour plot shows the hot oxidizer being entrained into the fuel stream, and pockets of ignition are visible from heights of 60 mm. The corresponding instantaneous contours of OH show the independent

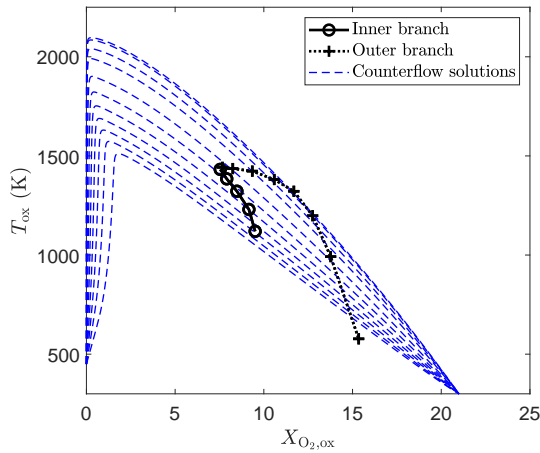


Figure 4.20: Coupling between temperature and oxygen mole fraction in the coflow of DJHC-I case. The coflow is separated into an outer and inner branch as shown here. The dashed line show 1D counterflow flames with various degrees of heat loss on the oxidizer side of the spatial domain in the counter flow set-up.

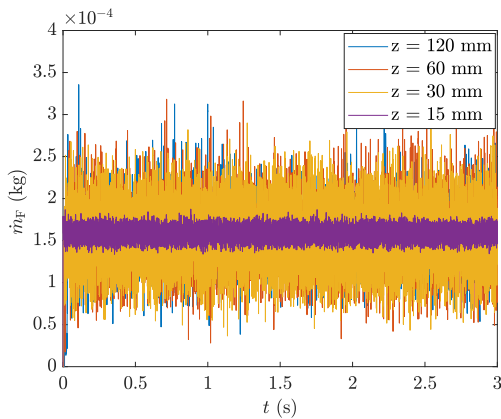


Figure 4.21: Fuel mass flux at various axial distances.

ignition kernel forming in the periphery of the fuel stream. The averaged contour plot of OH shows temperature iso-contours of 1100 K and 1200 K, and mixture fraction iso-contours of Z_{mr} and Z_{st} . The averaging of ignition kernels over time yields a smeared OH mass fraction from $z = 50$ mm till 100 mm, where the ignition kernels form and interconnect to develop into a continuous flame front. The peak OH mass fraction lies on the stoichiometric mixture fraction iso-contour, and the base of the flame coincides with the point where the temperature iso-contour of 1200 K from the oxidizer side meets the iso-contour of Z_{mr} , which indicates the triggering of ignition due to the increased availability of hot oxidizer from the core of the oxidizer stream.

This thesis presents a study of numerical modeling of igniting non-premixed systems for application in the development of MILD burners using biogas and other methane based future fuels. The 1D IML study in chapter 2 revealed key insights regarding biogas flames, i.e., their ignition under non-premixed conditions with a hot diluted oxidizer is hardly dependent on the CO_2 content in the fuel as the most reactive mixture fraction Z_{mr} is very close to 0. The ignition delay is found to be most sensitive to the oxidizer temperature and oxygen concentration in the coflow, but not the dilution of the fuel. A comparison between IML and ICF flames shows that the ignition is slightly delayed when a decaying scalar dissipation rate is present in the reactive zone. However, the scalar dissipation rate aids in the faster spread of the flame in the mixture fraction space, once ignition has occurred at the most reactive mixture fraction, Z_{mr} .

The generic algorithm for progress variable definition discussed in chapter 3 is shown to result in an FGM tabulation which reproduces the ignition delays for igniting 1D flames in DJHC-I and ECN spay-A configurations. The efficacy of the algorithm is tested with two separate detailed reaction mechanisms, namely GRI 3.0 for methane, and a reaction mechanism developed by Yao et al. [107] for n-dodecane. The approach discussed in this chapter is applicable to premixed and non-premixed igniting systems. For its application to MILD flames with the recirculation of combustion products, it will be of interest to have the automated calculation of progress variable weights to reproduce the ignition delays with the recirculation ratio being an additional controlling parameter.

The LES study in Chapter 4 points out the key modeling criteria for JHC flames depending on the fuel type, fuel Re and coflow homogeneity. It is shown that the heat loss at the inner coflow boundary plays an essential role in representing the flame lift off behavior accurately. Furthermore, the evaluation of subgrid scale mixture fraction variance is shown to be key factor for an accurate representation of the flame lift-off height in JHCs. A transported mixture fraction variance model $\widetilde{Z_1''^2}$ has shown to capture the flame lift off behavior of JHC flames in DJHC and Cabra burners. Furthermore, in the present LES, the flame lift-off heights tend to be smaller than the experimental results. This could be due to factors such as;

- The choice of GRI 3.0 as the detailed chemical mechanism: In the case of MILD combustion, ignition delay is predicted differently using different reaction mechanisms, when compared to experimental measurements. A study by Fürst et al. [127] showed that GRI 3.0 predicted an average absolute deviation of 68% from the experimental measurements for methane ignition under MILD conditions. The predicted ignition delays of GRI 3.0 under different temperatures and oxygen levels were lower than the measurements. In their

study, the POLIMI C1-C3 mechanism [128] showed the least average absolute deviation of 40%.

- Ignoring the thermal fluctuations at the coflow-exit: Thermal fluctuations in the coflow which are upto 100 K, can affect the flame lift off. As seen from chapter 2 the ignition delay is most sensitive to temperature fluctuations. Sarras et al. [49] have indicated that accounting for coflow inlet temperature fluctuations in LES will be useful to explore the mechanism of ignition kernel formation.
- Lack of a radiation model: Effects of volumetric radiation heat loss may play a role in the ignition of MILD flames, as the laminar flame thickness is larger than conventional flames. Huang et al. [129] showed that a spectral treatment of the radiative heat transfer for a lab-scale MILD furnace using a RANS approach, although the impact could be small for JHC flames.

The combined effect of these aspects in an LES could be subjected to future studies. The modeling of recirculation of combustion products will be a next step from the current work, which involves:

- i The study of flamelet-flamelet interaction, and ways to incorporate the corresponding effects in a reduced combustion model.
- ii A robust parametrization of FGM for representing the detailed chemistry with varying degrees of fuel and oxidizer dilutions with hot combustion products. X. Huang [130] used the tabulation of a 6D FGM table for modeling MILD combustion in a lab scale burner, incorporating mixture fraction, progress variable, a dilution parameter, enthalpy loss and the variances of mixture fraction and progress variable. A large number of dimensions of FGM leads to large memory usage. Methods to speed up the look-up and handling of FGM table will be needed for future studies.
- iii As the ignition delays for methane are predicted better using POLIMI C1-C3 mechanism than GRI 3.0 under MILD conditions, the application of the POLIMI mechanism in the LES simulations of JHC needs to be explored.

Finally we can conclude that we have advanced the understanding of MILD combustion of biogas and its numerical modeling for application in non-premixed systems. In MILD furnaces the conditions extend beyond what is studied in the current study. However, the findings in this thesis help in understanding the ignition behavior of biogas-like fuel in such applications. In computational studies that aid the development of complex combustion systems, using the FGM approach can significantly reduce the computational cost. For any fuel-oxidizer composition in these systems, the automated progress variable algorithm can be highly effective for avoiding the dilemma of manually choosing an apt progress variable definition. Furthermore, the transported mixture fraction variance model is shown to be critical in estimating the turbulent-chemistry interaction in systems that have the entrainment of burned gas into the fuel stream. These model developments and findings can be leveraged into accelerating the design improvements for MILD burners and furnaces.

Bibliography

- [1] J Kraft and A Kraft. Relationship between energy and GNP. The Journal of Energy and Development, 3(2):401–403, 1978.
- [2] E. A. Wrigley. Continuity, Chance and Change: The Character of the Industrial Revolution in England. Cambridge University Press, 1988.
- [3] E. A. Wrigley. Energy and the English Industrial Revolution. Cambridge University Press, 2010.
- [4] R. Fouquet. The slow search for solutions: Lessons from historical energy transitions by sector and service. Energy Policy, 38(11):6586–6596, 2010. Energy Efficiency Policies and Strategies with regular papers.
- [5] U.S. energy information administration’s international energy outlook 2020. U.S. Energy Information Administration (EIA), 2020.
- [6] International energy outlook 2019; with projections to 2050. U.S. Energy Information Administration (EIA), 2019.
- [7] BP energy outlook: 2019 edition. 2019.
- [8] IPCC. Global warming of 1.5°C - special report. 2018.
- [9] Communication from the commission to the european parliament, the european council, the council, the european economic and social committee and the committee of the regions, the european green deal. 2019.
- [10] Directive (eu) 2018/2001 of the european parliament and of the council of 11 december 2018 on the promotion of the use of energy from renewable sources. Official Journal of the European Union, 2018.
- [11] André P.C. Faaij. Bio-energy in europe: changing technology choices. Energy Policy, 34(3):322–342, 2006. Renewable Energy Policies in the European Union.
- [12] Ministerie EZ. Biomassa 2030—strategische visie voor de inzet van biomassa op weg naar 2030. Ministerie van Economische Zaken (EZ) Directie Groene Groei & BioBased Economy Directoraat-Generaal Bedrijfsleven en Innovatie. The Hague., 2015.

- [13] Bettina Kampman, Cor Leguijt, Thijs Scholten, Jurga Tallat-Kelpsaite, Robert Brückmann, Georgios Maroulis, Jan Peter Lesschen, Koen Meesters, Natasa Sikirica, and Berien Elbersen. Optimal use of biogas from waste streams : an assessment of the potential of biogas from digestion in the EU beyond 2020. European Commission, 2017.
- [14] Nathan Hinton and Richard Stone. Laminar burning velocity measurements of methane and carbon dioxide mixtures (biogas) over wide ranging temperatures and pressures. Fuel, 116:743–750, 2014.
- [15] Tim Patterson, Sandra Esteves, Richard Dinsdale, and Alan Guwy. An evaluation of the policy and techno-economic factors affecting the potential for biogas upgrading for transport fuel use in the uk. Energy Policy, 39(3):1806–1816, 2011.
- [16] Peng Fei Li, Jian Chun Mi, B. B. Dally, Fei Fei Wang, Lin Wang, Zhao Hui Liu, Sheng Chen, and Chu Guang Zheng. Progress and recent trend in MILD combustion. Science China Technological Sciences, 54(2):255–269, feb 2011.
- [17] J. A. Wüning and J. G. Wüning. Flameless oxidation to reduce thermal no-formation. Progress in Energy and Combustion Science, 23(1):81–94, 1997.
- [18] H. Tsuji, A.K. Gupta, T. Hasegawa, M. Katsuki, K. Kishimoto, and M. Morita. High Temperature Air Combustion: From Energy Conservation to Pollution Reduction. CRC Press, 2002.
- [19] M. Katsuki and T. Hasegawa. The science and technology of combustion in highly preheated air. Symposium (International) on Combustion, 27(2):3135–3146, 1998.
- [20] Ahmed E.E. Khalil and Ashwani K. Gupta. Towards colorless distributed combustion regime. Fuel, 195:113–122, 2017.
- [21] Antonio Cavaliere and Mara De Joannon. Mild combustion. Progress in Energy and Combustion Science, 30(4):329–366, 2004.
- [22] M. Oberlack, R. Arlitt, and N. Peters. On stochastic Damkohler number variations in a homogeneous flow reactor. Combustion Theory and Modelling, 4(4):495–509, 2000.
- [23] M. J. Evans, P. R. Medwell, H. Wu, A. Stagni, and M. Ihme. Classification and lift-off height prediction of non-premixed MILD and autoignitive flames. Proceedings of the Combustion Institute, 36(3):4297–4304, 2017.
- [24] P. Li, F. Wang, J. Mi, B. B. Dally, and Z. Mei. Mild combustion under different premixing patterns and characteristics of the reaction regime. Energy & Fuels, 28(3):2211–2226, 2014.
- [25] Y. Minamoto, N. Swaminathan, R. S. Cant, and T. Leung. Reaction zones and their structure in mild combustion. Combustion Science and Technology, 186(8):1075–1096, 2014.

- [26] Nguyen Anh Khoa Doan, Nedunchezian Swaminathan, and Yuki Minamoto. DNS of MILD combustion with mixture fraction variations. *Combustion and Flame*, 189:173–189, 2018.
- [27] N. Swaminathan. Physical insights on MILD combustion from DNS. *Frontiers in Mechanical Engineering*, 5:59, 2019.
- [28] M. De Joannon, A. Cavaliere, T. Faravelli, E. Ranzi, P. Sabia, and A. Tregrossi. Analysis of process parameters for steady operations in methane mild combustion technology. *Proceedings of the Combustion Institute*, 30 II(2):2605–2612, jan 2005.
- [29] Tanh Le Cong and Philippe Dagaut. Oxidation of H_2/CO_2 mixtures and effect of hydrogen initial concentration on the combustion of CH_4 and CH_4/CO_2 mixtures: Experiments and modeling. *Proceedings of the Combustion Institute*, 32 I:427–435, 2009.
- [30] Pino Sabia, Mariarosaria de Joannon, Antonio Picarelli, and Raffaele Ragucci. Methane auto-ignition delay times and oxidation regimes in MILD combustion at atmospheric pressure. *Combustion and Flame*, 160(1):47–55, 2013.
- [31] Stephan Kruse, Bruno Kerschgens, Lukas Berger, Emilien Varea, and Heinz Pitsch. Experimental and numerical study of MILD combustion for gas turbine applications. *Applied Energy*, 148:456–465, 2015.
- [32] V. Mahendra Reddy, Amit Katoch, William L. Roberts, and Sudarshan Kumar. Experimental and numerical analysis for high intensity swirl based ultra-low emission flameless combustor operating with liquid fuels. *Proceedings of the Combustion Institute*, 35(3):3581–3589, 2015.
- [33] Ahmed E.E. Khalil and Ashwani K. Gupta. Swirling distributed combustion for clean energy conversion in gas turbine applications. *Applied Energy*, 88(11):3685–3693, 2011.
- [34] Giancarlo Sorrentino, Pino Sabia, Mara De Joannon, Raffaele Ragucci, Antonio Cavaliere, Ugur Göktolga, Jeroen Van Oijen, and Philip De Goeij. Development of a Novel Cyclonic Flow Combustion Chamber for Achieving MILD/Flameless Combustion. *Physics Procedia*, 66:141–144, 2015.
- [35] P. Sabia, G. Sorrentino, P. Bozza, G. Ceriello, R. Ragucci, and M. de Joannon. Fuel and thermal load flexibility of a MILD burner. *Proceedings of the Combustion Institute*, 000:1–8, 2018.
- [36] André A.V. Perpignan, Arvind Gangoli Rao, and Dirk J.E.M. Roekaerts. Flameless combustion and its potential towards gas turbines. *Progress in Energy and Combustion Science*, 69:28–62, 2018.
- [37] B. B. Dally, A. N. Karpetis, and R. S. Barlow. Structure of turbulent non-premixed jet flames in a diluted hot coflow. *Proceedings of the Combustion Institute*, 29(1):1147–1154, 2002.

- [38] M. J. Evans, A. Chinnici, P. R. Medwell, and J. Ye. Ignition features of methane and ethylene fuel-blends in hot and diluted coflows. Fuel, 203:279–289, 2017.
- [39] Paul R. Medwell, Peter A.M. Kalt, and Bassam B. Dally. Simultaneous imaging of OH, formaldehyde, and temperature of turbulent nonpremixed jet flames in a heated and diluted coflow. Combustion and Flame, 148(1-2):48–61, 2007.
- [40] R. Cabra. Turbulent Jet Flames Into a Vitiated Coflow. Nasa, pages CR–2004–212887, 2004.
- [41] Robert L. Gordon, Assaad R. Masri, and Epaminondas Mastorakos. Simultaneous Rayleigh temperature, OH- and CH₂O-LIF imaging of methane jets in a vitiated coflow. Combustion and Flame, 155(1-2):181–195, 2008.
- [42] E. Oldenhof, M. J. Tummers, E. H. van Veen, and D. J. E. M. Roekaerts. Ignition kernel formation and lift-off behaviour of jet-in-hot-coflow flames. Combustion and Flame, 157(6):1167–1178, 2010.
- [43] E. Oldenhof, M. J. Tummers, E. H. van Veen, and D. J E M Roekaerts. Role of entrainment in the stabilisation of jet-in-hot-coflow flames. Combustion and Flame, 158(8):1553–1563, 2011.
- [44] Ernst Oldenhof, Mark J. Tummers, Eric H. van Veen, and Dirk J.E.M. Roekaerts. Transient response of the Delft jet-in-hot coflow flames. Combustion and Flame, 159(2):697–706, 2012.
- [45] Ernst Oldenhof, Mark J. Tummers, Eric H. van Veen, and D. J. E. M. Roekaerts. Conditional flow field statistics of jet-in-hot-coflow flames. Combustion and Flame, 160(8):1428–1440, 2013.
- [46] Paul R. Medwell, Peter A.M. Kalt, and Bassam B. Dally. Imaging of diluted turbulent ethylene flames stabilized on a Jet in Hot Coflow (JHC) burner. Combustion and Flame, 152(1-2):100–113, jan 2008.
- [47] R. Cabra, T. Myhrvold, J. Y. Chen, R. W. Dibble, A. N. Karpetsis, and R. S. Barlow. Simultaneous laser raman-rayleigh-lif measurements and numerical modeling results of a lifted turbulent H₂/N₂ jet flame in a vitiated coflow. Proceedings of the Combustion Institute, 29(2):1881–1888, 2002.
- [48] L. D. Arteaga Mendez, M. J. Tummers, E. H. Van Veen, and D. J. E. M. Roekaerts. Effect of hydrogen addition on the structure of natural-gas jet-in-hot-coflow flames. Proceedings of the Combustion Institute, 35(3):3557–3564, 2015.
- [49] G. Sarras, Y. Mahmoudi, L. D. Arteaga Mendez, E. H. Van Veen, M. J. Tummers, and D. J. E. M. Roekaerts. Modeling of turbulent natural gas and biogas flames of the delft jet-in-hot-coflow burner: Effects of coflow temperature, fuel temperature and fuel composition on the flame lift-off height. Flow, Turbulence and Combustion, 93(4):607–635, 2014.

- [50] C. S. Yoo, R. Sankaran, and J. H. Chen. Three-dimensional direct numerical simulation of a turbulent lifted hydrogen jet flame in heated coflow: Flame stabilization and structure. Journal of Fluid Mechanics, 640:453–481, 2009.
- [51] J. A. Oijen, van. Flamelet-Generated Manifolds : Development and Application to Premixed Laminar Flames. Technische Universiteit Eindhoven, 2002.
- [52] Charles D. Pierce and Parviz Moin. Progress-variable approach for large-eddy simulation of non-premixed turbulent combustion. Journal of Fluid Mechanics, 504:73–97, 2004.
- [53] D. C. Haworth. Progress in probability density function methods for turbulent reacting flows. Progress in Energy and Combustion Science, 36(2):168–259, 2010.
- [54] A.Y. Klimenko and R.W. Bilger. Conditional moment closure for turbulent combustion. Progress in Energy and Combustion Science, 25(6):595–687, 1999.
- [55] J. W. Labahn and C. B. Devaud. Large Eddy Simulations (LES) including Conditional Source-term Estimation (CSE) applied to two Delft-Jet-in-Hot-Coflow (DJHC) flames. Combustion and Flame, 164:68–84, 2016.
- [56] S. E. Abtahizadeh, L. P.H. de Goey, and J. A. van Oijen. Development of a novel flamelet-based model to include preferential diffusion effects in autoignition of CH₄/H₂ flames. Combustion and Flame, 162(11):4358–4369, 2015.
- [57] A. W. Vreman, B. A. Albrecht, J. A. van Oijen, L. P.H. de Goey, and R. J.M. Bastiaans. Premixed and nonpremixed generated manifolds in large-eddy simulation of Sandia flame D and F. Combustion and Flame, 153(3):394–416, 2008.
- [58] Aromal Vasavan, Philip De Goey, and Jeroen Van Oijen. Numerical Study on the Autoignition of Biogas in Moderate or Intense Low Oxygen Dilution Non-premixed Combustion Systems. Energy and Fuels, 32(8):8768–8780, 2018.
- [59] J.B. Holm-Nielsen, T. Al Seadi, and P. Oleskowicz-Popiel. The future of anaerobic digestion and biogas utilization. Bioresource Technology, 100(22):5478 – 5484, 2009. OECD Workshop: Livestock Waste Treatment Systems of the Future: A Challenge to Environmental Quality, Food Safety, and Sustainability.
- [60] Bianca Cavicchi. Sustainability that backfires: the case of biogas in emilia romagna. Environmental Innovation and Societal Transitions, 21:13 – 27, 2016.
- [61] P. Iovane, F. Nanna, Y. Ding, B. Bikson, and A. Molino. Experimental test with polymeric membrane for the biogas purification from CO₂ and H₂S. Fuel, 135:352 – 358, 2014.

- [62] Saiful Bari. Effect of carbon dioxide on the performance of biogas/diesel dual-fuel engine. *Renewable Energy*, 9(1):1007 – 1010, 1996. World Renewable Energy Congress Renewable Energy, Energy Efficiency and the Environment.
- [63] Yong Qian, Shuzhou Sun, Dehao Ju, Xinxing Shan, and Xingcai Lu. Review of the state-of-the-art of biogas combustion mechanisms and applications in internal combustion engines. *Renewable and Sustainable Energy Reviews*, 69:50–58, 2017.
- [64] Wen Zeng, Hongan Ma, Yuntao Liang, and Erjiang Hu. Experimental and modeling study on effects of N_2 and CO_2 on ignition characteristics of methane/air mixture. *Journal of Advanced Research*, 6(2):189–201, 2015.
- [65] L. J. Muzio and G. C. Quartucy. Implementing NO_x control: Research to application. *Progress in Energy and Combustion Science*, 23(3):233 – 266, 1997.
- [66] J. Wünnig. Flameless oxidation to reduce thermal NO -formation. *Progress in Energy and Combustion Science*, 23(1):81–94, 1997.
- [67] M. de Joannon, P. Sabia, G. Cozzolino, G. Sorrentino, and A. Cavaliere. Pyrolytic and oxidative structures in Hot Oxidant Diluted Oxidant (HODO) MILD combustion. *Combustion Science and Technology*, 184(7-8):1207–1218, 2012.
- [68] P. J. Coelho and N. Peters. Numerical simulation of a mild combustion burner. *Combustion and Flame*, 124(3):503 – 518, 2001.
- [69] Sheng Chen and Chuguang Zheng. Counterflow diffusion flame of hydrogen-enriched biogas under mild oxy-fuel condition. *International Journal of Hydrogen Energy*, 36(23):15403 – 15413, 2011.
- [70] M. de Joannon, G. Sorrentino, and A. Cavaliere. Mild combustion in diffusion-controlled regimes of hot diluted fuel. *Combustion and Flame*, 159(5):1832 – 1839, 2012.
- [71] M. Fischer and X. Jiang. An investigation of the chemical kinetics of biogas combustion. *Fuel*, 150:711–720, 2015.
- [72] Gregory P. Smith, David M. Golden, Michael Frenklach, Nigel W. Moriarty, Boris Eiteneer, Mikhail Goldenberg, C. Thomas Bowman, Ronald K. Hanson, Soonho Song, William C. Gardiner, Jr., Vitali V. Lissianski, and Zhiwei Qin. 2000.
- [73] Bruno Coriton, Jonathan H. Frank, and Alessandro Gomez. Effects of strain rate, turbulence, reactant stoichiometry and heat losses on the interaction of turbulent premixed flames with stoichiometric counterflowing combustion products. *Combustion and Flame*, 160(11):2442 – 2456, 2013.
- [74] Jenni A.M. Sidey, Andrea Giusti, and Epaminondas Mastorakos. Simulations of laminar non-premixed flames of kerosene with hot combustion products as oxidiser. *Combustion Theory and Modelling*, 20(5):958–973, 2016.

- [75] Lin Wang, Zhaohui Liu, Sheng Chen, Chuguang Zheng, and Jun Li. Physical and Chemical Effects of CO₂ and H₂O Additives on Counterflow Diffusion Flame Burning Methane. Energy & Fuels, 27(12):7602–7611, 2013.
- [76] A. Liñán and F. A. Williams. Ignition in an unsteady mixing layer subject to strain and variable pressure. Combustion and Flame, 95(1-2):31–46, 1993.
- [77] J. A. Van Oijen. Direct numerical simulation of autoigniting mixing layers in MILD combustion. Proceedings of the Combustion Institute, 34(1):1163–1171, 2013.
- [78] R. Knikker, A. Dauplain, B. Cuenot, and T. Poinso. Comparison of computational methodologies for ignition of diffusion layers. Combustion Science and Technology, 175(10):1783–1806, 2003.
- [79] T. G. Kreutz and C. K. Law. Ignition in nonpremixed counterflowing hydrogen versus heated air: Computational study with skeletal and reduced chemistry. Combustion and Flame, 114(3-4):436–456, 1998.
- [80] Melvin Gerstein. The structure of laminar flames. Symposium (International) on Combustion, 4(1):35–43, 1953.
- [81] L.M.T Somers. The simulation of flat flames with detailed and reduced chemical models. Eindhoven University of Technology, Eindhoven, The Netherlands, 1994.
- [82] Michael J. Evans, Paul R. Medwell, Zhao F. Tian, Alessio Frassoldati, Alberto Cuoci, and Alessandro Stagni. Ignition Characteristics in Spatially Zero-, One- and Two-Dimensional Laminar Ethylene Flames. AIAA Journal, 54(10):3255–3264, 2016.
- [83] Norbert Peters. Turbulent Combustion. Cambridge Monographs on Mechanics. Cambridge University Press, 2000.
- [84] Heinz Pitsch and Norbert Peters. Investigation of the Ignition Process of Sprays Under Diesel Engine Conditions Using Reduced n-Heptane Chemistry. SAE, (724), 1998.
- [85] Chung K. Law. Combustion Physics. Cambridge University Press, 2006.
- [86] D. Healy, H. J. Curran, J. M. Simmie, D. M. Kalitan, C. M. Zinner, A. B. Barrett, E. L. Petersen, and G. Bourque. Methane/ethane/propane mixture oxidation at high pressures and at high, intermediate and low temperatures. Combustion and Flame, 155(3):441–448, 2008.
- [87] Christopher J. Aul, Wayne K. Metcalfe, Sinéad M. Burke, Henry J. Curran, and Eric L. Petersen. Ignition and kinetic modeling of methane and ethane fuel blends with oxygen: A design of experiments approach. Combustion and Flame, 160(7):1153–1167, 2013.

- [88] Yingjia Zhang, Zuohua Huang, Liangjie Wei, Jiaxiang Zhang, and Chung K. Law. Experimental and modeling study on ignition delays of lean mixtures of methane, hydrogen, oxygen, and argon at elevated pressures. Combustion and Flame, 159(3):918–931, 2012.
- [89] Raimo S. Timonen, Emil Ratajczak, and David Gutman. Kinetics of the reactions of the formyl radical with oxygen, nitrogen dioxide, chlorine, and bromine. The Journal of Physical Chemistry, 92(3):651–655, 1988.
- [90] Epaminondas Mastorakos. Ignition of turbulent non-premixed flames. Progress in Energy and Combustion Science, 35(1):57–97, 2009.
- [91] Aromal Vasavan, Philip de Goey, and Jeroen van Oijen. A novel method to automate fgm progress variable with application to igniting combustion systems. Combustion Theory and Modelling, 24(2):221–244, March 2020.
- [92] N. Peters. Laminar diffusion flamelet models in non-premixed turbulent combustion. Progress in Energy and Combustion Science, 10(3):319–339, 1984.
- [93] J. P. H. Sanders, J. Y. Chen, and I. Gökalp. Flamelet-based modeling of NO formation in turbulent hydrogen jet diffusion flames. Combustion and Flame, 111(1-2):1–15, oct 1997.
- [94] P. J. Coelho and N. Peters. Unsteady modelling of a piloted methane/air jet flame based on the Eulerian particle flamelet model. Combustion and Flame, 124(3):444–465, 2001.
- [95] K. W. Lee and D. H. Choi. Analysis of NO formation in high temperature diluted air combustion in a coaxial jet flame using an unsteady flamelet model. International Journal of Heat and Mass Transfer, 52(5-6):1412–1420, feb 2009.
- [96] Paul R. Medwell, David L. Blunck, and Bassam B. Dally. The role of precursors on the stabilisation of jet flames issuing into a hot environment. Combustion and Flame, 161(2):465–474, 2014.
- [97] Andrew R.W. Macfarlane, Matthew Dunn, Mrinal Juddoo, and Assaad Masri. The evolution of autoignition kernels in turbulent flames of dimethyl ether. Combustion and Flame, 197:182–196, 2018.
- [98] Matthias Ihme and Yee Chee See. Prediction of autoignition in a lifted methane/air flame using an unsteady flamelet/progress variable model. Combustion and Flame, 157(10):1850–1862, 2010.
- [99] R. Cabra, J. Y. Chen, R. W. Dibble, A. N. Karpetis, and R. S. Barlow. Lifted methane-air jet flames in a vitiated coflow. Combustion and Flame, 143(4):491–506, 2005.
- [100] Matthias Ihme and Heinz Pitsch. Prediction of extinction and reignition in nonpremixed turbulent flames using a flamelet/progress variable model. 2. Application in LES of Sandia flames D and E. Combustion and Flame, 155(1-2):90–107, 2008.

- [101] Yong Hu and Ryoichi Kurose. Nonpremixed and premixed flamelets les of partially premixed spray flames using a two-phase transport equation of progress variable. Combustion and Flame, 188:227 – 242, 2018.
- [102] B. Fiorina, O. Gicquel, L. Vervisch, S. Carpentier, and N. Darabiha. Premixed turbulent combustion modeling using tabulated detailed chemistry and PDF. Proceedings of the Combustion Institute, 30(1):867–874, 2005.
- [103] Matthias Ihme, Lee Shunn, and Jian Zhang. Regularization of reaction progress variable for application to flamelet-based combustion models. Journal of Computational Physics, 231(23):7715–7721, 2012.
- [104] Yi Shuai Niu, Luc Vervisch, and Pham Dinh Tao. An optimization-based approach to detailed chemistry tabulation: Automated progress variable definition. Combustion and Flame, 160(4):776–785, 2013.
- [105] Jing Chen, Minghou Liu, and Yiliang Chen. Optimizing progress variable definition in flamelet-based dimension reduction in combustion. Applied Mathematics and Mechanics (English Edition), 36(11):1481–1498, 2015.
- [106] Engine Combustion Network. Sandia National Laboratories, 2016.
- [107] Tong Yao, Yuanjiang Pei, Bei Jing Zhong, Sibendu Som, Tianfeng Lu, and Kai Hong Luo. A compact skeletal mechanism for n-dodecane with optimized semi-global low-temperature chemistry for diesel engine simulations. Fuel, 191:339–349, 2017.
- [108] S. Ebrahim Abtahizadeh. Numerical study of Mild combustion from laminar flames to Large Eddy Simulation of turbulent flames with Flamelet Generated Manifolds. PhD thesis, Department of Mechanical Engineering, 2014.
- [109] Tobias Plessing, Norbert Peters, and Joachim G. Wüning. Laseroptical investigation of highly preheated combustion with strong exhaust gas recirculation. Symposium (International) on Combustion, 27(2):3197–3204, 1998.
- [110] Likun Ma. Computational Modeling of Turbulent Spray Combustion. PhD thesis, Department of Process and Energy, 2016.
- [111] X. Huang, M. J. Tummers, and D. J. E. M. Roekaerts. Experimental and numerical study of MILD combustion in a lab-scale furnace. Energy Procedia, 2017.
- [112] A. W. Vreman. An eddy-viscosity subgrid-scale model for turbulent shear flow: Algebraic theory and applications. Physics of Fluids, 16(10):3670–3681, 2004.
- [113] R.W. Bilger. The structure of turbulent nonpremixed flames. Symposium (International) on Combustion, 22(1):475–488, 1989.
- [114] J.A. Oijen, van. Flamelet-generated manifolds : development and application to premixed laminar flames. PhD thesis, Department of Mechanical Engineering, 2002.

- [115] W. J. S. Ramaekers. The application of flamelet generated manifolds in modelling of turbulent partially-premixed flames. PhD thesis, Department of Mechanical Engineering, Technische Universiteit Eindhoven, 2011.
- [116] B. A. Albrecht, W. J. S. Ramaekers, J. A. van Oijen, and R. J. M. Bastiaans. A progress variable approach based on premixed flamelets for turbulent combustion modeling. Flow, Turbulence and Combustion, 2007.
- [117] Charles D. Pierce and Parviz Moin. A dynamic model for subgrid-scale variance and dissipation rate of a conserved scalar. Physics of Fluids, 10(12):3041–3044, 1998.
- [118] E. Knudsen, E. S. Richardson, E. M. Doran, H. Pitsch, and J. H. Chen. Modeling scalar dissipation and scalar variance in large eddy simulation: Algebraic and transport equation closures. Physics of Fluids, 24(5), 2012.
- [119] C. Jiménez, F. Ducros, B. Cuenot, and B. Bédard. Subgrid scale variance and dissipation of a scalar field in large eddy simulations. Physics of Fluids, 13(6):1748–1754, 2001.
- [120] Heinz Pitsch and Helfried Steiner. Scalar mixing and dissipation rate in large-eddy simulations of non-premixed turbulent combustion. Proceedings of the Combustion Institute, 28(1):41–48, 2000.
- [121] R. van Buuren, J.G.M. Kuerten, and B.J. Geurts. Instabilities of stationary inviscid compressible flow around an airfoil. Journal of Computational Physics, 138(2):520–539, 1997.
- [122] Bram van Leer. Towards the ultimate conservative difference scheme. ii. monotonicity and conservation combined in a second-order scheme. Journal of Computational Physics, 14(4):361–370, 1974.
- [123] A. Skillen, A. Revell, and T. Craft. Accuracy and efficiency improvements in synthetic eddy methods. International Journal of Heat and Fluid Flow, 62:386–394, 2016.
- [124] Aromal Vasavan, Philip De Goey, and Jeroen Van Oijen. Numerical Study on the Autoignition of Biogas in Moderate or Intense Low Oxygen Dilution Non-premixed Combustion Systems. Energy and Fuels, 32(8):8768–8780, 2018.
- [125] Christoph M. Arndt and Wolfgang Meier. Influence of Boundary Conditions on the Flame Stabilization Mechanism and on Transient Auto-ignition in the DLR Jet-in-Hot-Coflow Burner. Flow, Turbulence and Combustion, 102(4):973–993, 2019.
- [126] N. Jarrin, S. Benhamadouche, D. Laurence, and R. Prosser. A synthetic-eddy-method for generating inflow conditions for large-eddy simulations. International Journal of Heat and Fluid Flow, 27(4):585–593, 2006.
- [127] Magnus Fürst, Pino Sabia, Marco Lubrano Lavadera, Gianmarco Aversano, Mara de Joannon, Alessio Frassoldati, and Alessandro Parente. Optimization of chemical kinetics for methane and biomass pyrolysis products in

- moderate or intense low-oxygen dilution combustion. Energy & Fuels, 32(10):10194–10201, 2018.
- [128] E. Ranzi, A. Frassoldati, R. Grana, A. Cuoci, T. Faravelli, A.P. Kelley, and C.K. Law. Hierarchical and comparative kinetic modeling of laminar flame speeds of hydrocarbon and oxygenated fuels. Progress in Energy and Combustion Science, 38(4):468–501, 2012.
- [129] Xu Huang, Mark J. Tummers, Eric H Van Veen, and Dirk J. E. M. Roekaerts. Modelling of MILD combustion in a lab-scale furnace with an extended FGM model including turbulence-radiation interaction. Combustion and flame, accepted for publication, 2021.
- [130] X. Huang. Measurements and model development for flameless combustion in a lab-scale furnace. PhD thesis, Delft University of Technology, 2018.

Acknowledgment

To my promoters, Jeroen and Philip, who had been most supportive, available, critical, as well as patient to me through the eight and something years of PhD. To everyone who made my well-being and therefore this thesis possible with their kindness, love, and immense support, especially my parents. To the invaluable and hopefully lifelong friendships I formed over the years in Gemini Noord 1.21, Mo, Yigit, Denis, Miao, Shuli, to name a few. To my sister, Aneesha. To my wife, Priya, for the days to come.

Aromal Vasavan
Eindhoven
October 19, 2021

Curriculum Vitae

Aromal Vasavan was born on 29-04-1988 in Thamarakkulam, Kerala, India. After finishing Mechanical Engineering in 2009 at Mar Athanasius College of Engineering in Kothamangalam, India, he studied Aerospace Engineering at Indian Institute of Technology Bombay, India. In 2011 he graduated within the Aerospace Propulsion group on “Computational Estimation of Extinction limits for Methane Air Counter-Flow Non-Premixed Flames in Micro-gravity”. The research for his master thesis was conducted at the Institute of Technical Thermodynamics of Karlsruhe Institute of Technology, Karlsruhe, Germany, with a scholarship from DAAD. From 2011 till 2013, he worked as a technologist at General Electric Aviation in Bangalore, India. From 2013 he started a PhD project at Eindhoven University of Technology at Eindhoven, Netherlands, of which the results are presented in this dissertation. Since 2018 he is employed at ASML as a metrology design engineer.

List of Publications

- Numerical study on the autoignition of biogas in moderate or intense low oxygen dilution nonpremixed combustion systems, Vasavan, A., de Goey, L. P. H. & van Oijen, J. A., 16 Aug 2018, In: *Energy & Fuels*. 32, 8, p. 8768-8780 13 p.
- A novel method to automate FGM progress variable with application to igniting combustion systems, Vasavan, A., de Goey, P. & van Oijen, J., 3 Mar 2020, In: *Combustion Theory and Modelling*. 24, 2, p. 221-244 24 p.
- Modeling strategies for jet in hot coflow burners using FGM, Vasavan, A., de Goey, L. P. H. & van Oijen, J. A., *Article in preparation*.
- Modeling MILD combustion with flamelet-generated manifolds, van Oijen, J. & Vasavan, A., 7 May 2019, 17th International Conference on Numerical Combustion - Aachen, Germany.
- Comparative study of RANS-EDC, LES-CSE and LES-FGM simulations of Delft jet-in-hot-coflow (DJHC) natural gas flames, Roekaerts, D. J. E. M., Bao, H., Huang, X., Vasavan, A., van Oijen, J. A., Labahn, J. & Devaud, C., 5 Oct 2016, Combura Symposium, Soesterberg, The Netherlands.
- Higher order correction of progress variable source term in Flamelet Generated Manifolds (FGM) approach for modeling strained 1D counterflow flames, Vasavan, A., de Goey, P. & van Oijen, J. A., 5 June 2016, Hersonissos, Crete, Greece.